UNIVERSITY OF CALIFORNIA

Los Angeles

Focusing light on nanoscale: A novel plasmonic-lens design

A dissertation submitted in the partial satisfaction

of the requirements for the degree Doctor of Philosophy

in Electrical Engineering

by

Shantha Vedantam

2009

The dissertation of Shantha Vedantam is approved.

Jia-Ming Liu

Tsu-Chin Tsao

Chandrashekhar Joshi

Eli Yablonovitch, Committee Chair

University of California, Los Angeles

2009

TABLE OF CONTENTS

LIST OF FIGURES

ACKNOWLEDGEMENTS

I am grateful to many people who have helped me to take up and complete this dissertation. First and foremost, I would like to thank my advisor Prof. Eli Yablonovitch for giving me this research opportunity, scientific guidance, and financial support to work on this project. I am ever indebted to him for the confidence he reposed in my competency from time to time without which I may not have been able to tide through the ebbs of my graduate stint at UCLA. I would also thank my doctoral committee members Prof. Chandrashekhar Joshi, Prof. Jia-Ming Liu, and Prof. Tsu-Chin Tsao for consenting to be on my committee.

I am extremely thankful to my teammate Josh Conway whose PhD dissertation formed the basis of my work. Josh has been the support for the entire plasmonics team with his sound theoretical understanding being something that the every body could count upon. I would like to thank him for his experimental ideas of going beyond the world of plasmonic lens and forging collaboration with other groups. I am also grateful to my teammate Hyojune Lee who has supported and shared my workload in the fabrication and experimental characterization at every step in this project. The efforts of Hyojune and Japeck Tang have helped to successfully complete the fabrication of the plasmonic lens and perform the measurements. Matteo Staffaroni has played a great role in developing the new understanding of metal optics as well as in providing computational support for all plasmonic related ideas. For this, I thank each of them.

I am like to gratefully acknowledge the assistance and guidance I received from the UCLA NRF engineers, in particular to Joe Zendejas, Ivan Alvarado-Rodriguez, Hoc

Ngo, Tom Lee, Wilson Lin, and Hyunh Do who have helped me in innumerable ways from making comments and suggestions to testing the feasibility of my wild ideas for fabrication of the plasmonic lens at the UCLA Nanolab. Included in the above list are several users of the Nanolab with vastly different backgrounds who have discussed and helped me at every stage of the fabrication process in the nanolab.

I would like to extend my thanks to our collaborators Prof. Xiang Zhang's group, Prof. Jean Frechet's group at UC Berkeley for working with us in the plamonics project.

My lab members have been my friends and well-wishers for all my years of stay here. I thank my lab mates, in particular Japeck Tang and Xi Luo for always being there to help me out in the lab at any hour of the day. I owe my thanks to Thomas Szkopek, Subal Sahni, Hans Robinson, Deepak Rao, Jaionne Tirapu Azpiroz, Yunping Yang, Giovanni Mazzeo, and in particular, Adit Narasimha for all their help and guidance in my academic life at UCLA. My graduate stint at the UCLA Optoelectronics group would not have been so smooth if not for the ever-available support of administrative staff comprising of Jaymie Lynn Mateo and Carmichael Aurelio.

Last but not the least; I would thank my parents, sister, all my friends at UCLA Spicmacay student group and elsewhere, my roommates of the last six years, and my spiritual mentors, teachers and friends of the Art of Living Foundation for being there, for forming my moral support system, and for providing encouragement throughout my graduate life at UCLA.

VITA

November 3, 1981	Born, Hyderabad, India
2003	B.E.(Hons.) Birla Institute of Technology & Science, Pilani, India
2003-2006	M.S. Department of Electrical Engineering University of California, Los Angeles
2003-2004	Electrical Engineering Departmental Fellowship CNID Graduate Fellowship
2004-2006	Graduate Student Researcher Department of Electrical Engineering University of California, Los Angeles
2006-2009	Graduate Student Researcher Department of Electrical Engineering University of California, Los Angeles
2009	Student Intern Ostendo Technologies Carlsbad, California

PUBLICATIONS AND PRESENTATIONS

S. Vedantam, H. Lee, J. Tang, J. Conway, M. Staffaroni and E. Yablonovitch, "Fabrication and Characterization of Plasmonic Dimple Lens for nanoscale focusing of light," *Nano Letters*, vol.9, pp. 3447-3452 (2009).

S. Backer, I. Suez, Z. Fresco, J. Frechet **,** J. Conway, **S. Vedantam**, H. Lee and E. Yablonovitch, , "Evaluation of new materials for plasmonic imaging lithography at 476nm using near field scanning optical microscopy," *Journal of Vacuum Technology B*, vol. 25, pp. 1336-1339 (2007).

S. Vedantam, H. Lee, J. Tang, J. Conway, M. Staffaroni, J. Lu and E. Yablonovitch, "Nanoscale Fabrication of a Plasmonic Dimple Lens for Nano-focusing of Light," *Proceedings of SPIE*, vol. 6641, 66411J (2007).

H. Lee, **S. Vedantam**, J. Tang, J. Conway, M. Staffaroni and E.Yablonovitch, "Experimental Demonstration of Optical Nanofocusing by a Plasmonic Dimple Lens" ***[Oral presentation]*** Plasmonics and Metamaterials (META) 2008, Rochester, New York (October 2008)

S. Vedantam and E.Yablonovitch, "Spontaneous Emission as an Antenna Phenomenon" ***[Invited Talk]*** Gordon Conference on Plasmonics, Tilton, New Hampshire (July 2008).

S. Vedantam, H. Lee, J. Tang, J. Conway, M. Staffaroni and E.Yablonovitch, "Novel Plasmonic Dimple Lens for Nano-Focusing Optical Energy," ***[Invited Talk]*** SPIE Optics and Photonics Conference, San Diego (August 2007).

ABSTRACT

Focusing light on nanoscale: A novel plasmonic lens design

by

Shantha Vedantam

Doctor of Philosophy in Electrical Engineering

University of California, Los Angeles, 2009

Professor Eli Yablonovitch, Chair

Surface plasmons are oscillations of the conduction charges at a metal-dielectric interface. The symmetric mode of the surface plasmonic oscillation has no cut-off for propagation. A thin layer of dielectric sandwiched between two thick layers of metal can support plasmonic modes with large propagation constant and small group velocity. Further, surface plasmons can be easily excited by photons.

These attributes of the surface plasmons give way to the design of a circularly symmetric three dimensional nanoscopic structure that can be used to focus down the energy of a

plasmon to a very small volume, much beyond the conventional diffraction limit. Analysis of metal-optics on the sub-wavelength scale using distributed circuit models of transmission lines establishes the equivalence of the plasmonic lens with two-dimensional tapered transmission line. This circuit level perspective brings forth several key insights that govern the nanoscale energy focusing, such as kinetic inductance and impedance transformation in two-dimensionally tapered parallel plate metal-dielectric-metal structures.

The fabrication of a plasmonic lens for focusing the energy poses several challenges. The three dimensional aspect of the design forces us to explore new methods of fabrication and metrological characterization, evaluate the repeatability and yield of several process steps, and finally the integration of these steps into a sequence with each step being compatible with all the other steps in the chain.

This dissertation also discusses the experimental set-up and data analysis of the near-field optical characterization of the plasmonic lens. The limitations of the measurement technique are detailed and this gives way to the suggestions of alternate diagnostics that can improve the characterization of the proposed plasmonic lens in future.

Chapter 1 Introduction

1.1 Motivation

Since the advent of large-scale integration in the field of electronics, the semiconductor industry is moving forward on the road of device miniaturization. The scaling down of the transistors has been governed by the Moore's law, which is bringing about commercial products at the 45nm node in the year 2010, with the ITRS roadmap [1] predicting devices with size 13nm by the end of 2020. This industrial drive has pushed all fields of engineering to study the properties of materials, electromagnetic phenomena, and microfabrication techniques on sub-micron scales. On the other hand, there have been significant advances in biological and chemical sciences in probing molecules to study their physical and chemical properties, particularly with the scanning probe microscopy technique (SPM). Scanning Tunneling Microscopy (STM) technique followed by the Atomic Force Microscopy (AFM) operating in various configurations, like magnetic, electric, optical, surface potential, contact, non-contact, friction modes [2], has enabled the researchers to probe materials at molecular level. The convergence of research interests in both the fields of engineering and science at the nanoscale has led to the emergence of the field of nanotechnology, with each contributing its expertise towards the development of the other.

While the magnetic, electric and conductive modes of SPM probe the materials at low frequencies, the optical mode of probing enables us to study the response of materials at optical frequencies where materials at nanoscale, exhibit widely different and

interesting properties. To be able to probe these phenomena is the way to make discoveries at nanoscale.

At this juncture, one of the most important questions relevant to both engineering and science is an efficient way to couple electromagnetic energy at optical frequencies, to the nanoscale. Once the energy is efficiently coupled, there is a scope to probe molecules or material surfaces with a resolution better than the state-of-art near-field scanning optical microscopy [3] or in achieving optical non-linearities with a small photon count which could lead to new avenues of research. The design and fabrication of probes that deliver energy efficiently can prove to be an important contribution of engineering to nanoscience, and can potentially also open up new realms in nanotechnology.

1.2 Metal-optics at nanoscale

It is interesting to note that metals have always been the materials of choice for applications where electromagnetic energy needs to be focused to a scale smaller than the wavelength. A classic example of this is a wall plug with metal leads. It operates at a frequency of 60Hz where the wavelength of the electromagnetic wave is 5000km (Figure1.1). It is usually regarded as a part of an electrical circuit that is used to deliver electric energy to an appliance that acts as a load. Another example is the phenomenon of photo-assisted STM where sharp metal tip (or a metal coated dielectric or semiconductor tip) is used to concentrate light (Figure1.1) and can achieve energy densities high enough to ablate material in its vicinity [4].

A more recent application of high optical field densities at nanoscale is the use of gold nanoshells in non-invasive cancer therapy. Silica nanospheres of ~100nm in size coated with a thin layer of gold of ~10nm are introduced into the body. These nanoshells tend to selectively accumulate in the regions of tumors. The tissue is then exposed to infrared light; causing high concentrating of energy on the surface of the nanoshells that eventually gets dissipated as heat. This heat destroys the cancer cells only, while the healthy tissue remains unaffected [5]. Another emerging area of application is detection of trace chemicals by capturing their Raman signature. It is well known that rough metallic surfaces tend to concentrate impinging optical fields and this phenomenon of Surface Enhanced Raman Scattering (SERS) can greatly enhance the Raman scattering of the adsorbed molecules [6]. Finally even the magnetic storage industry is integrating metallic nanostructures with the magnetic read/write head to increase the storage capacity of the next generation hard disks. This technology, known as Heat Assisted Magnetic Recording (HAMR), uses metallic structures as near-field transducer elements that can focus laser light into a sub-40nm spot that can heat up the individual bits of a hard disk [7, 8].

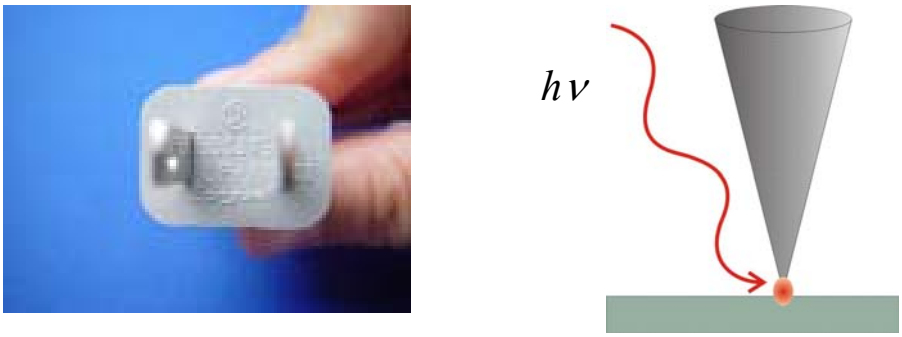

Figure1.1 Wall plug: A sub-wavelength component (on left). Photo-assisted STM (on right)

Electromagnetics on the sub-wavelength scales can be modeled using the circuit theory formalism. Circuits use lumped elements like inductors, capacitors, resistors, voltage generators etc to depict the flow of electromagnetic energy. Inductors and capacitors are energy storage elements while resistors are energy dissipative elements. Both these kinds of elements cause impedance to the flow of current through the circuit. These lumped elements are much smaller than the wavelength of operation. So the electric and magnetic fields associated with these elements are deemed to be quasistatic. This implies that in the regime of sub-wavelength electromagnetics, the temporal changes in current through the lumped elements would cause near negligible change in the spatial static field distribution in and around these circuit elements [9, 10].

Electromagnetics is completely governed by the Maxwell's equations. Maxwell's equations use the dielectric constant ε of a medium to establish the relationship between the electric and the magnetic fields and the sources like charges and currents. On the

other hand, the conductivity σ (or resistivity $\rho = 1/\sigma$) is typically used to relate the electric field $\boldsymbol{E}$ and current density $\boldsymbol{J}$ used in the circuit formalism.

$$\mathrm{J} = \rho E \tag{1.1}$$

$$\nabla \times \boldsymbol{H} = \frac{\partial \boldsymbol{D}}{\partial t} = \varepsilon_r \varepsilon_o \frac{\partial \boldsymbol{E}}{\partial t} \tag{1.2}$$

$$\nabla \times \boldsymbol{H} = \boldsymbol{J} + \varepsilon_o \frac{\partial \boldsymbol{E}}{\partial t} = \frac{\boldsymbol{E}}{\rho} + \varepsilon_o \frac{\partial \boldsymbol{E}}{\partial t} \tag{1.3}$$

To establish the equivalence between ε and ρ (or σ),

$$\rho = \frac{j}{\omega \varepsilon_0 (1 - \varepsilon_r)} \tag{1.4}$$

In the above equations $\varepsilon_r = \varepsilon_r' + j\varepsilon_r''$ where ε_r is the complex relative dielectric constant of a metal. The imaginary part of ε_r contributes to the real part of resistivity ρ where as the negative real part of ε_r gives rise to a relatively unknown imaginary part of ρ that represents a new kind of inductance known as the kinetic inductance.

The ε_r of a metal is a function of frequency. At lower frequencies, its imaginary part dominates over the absolute value of the real part and this makes the metal resistive. However, at higher frequencies the resistivity ρ becomes imaginary and the metal is in a regime where kinetic inductance comes to fore. Figure1.2 is a plot demarcating the regions of dominant impedance for a cylindrical silver wire of specific dimension in a specific frequency range of operation.

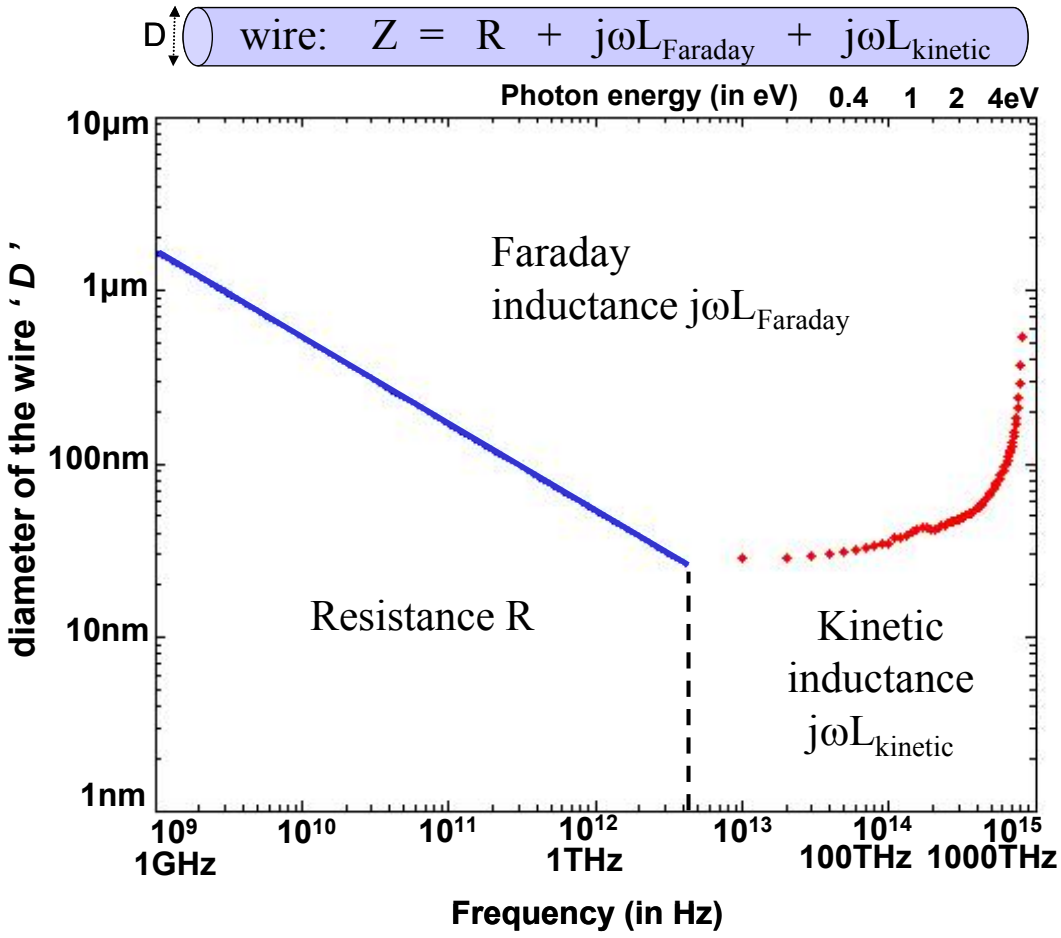

Figure1.2 A dominant-impedance plot of a silver wire in different length-scale vs frequency regimes

The above plot also indicates a third region of impedance namely the faraday inductance. This is the conventional inductance that is the ratio of the magnetic flux generated by the current flowing through the metal wire. It is also interesting to note that diameter of the wire plays an important role in determining which of the three impedances dominates for any given frequency. This should not come as a surprise because both resistance and kinetic inductance depend on the cross-sectional area of the

wire through which the current flows. More details on this graph are discussed in the next chapter 2, section 2.6.

The focus of this dissertation is to work with metallic nanostructures at optical frequencies. So far we have discussed this from the perspective of a circuit model. Surface plasmons are photonic modes coupled to the interface of a metal and a dielectric. Guiding surface plasmons through metallic waveguide structures can also concentrate the optical energy at nanoscale. The next section delves into the features and characteristics of surface plasmonic modes.

1.3 Surface plasmons

The response of a material to electromagnetic fields is characterized by its dielectric constant ε. The susceptibility of a material, $\chi\ (= \varepsilon - 1)$ is the ratio of the polarization induced in a material, $\boldsymbol{P}$ to the applied electric field, $\boldsymbol{E}$. Materials with bound electrons get polarized in the direction of the applied electric field and hence have a positive χ. These materials are known as dielectrics. On the other hand, certain materials, like metals, respond by polarizing in a way so as to oppose applied field, $\boldsymbol{E}$**.** These have a negative χ, thereby a negative dielectric constant ε. These materials have sea of electrons, which can freely respond to the applied field, $\boldsymbol{E}$. As per the lossless Drude model, the relative dielectric constant for free electron plasma is given by

$$\varepsilon_r(\omega) = 1 - (\omega_p/\omega)^2 \tag{1.5}$$

In the above equation ω_p is the bulk plasmon frequency of the metal given by $(Ne^2/\varepsilon_0 m)^{1/2}$, where N is the volume electron density, is the permittivity of free space, e and m are the electronic charge and mass, respectively.

Plasmons are the oscillations of electron gas in metals against the positive ion core. Inside a metal (or doped semiconductor), the electron gas can oscillate longitudinally along the direction of propagation of the wave. These are called bulk or volume plasmons. These modes can be excited by waves, which have electric field component along their propagation vector. Hence transverse electromagnetic waves cannot excite bulk plasmons.

Bulk plasmons can be excited by electrons of sufficient energy impinging on a thin metallic surface [11]. In this case the electric field between the electrons and the induced positive image charge in the metal, and direction of propagation of the electrons are parallel to each other. The metal is thin such that electrons can lose energy and momentum to bulk plasmon modes. The transmitted electron energy is analyzed with a technique known as electron energy loss spectroscopy, EELS which gives the characteristic bulk plasmon frequency of the metal.

Surface plasmons are the surface modes of electric and magnetic field distributions, which decay in the direction away from the interface of two media. Solving Maxwell's Equations for such surface modes, the boundary condition of continuity of the normal component of displacement vector $\boldsymbol{D}$ requires one of the media to have a negative dielectric constant ε. From the discussion at the beginning of this section, it follows that one of the media must be a metal.

Thus, surface plasmons can be defined as the collective oscillations of conductive electron gas of a metal at the metal-dielectric interface as shown in Figure1.3

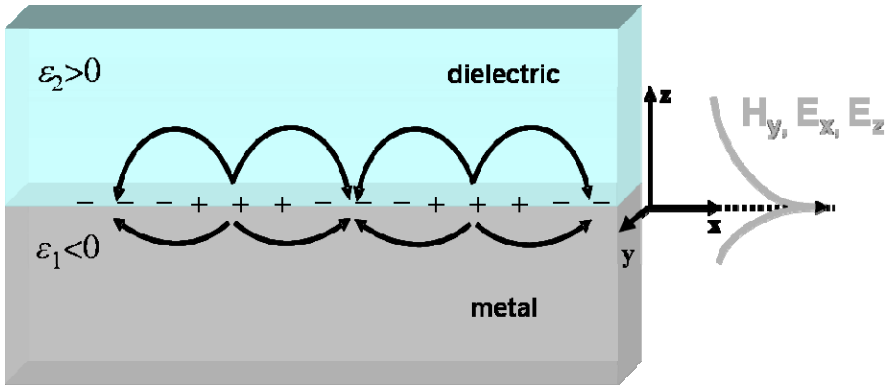

Figure 1.3 Collective oscillations of charges at dielectric-metal interface. The surface plsamon propagates along x-axis and the magnetic field H_y is pointing along the y-axis. E_x, E_z and H_y decay both into the dielectric as well as the metal.

The bound surface charges oscillating at optical frequencies form ac currents that give rise to magnetic fields along the *y*-axis as depicted in Figure1.1. The electric field lines between the negatively charged electrons and positive ionic background core, have both longitudinal and transverse character as they fringe into the dielectric and the metal, implying that the electric field has both *x* and *z* components. The transverse character of the electric field lines makes it possible for the coupling between plasmons and transverse electromagnetic waves.

The dispersion relation for surface plasmons stands as

$$k_{sp} = \sqrt{\frac{\varepsilon_{metal}(\omega)\varepsilon_{dielectric}}{\varepsilon_{metal}(\omega) + \varepsilon_{dielectric}}}\, k_0 \qquad (1.6)$$

where k_0 is the wave-vector of free-space photon and k_{sp} is the wave-vector of the surface plasmon.

Figure1.4 is a plot of the dispersion relation for surface plasmons at the air-lossless Drude metal interface.

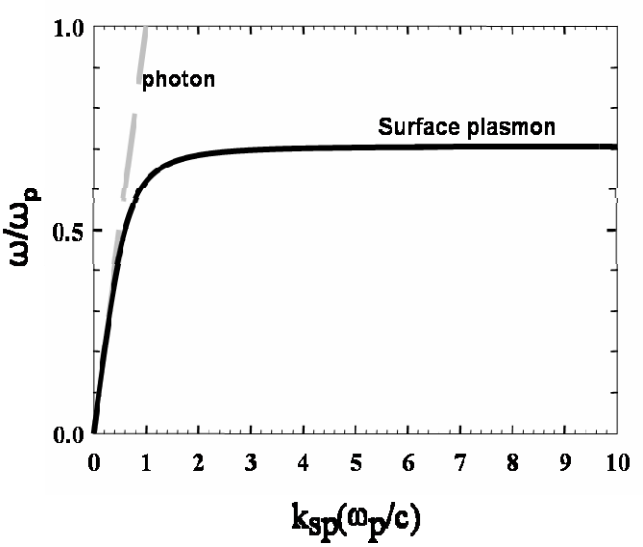

Figure1. 4 A plot of dispersion relation (ω vs k) for a surface plasmon (solid) and photon (dashed)

The following observations can be made from the above Equation1.6 and Figure1.4

- Resonance condition for the surface plasmons occurs at a frequency where the $|\varepsilon_{metal}| = \varepsilon_{dielectric}$ when the denominator of the Equation1.6 goes to zero. This frequency is called surface plasmon frequency, ω_{sp}.
- At the resonant frequency, the propagation vector, k_{sp}, of the surface plasmons becomes very large. For silver, this resonance occurs at around 3.2eV.

- The surface plasmon dispersion curve always lies to the right of the light line. This is indicative of the fact the free space photons cannot couple into surface plasmons at silver-air interface and vice-versa owing to momentum mismatch.
- As the surface plasmon resonance is approached, the phase velocity and the group velocity of the surface plasmons decrease.

1.4 Organization of the dissertation

This dissertation draws upon the PhD dissertation of Josh Conway [12], whose design of a lens-like structure aimed at sub-wavelength focusing of energy forms the basis of the fabrication and experimental work presented here. The Chapter 2 describes the concept and design of nanoscopic lens for the focusing the energy of surface plasmons to the nanoscale. It also discusses the circuit perspective on metal-optics. Some preliminary experiments leading to characterization of thin silver films and grating in-coupler are presented in Chapter 3. The Chapter 4 outlines the nanofabrication challenges and schemes upon which a fabrication process flow is developed in Chapter 5. The Chapter 5 also describes the experimental setup and analyzes the experimental data, followed by the discussion of the experimental limitations. The final chapter suggests alternate diagnostic schemes that can further improve the characterization of the proposed plasmonic lens. It also discusses the progress on the issues that address the limitations of design or fabrication of the plasmonic lens while also touching upon some new ideas of design, analysis, or fabrication.

Chapter 2 Plasmonic lens: Concept and Design

2.1 Motivation

In far-field optics, it is well established, that light cannot be focused beyond spot of size of ~λ/2. This is called the Rayleigh limit. When a collimated beam of light is incident on a circular aperture of diameter *D*, its diffraction pattern is composed of Airy's disks with the angular radius of the first disk being $1.22\lambda/D$. If the circular aperture is replaced with a circular lens of diameter *D* and focal length *f*, then the size of the focused spot is $1.22\lambda f/D$. This diffraction limit follows from the uncertainty principle of $\Delta x\, \Delta k_x = 2\pi$ where $\Delta k_x = 2k_0 D/f$ are the spatial frequencies k_x that form the image ranging from $+k_0 D/f$ to $- k_0 D/f$, giving rise to minimum spot size of $\lambda f/D$.

The uncertainty principle implies that the spot size Δx can be made smaller by increasing the range of spatial frequencies that form the image. Since an aperture or a lens allows only a small range of spatial frequencies to propagate and form an image in the far field, the spot size of the beam or optical resolution of the image is limited. However, the range of spatial frequencies can be increased if instead of being limited to propagating spatial frequencies, we use evanescent waves for imaging. This is the principle behind near-field imaging where a large number of evanescent wave-vectors are used in the near field of an aperture or tapered fiber probe illuminated by light.

The concept of imaging with evanescent waves forms the basis of Near-field Scanning Optical Microscopy (NSOM) technique which could give a sub micron resolution of ~50-100nm [3]. A tapered silica probe with a core aperture diameter of 50-

80nm is coated with metal. Light guided by the silica core is evanescently coupled out of the aperture. With appropriate surface feedback mechanism, the probe is positioned a few nanometers away from the surface where there is interaction between the illuminating near field and the probe.

The amount of energy out-coupled into the near field is a strong function of the size of the aperture and taper angle of the fiber. The transmission efficiency of a fiber probe falls off as fourth power of the radius of the aperture [13,14]. Also smaller the taper angle, the evanescent photons have to tunnel through a larger distance before out coupling, hence lower is the efficiency. The state-of-art loss for commercial pulled fiber probes is about 50-60dB [15]. By engineering the taper design, the losses have been brought down to 20-30dB [16]. However, these losses are still pretty large and resolution is limited to ~50-100nm.

Enhanced transmission through metals perforated with holes has been observed [17]. This transmission is mediated by surface plasmons. Photons couple into surface plasmons on the illuminated side of the metal film. These plasmons propagate through the holes and out-couple into photons on the other side of the film. The pitch and size of the holes is important and is a function of the wavelength of illumination. In the near field of the holes, the spot size is limited by the wavelength of the excited surface plasmons, which is on the order of exciting wavelength, hence is not very small.

Another interesting feature of associated with surface plasmons is the enhancement of electric field $\boldsymbol{E}$. Conventionally light can be focused down to a Gaussian beam with peak $\boldsymbol{E}$ field occurring at the center of the beam. The spot size $2w_0$ of the

beam is limited the Rayleigh limit. Surface plasmons are the modes where fields decay into both the dielectric and the metal with the maximum field at the interface. If all the power of a Gaussian beam is coupled into surface plasmons, then the magnitude of the $\boldsymbol{E}$ at the surface is much greater than the $\boldsymbol{E}$ in the Gaussian beam, thereby leading to an enhancement in the $\boldsymbol{E}$-field. The more localized the plasmons are, the more is the enhancement in the $\boldsymbol{E}$ field. Very high electric field enhancements on the order of 10^4-10^6 can be obtained on rough metallic surfaces. An adsorbed molecule at these surfaces emits a strong characteristic Raman signal. This is phenomenon is known as Surface Enhanced Raman Scattering (SERS) [6].

Due to (i) the limitations on the throughput of energy and resolution of evanescent near field imaging through tapered fiber probes and (ii) the prospect of enhanced transmission and large electric fields of surface plasmons at nanoscopic scale, it pays to design a plasmonic structure harnessing the salient features of surface plasmons to deliver optical energy to nanoscale.

2.2 Double-sided surface plasmons

Section 1.3 examined the features of the dispersion relation of surface plasmons at the interface of a lossless Drude metal and air (Figure1.4). These plasmons are called single-sided plasmons, which exist, at the interface of semi-infinite half spaces of metal and dielectric. Suppose that the metal layer has finite thickness, d as in Figure2.1 (a). Now there are two interfaces of metal and air. The surface plasmon fields decay exponentially as one moves into the dielectric or the metal. As long as the thickness of

the metal, *d* is 3-5 times greater than the decay length of the plasmon field, surface plasmon modes on the two interfaces are independent of each other and can be each regarded as a single-sided plasmon. However as the thickness *d* reduces, the plasmon on one interface sees the presence of the other interface and gets coupled to the other plasmon. In other words, the two single-sided plasmons modes mix to give rise to two double-sided plasmon modes –a symmetric mode and an anti-symmetric mode. Figure2.1 (a) is popularly referred to as Insulator-Metal-Insulator (IMI) geometry where the Figure2.1 (b) is the Metal-Insulator-Metal (MIM) geometry.

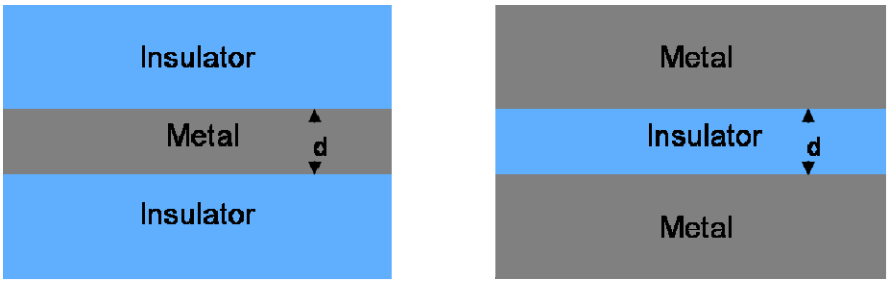

(a) **(b)**

Figure2. 1 (a) Insulator-Metal-Insulator (IMI) geometry (b) Metal-Insulator-Metal (MIM) geometry

The dispersion relation for the double-sided plasmons may be derived by considering the reflectance of the stack of IMI or MIM geometries. The reflectance of the MIM stack is given by Equation 2.1.

$$r_{MIM} = \frac{r_{MI} + r_{IM}\exp(i2k_{zI}\,d)}{1 + r_{MI}r_{IM}\exp(i2k_{zI}\,d)} \qquad (2.1)$$

where r_{MI} is the field reflectivity of the light incident from medium *M* to medium *I*, $k^2_{zI} = \varepsilon_I k^2_0 - k^2_{sp}$ and $ksp = k_{xM} = k_{xI}$ and

$$r_{MI} = \left[\frac{\frac{k_{zM}}{\varepsilon_M} - \frac{k_{zI}}{\varepsilon_I}}{\frac{k_{zM}}{\varepsilon_M} + \frac{k_{zI}}{\varepsilon_I}} \right] \tag{2.2}$$

Equating that denominator of Equation2.1 to zero, the k_{sp} can be solved at every frequency ω. Equation2.3 gives the dispersion relation

$$\left(\frac{k_{zM}}{\varepsilon_M} + \frac{k_{zI}}{\varepsilon_{MI}}\right)\left(\frac{k_{zM}}{\varepsilon_M} + \frac{k_{zI}}{\varepsilon_{MI}}\right) + \left(\frac{k_{zM}}{\varepsilon_M} - \frac{k_{zI}}{\varepsilon_{MI}}\right)\left(\frac{k_{zM}}{\varepsilon_M} + \frac{k_{zI}}{\varepsilon_{MI}}\right)\exp(i2k_{z1}\mathrm{d}) = 0 \tag{2.3}$$

We note that the dielectric constant ε_{metal} is dispersive and complex. Figure2.2 (a) and (b) are log-plots of ε'_{silver} and ε''_{silver} as a function of frequency [18].

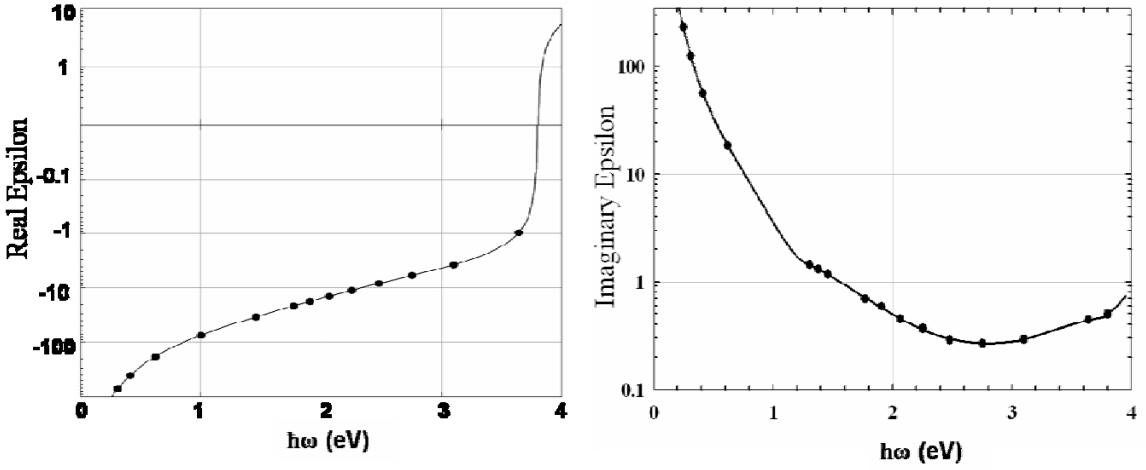

(a) **(b)**

Figure2.2 Log plots (a) Real part of ε'_{silver} (b) Imaginary part of ε''_{silver} as a function of photon energy.

The dispersion relation, Equation2.3, will have real part as well as an imaginary part because the ε_{metal} is a complex quantity. The roots of this equation yield the plasmon dispersion plot (k'_{sp} vs ω) for double-sided plasmons of the MIM structure where as the solutions for the imaginary part of the equation given the decay lengths (=1/ k''_{sp}).

From Figure2.2 (b) it can be seen that the ε''_{silver} is lowest in the range of 2-3eV of light corresponding to a free space wavelength range of 420-620nm. As the surface plasmon propagates at the interface of silver and silica, the imaginary part of the dielectric constant results in energy absorption, also known as the Joule heating losses.

For any electromagnetic energy that propagates in a lossy dispersive medium, the quality factor Q is given by the Equation2.4 [19]

$$Q \equiv \frac{\omega U}{-dU/dt} = \frac{\frac{1}{2}\int\left(\frac{\partial(\omega\varepsilon')}{\partial\omega}E^2 + \frac{\partial(\omega\mu')}{\partial\omega}H^2\right)d\tau}{\int\left(\varepsilon''E^2 + \mu''H^2\right)d\tau} \tag{2.4}$$

After some approximations in the regime when ***E***-field is much larger than the ***H***-field, the following equation is obtained [18] from Equation2.4

$$Q_{mat} \equiv \frac{\partial(\omega\varepsilon')/\partial\omega}{2\varepsilon''} \tag{2.5}$$

A plot of the Q values for silver, gold, copper, aluminum all of which support surface plasmons is given in Figure2.3

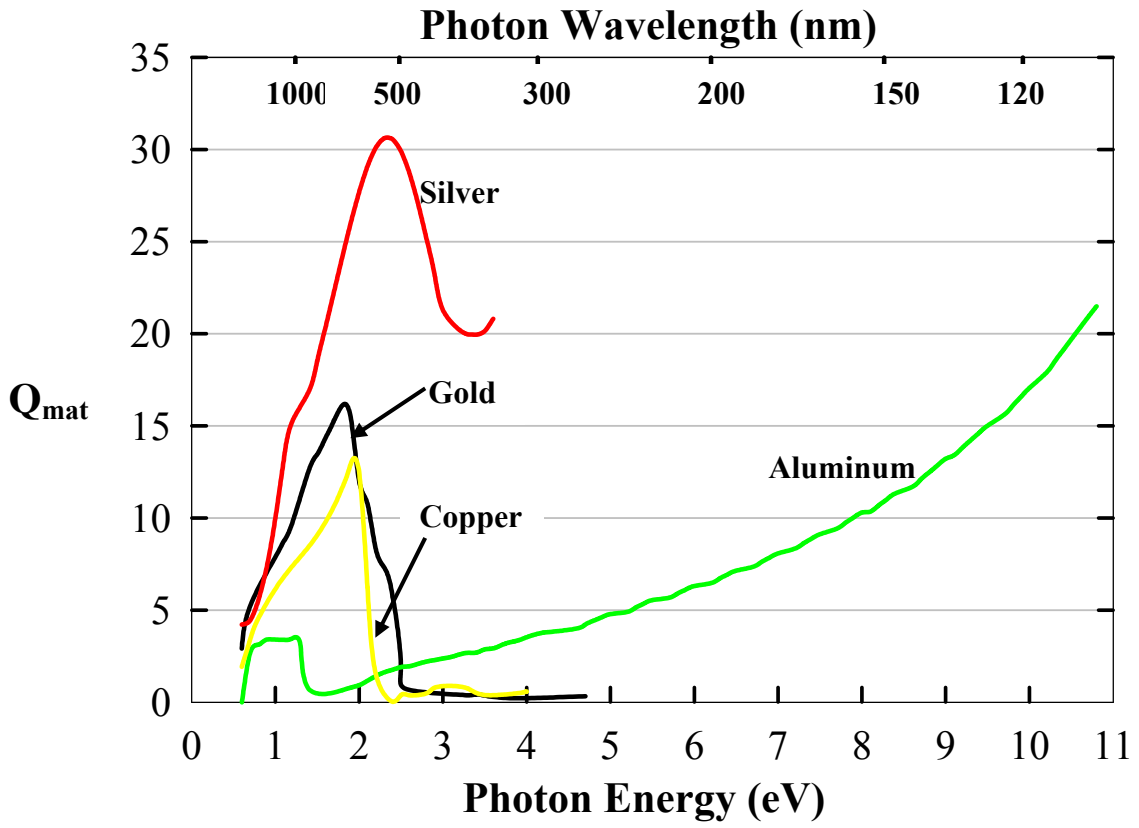

Figure2.3 Material Q of metals that support surface plasmons

The above plot shows why silver is a preferred metal for plasmonic devices. It has the best material Q ~30 in the 2-3eVrange of photon energy.

2.3 Plasmonic lens design

With silver as the metal and silicon dioxide (SiO_2) as the insulator, the real part of Equation2.3 is solved for several thickness of SiO_2 (ε_{SiO2} =2.13). These dispersion plots are shown in Figure2.4 [20]

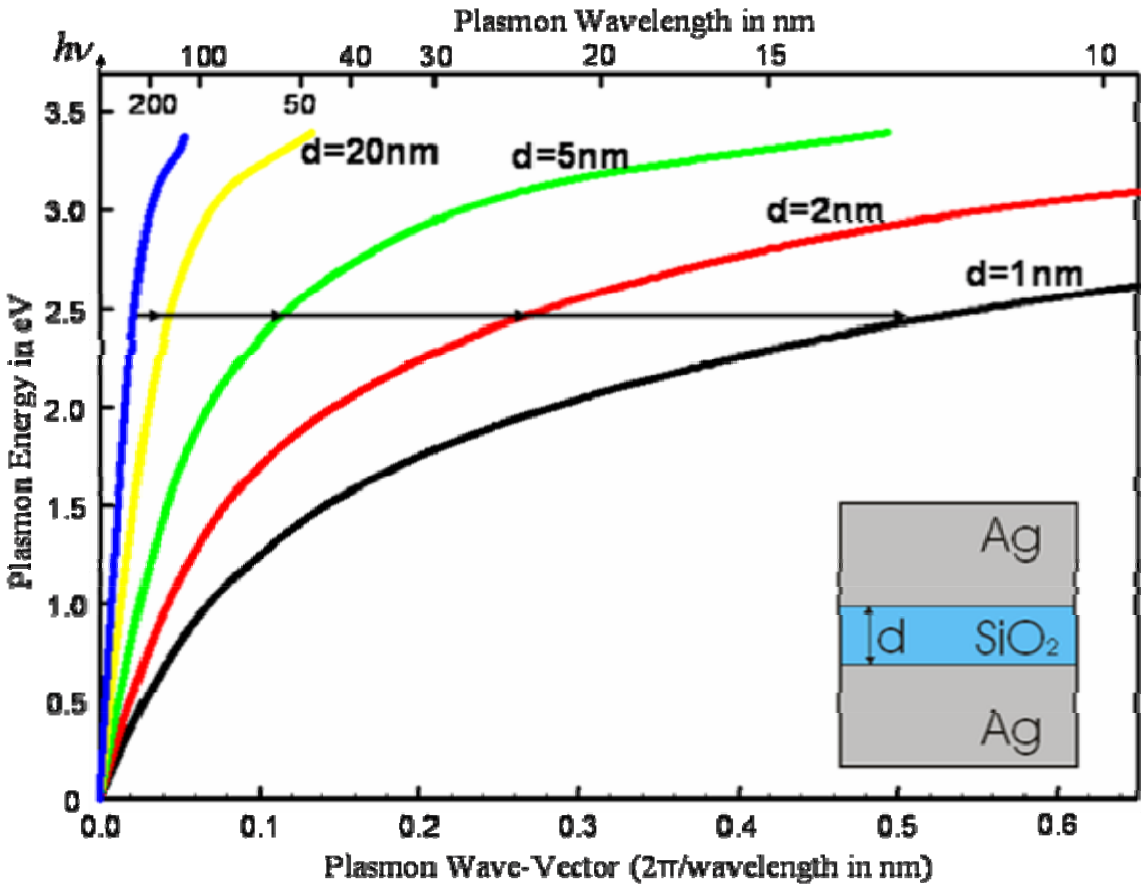

Figure2.4 Dispersion relations for MIM of silver-SiO_2-silver structures with varying thickness of the dielectric

The most striking feature of the above plot is that as the thickness *d* of SiO_2 decreases, plasmons with large propagation vectors can be excited at lower frequencies. Looking at it in another way, light at a given frequency can excite surface plasmons whose wave vectors increase as the thickness of the dielectric decreases. The genesis of a plasmonic lens starts here.

In order to focus the energy from photons to a nanoscale spot size, we need to be able to convert photons into surface plasmons of wavelengths on the order of a few tens of nanometers.

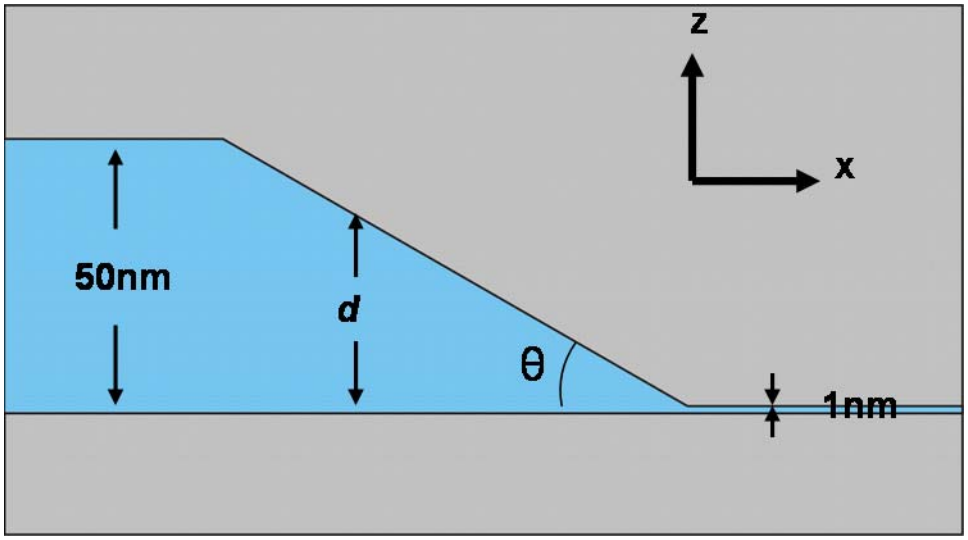

Figure2.5 A possible profile of the MIM structure with the thickness of the dielectric decreasing linearly with distance.

Consider a structure (Figure2.5), where the thickness *d* of the dielectric is reduced from 50nm down to 1nm. When this structure is sandwiched between thick silver, the surface plasmon launched at the 50nm end has larger wavelength (or low k-vector). As this plasmon propagates through a stack, it sees thinner and thinner dielectric. To propagate further in the thinner dielectric region, it needs to assume a shorter wavelength. In process of changing wavelength to adapt to the narrowing dielectric, the surface plasmons with lower wave-vector would experience some amount of backscattering, leading to the loss of power. If the change in the dielectric thickness is rather slow, then the change in plasmon wavelength $\delta\lambda_{sp}/\lambda_{sp}$, is also small. This leads to a negligible backscattering loss. However, the double-sided surface plasmon launched at the 50nm end needs to travel a long distance before it becomes a mode in the 1nm thick dielectric

with very short λ_{sp}. The absorption or the Joule heating losses in the metal increase as the plasmons need to travel longer distance.

Figure2.6 shows the decay lengths of the plasmons when the imaginary part of Equation2.3 is solved [20]. The plot gives the decay lengths (=1/ k''_{sp}) against the plasmon wave vector k'_{sp} for different thickness of the dielectric SiO_2.

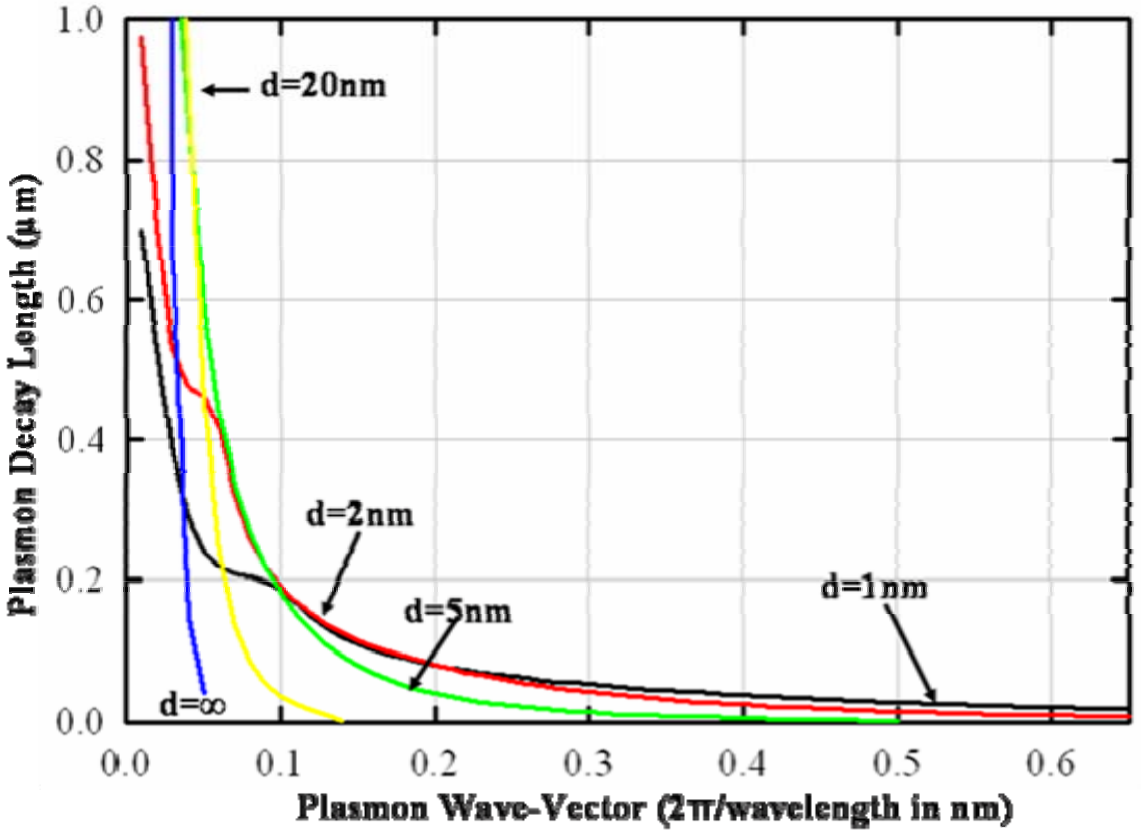

Figure2.6 Log plots (a) Real part of ε'_{silver} (b) Imaginary part of ε''_{silver} as a function of photon energy.

It can be observed that as the dielectric thickness d scales down and k'_{sp} becomes larger, the 1/e decay length of propagation of the plasmons becomes less than 500nm.

This implies that plasmons, from one end plasmonic structure in Figure2.5, cannot propagate very long distances just to minimize backscattering losses.

Figure2.5 has assumed a linear taper in the dielectric with the initial thickness of the dielectric being 50nm and the final thickness 1nm. It turns out that as the surface plasmons assume larger wave-vectors, the $|k_{spz}| \approx k'_{spx}$ (this stems from the relation $k^2_0 = k^2_{spz} + k'^2_{spx}$ and at larger k'_{spx} **,** the vacuum wave-vector k^2_0 becomes much smaller in comparison to the terms on the right hand side). This leads to the simplification of the dispersion relation for double sided plasmons Equation2.3 where the surface plasmon wavelength, decay length and group velocity, all scale linearly with the dielectric thickness *d*. Elegant arguments presented in [21] suggest that a linear taper is best suited for transition of the dielectric thickness from 50nm to 1nm.

In order to balance the backscattering losses against the absorption losses in a liner taper, the angle of the taper needs to be optimized. This optimization has been done using the finite element method. FEMLAB takes a geometric structure, boundary conditions and physical constants as its input. It meshes the structure and computes the field distributions of a structure. The difference between the electromagnetic power flow across the 50nm channel and the 1nm channel, gives the power loss through as the plasmon mode propagates through the taper. More details on the FEMLAB computation are present in [22].

Figure2.7 is a plot of power loss across the taper versus the angle of the taper.

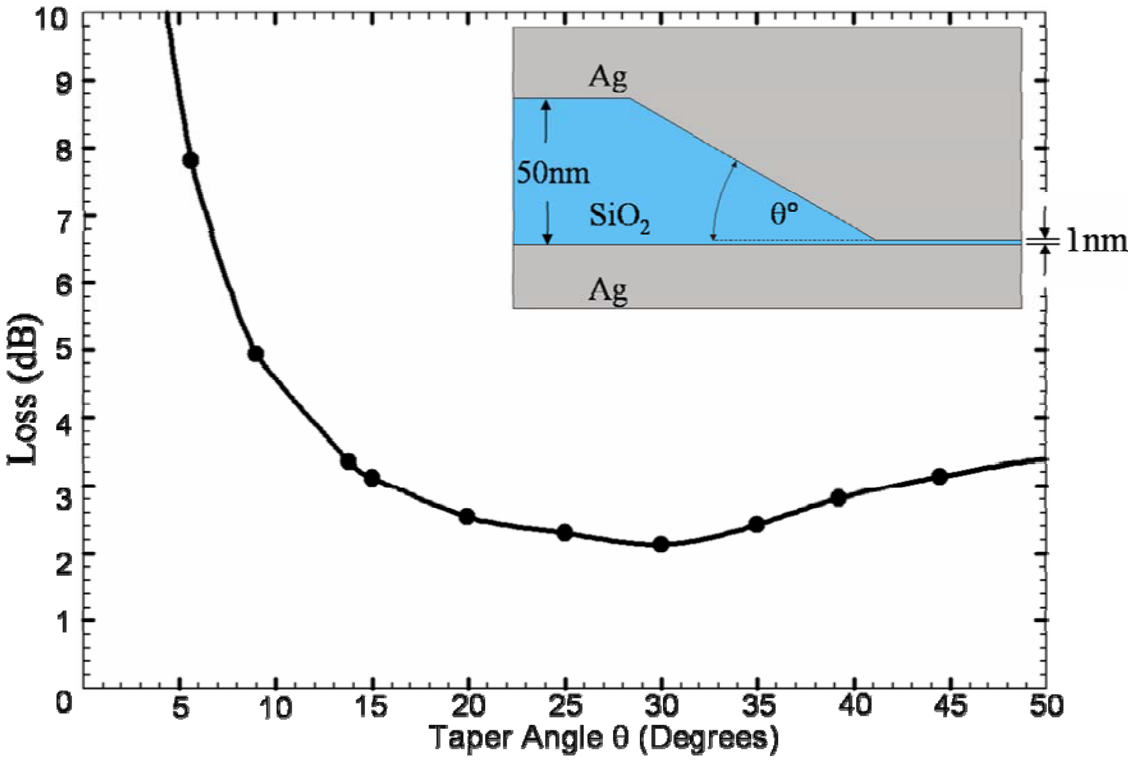

Figure2.7 Loss through the taper vs taper angle

It turns out the in the range of 20°-40° losses are pretty low, with the minimum loss occurring at a taper angle of 30°.

2.4 Energy confinement and focusing

The taper structure as depicted in Figure2.5 achieves energy confinement in two dimensions, *x* and *z*.

- In direction of propagation, *x*, the group velocity of the surface plasmon modes decreases as the plasmons propagate towards the thinnest part of the structure. This causes the energy flow to slow down and energy density increases as we move to shorter plasmon wavelengths.

- In the direction transverse to propagation, *z*, energy is confined as a result of decrease in the transverse modal size of the surface plasmon. The penetration of the field into the metal is determined by inverse of $|k_{spz}|$. At large wave vectors, it has already been discussed that $|k_{spz}| \approx k'_{spx}$. Hence the mode penetrates very little into the metal. It is estimated that the modal size of the energy of the surface plasmon is about 2.6nm with the terminal dielectric thickness of 1nm [22, 23].

- To achieve focusing in the third dimension, y, and the two-dimensional taper shown in Figure2.5 is revolved around a focal point. This gives us a dimple with circular symmetry as depicted in Figure2.8. The large k-vectors achieved by tapering the dielectric down to 1nm, are brought into focus due the circular geometry. The focusing achieved in this dimension is theoretically equal to the λ_{sp}(at d=1nm) / 2 which comes to about 5nm.

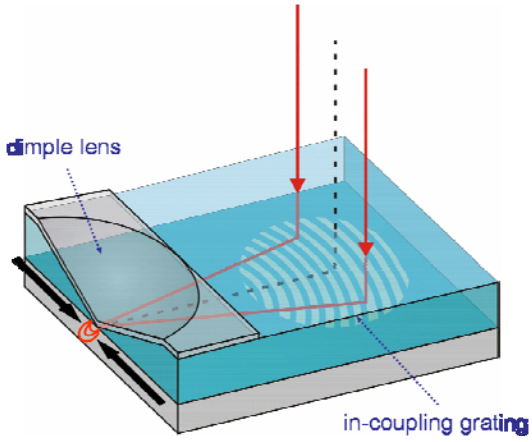

Figure2.8 Three dimensional plasmonic lens

The energy confinement in the three dimensions as discussed, gives rise to enhancement of the electric field. Apart from the enhancement that is achieved by converting a free space photon in a Gaussian mode into surface plasmon, the estimated field enhancement due to the confinement of energy in the *x* and *z* directions is about 340 and that in the y-direction is 140. For details please refer to [24].

All along we focused on the Metal-Insulator-Metal (MIM) geometry over its complementary Insulator-Metal-Insulator (IMI) geometry. Both these geometries have similar dispersion relations. From the dispersion relations it turns out that the thickness of the dielectric *d* in the MIM geometry or the thickness of the metal in the IMI geometry determines the shortest achievable surface plasmon wavelength and energy confinement. The justification of choosing the MIM geometry comes from the fact that to get a continuous silver film down to a thickness of <5nm with reasonably good surface roughness because evaporated silver tends to form islands on a dielectric substrate. On the other hand, very thin and smooth amorphous silicon oxide [25] or silicon nitride films [26] are a standard in the IC fabrication industry. These films are grown on crystalline silicon substrate. Removal of silicon substrate and sandwiching the dielectric film between silver is a fabrication challenge dealt with in Section 4.5.

Thus up to this point, this chapter presents the evolution of a plasmonic lens structure from the characteristics of double-sided surface plasmons on the slab MIM

geometry that helps us achieve nanoscopic energy confinement with a very low loss across the taper.

2.5 Transmission line analysis of plasmonic dimple lens

A novel plasmonic lens design has been developed in the previous sections of this chapter. However, it is important to note that guiding and focusing surface plasmons is not the only way to obtain to high concentration of electric field energy on nanoscale. There are several other structures of dimensions on the scales of wavelength as well as sub-wavelength, which seem to achieve focusing of optical energy. Some of the representative candidates are shown in Figure2.9 and Figure2.10. The first class of structures is half-wave dipole or quarter-wave monopole structures. These antenna structures are on the size of a wavelength, which enable them to efficiently capture the impinging radiation and focus it at a sharp point(s). The other class of structures comprises of slots drilled into a sheet of metal. Here the optical field is focused at the smallest separation in the metallic slot [27-29].

In order to gain a fundamental understanding with regard to sub-wavelength optics without seemingly involving the surface plasmonic modes, we turn our attention to concept introduced in Section 1.2. The last chapter briefly discussed about application of the lumped circuit theory concepts to sub-wavelength regime electromagnetics with the rationale being that the lumped circuit elements are much smaller than the wavelength of operation and that the field distributions associated with them are quasistatic. We now

consider circuits whose size is comparable to the wavelength of operation. These circuits cannot be modeled with a single lumped inductor, capacitor, or resistor because the fields associated with these elements will have spatial variations on the order of a wavelength. The impedance of such a circuit is spread over the entire dimension of the circuit. However, we can still break up this circuit into small segments that are much smaller than the wavelength. Each of these segments can be modeled as a collection of lumped impedance elements, each with a quasistatic field distribution that is different from that of the adjoining segment. Thus each segment can be associated with a voltage and current that varies as across the segments. This kind of a circuit is called a distributed circuit, however one can still use the concepts developed for the lumped circuit analysis.

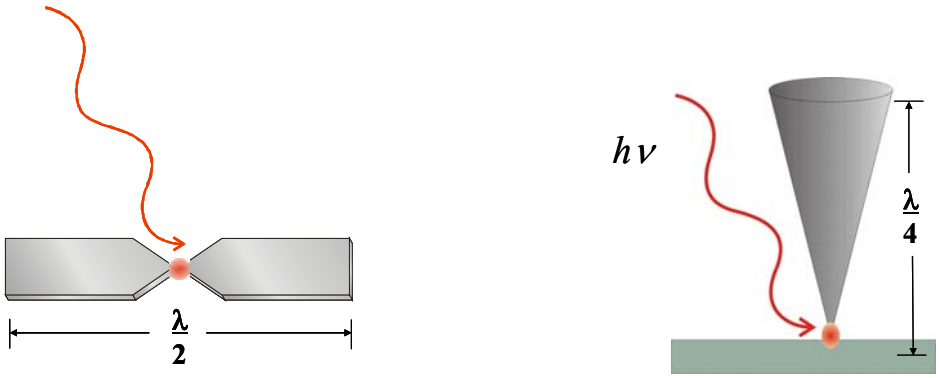

Figure2.9 (Left) Half-wave dipole bow-tie antenna, (Right) Quarter-wave monopole antenna

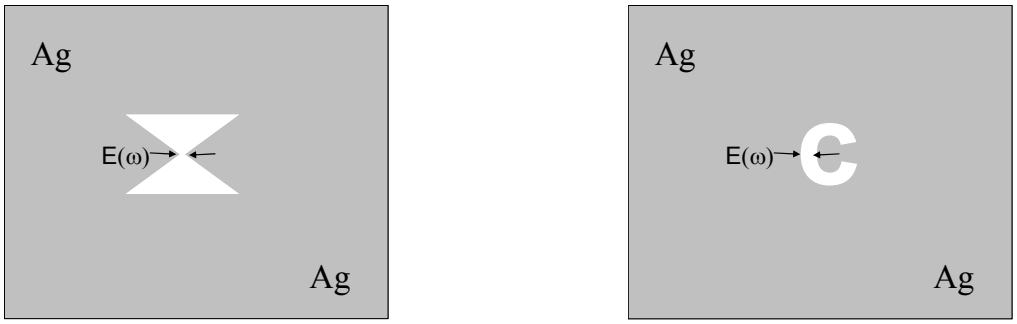

Figure2.10 Slot antennas: (Left) Bow-tie and (Right) C-shape

A transmission line, often discussed in the context of microwave frequency regime, is a classic example of a distributed circuit. An ideal transmission line (in Figure2.11) is at least on the order of wavelength of operation, guides electromagnetic energy along its longest dimension, and can be modeled with a series of inductors and capacitors that propagate the electromagnetic fields along its length.

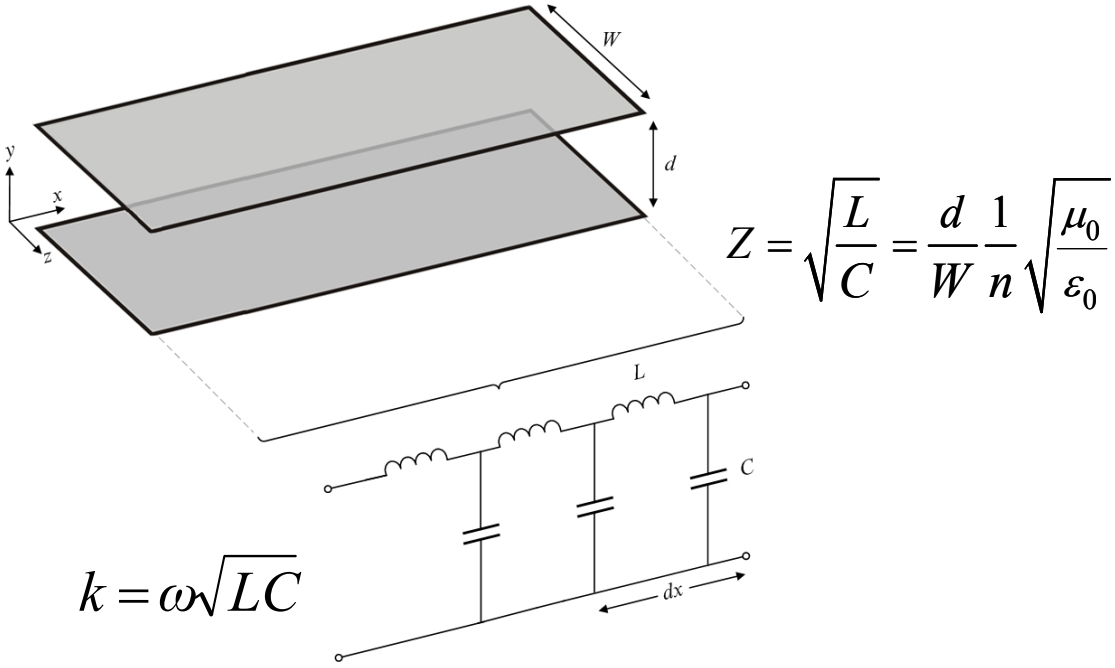

Figure2.11 A parallel plate transmission line as a distributed circuit.

A parallel plate transmission line is characterize by the propagation vector k and characteristic impedance Z, both of which are governed by the inductance and capacitance per unit length which in turn depends on the dimensions of the transmission line.

Our plasmonic dimple lens designed in the previous sections of this chapter resembles the tapered parallel plate transmission line in structure as seen in Figure2.12 Metal plates that sandwich a tapered dielectric layer bind both the structures.

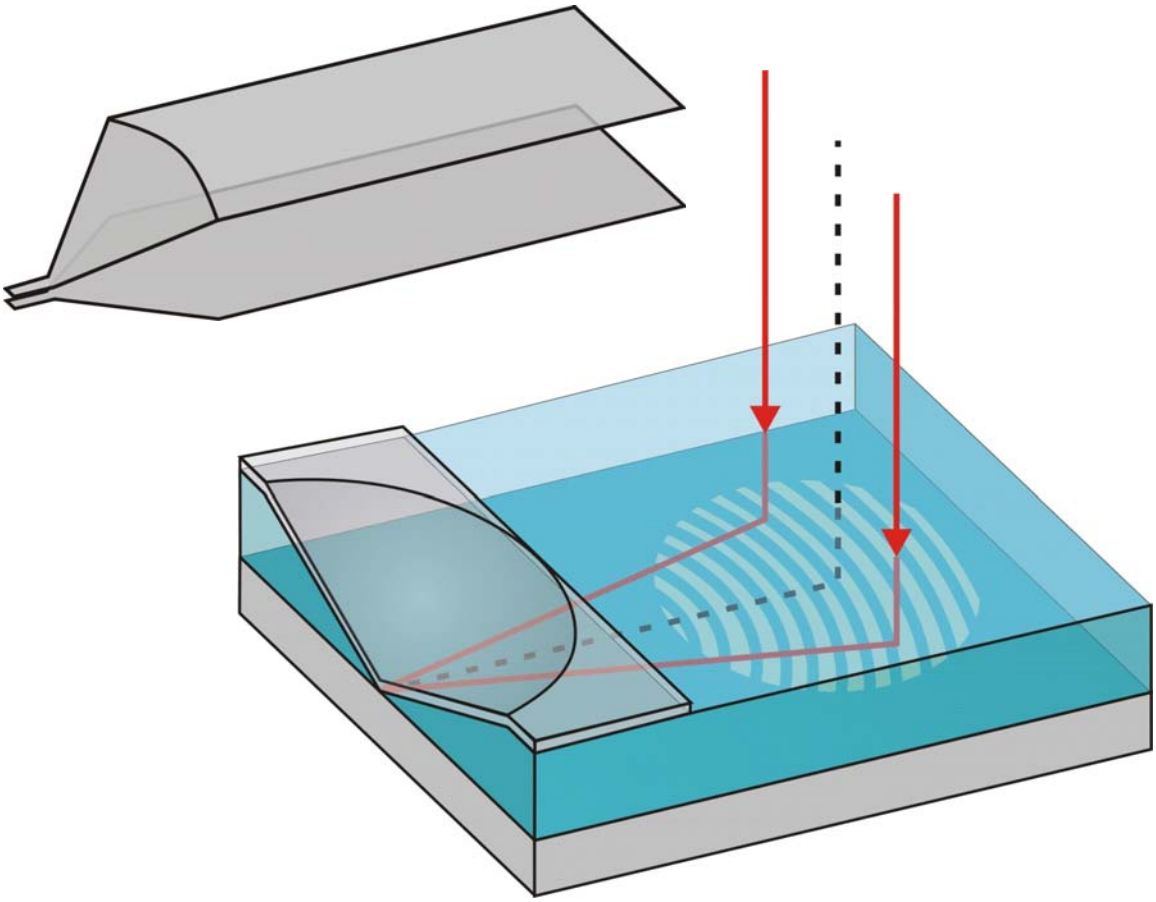

Figure2.12 (upper) A 3D tapered parallel plate transmission line, (lower) plasmonic dimple lens.

We re-examine the dispersion relation of a silver-SiO_2-silver MIM slab structure seen in Figure2.5. It can be easily observed that the dispersion relation of a double-sided plasmon of a large dielectric thickness *d* denoted by the blue curve is almost a straight line (that nearly looks like that of a free space photon). In terms of the aforementioned transmission line analysis, it appears that the propagation vector *k* of blue curve is

represented by $k = \omega\sqrt{LC}$. And the propagation vectors of all the other curves governing the thinner dielectric MIM slabs, can be given by the expression $k = \omega\sqrt{(L + L')/C}$, where L' is some additional inductance. It can be immediately recalled that in section 1.2 we discussed about a new form of inductance called the kinetic inductance that would be significant in comparison to the faraday inductance L at higher frequencies and smaller physical dimensions. Since the slope (given by ω/k) of other curves (of smaller dielectric thickness d) is smaller than the one for the blue curve (of the largest dielectric thickness d), we can conclude that L' denotes the kinetic inductance.

2.6 A new impedance plot

This section discusses the dominant impedance involved in the analysis of a parallel plate MIM structure in the form of Ag-air-Ag. As discussed in section 1.2, there are three types of impedances to the flow of current in a MIM parallel plate structure namely resistance R, faraday inductance L_f, and kinetic inductance L_k. In a specific frequency range and for a given physical dimension d, the dielectric thickness or the plate separation of a MIM slab structure, one of these impedances dominates as shown in Figure2.13.

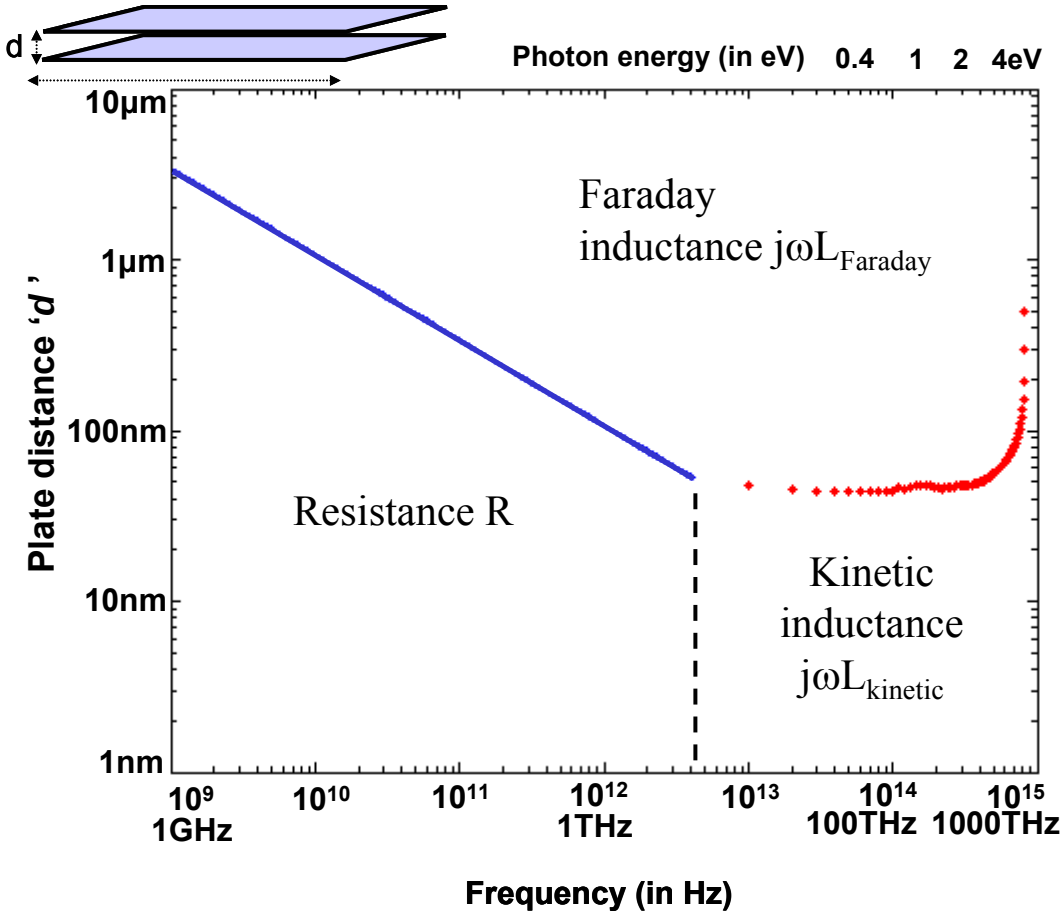

Figure2.13 A dominant-impedance plot of a silver wire in different length-scale vs frequency regimes

The expression for each of the impedances is given by the following.

$$L_k = \frac{1}{\omega^2 \varepsilon_0 (1 - \varepsilon_r'(\omega))} \frac{(length)}{(area)}$$

$$R = \frac{\varepsilon_r''(\omega)}{\omega \ \varepsilon_0 \left|1 - \varepsilon_r'(\omega)\right|^2} \frac{(length)}{(area)}$$

$$L_f = \frac{\mu_0 d}{W}(length) \qquad \text{and} \qquad area = W\delta$$

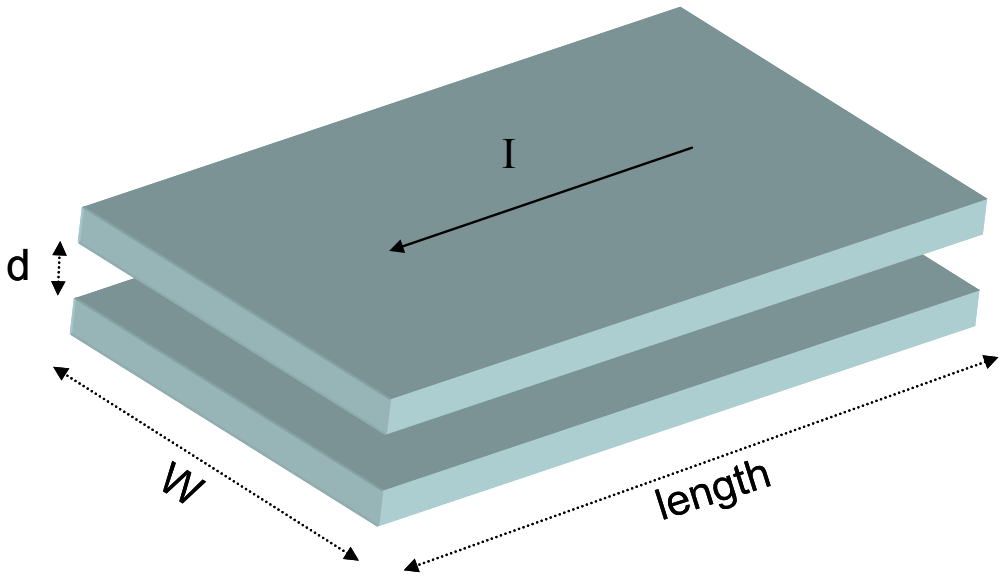

- The boundary between ωL_k and R is determined by equating the expressions of the two. The frequency at which $(1-\varepsilon_r'(f))$ equals $\varepsilon_r''(f)$ for silver is 4.12 THz [30].
- The boundary between R and L_f is determined from the expression $\delta = \sqrt{2/(\omega\sigma\mu_0)}$ where conductivity $\sigma = 6.17\times10^7$ where δ is the skin depth of penetration of the electromagnetic fields in silver [31]. In the resistive regime, finite conductivity of a metal arises from the energy loss due to electron-lattice collisions. Hence this skin depth δ is also known as $\delta_{collisional}$
- There are two approaches to determine the boundary between L_k and L_f
    - The first approach is to equate the expressions for L_k and L_f as given above. So we get, $W\delta = \dfrac{1}{\omega^2\mu_0\varepsilon_0(1-\varepsilon_r'(\omega))} = \dfrac{c^2}{\omega^2(1-\varepsilon_r'(\omega))} = \dfrac{k^2}{(1-\varepsilon_r'(\omega))}$

Since we are analyzing a 2D tapered transmission line (use Figure2.11 and upper one in Figure2.12), we consider the case of $W=d$ and the above expression simplifies to $d=\delta$, and we get $\frac{k^2}{(1-\varepsilon_r'(\omega))} = \delta^2$

Note that the δ here is the collisionless skin depth of silver at these high frequencies. It is important to note that physically δ is the *1/e* penetration depth of the electric field of an incident photon (of momentum k_0) that impinges normally on the metallic surface. This means that k_0 does NOT have any component parallel to the metal surface. The impedance plot generated for this case is shown in Figure2.14

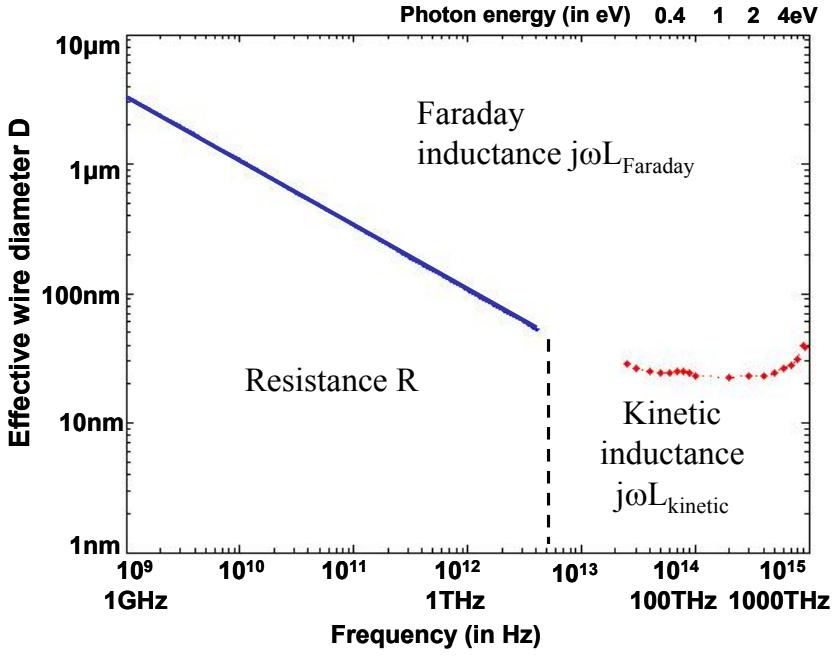

Figure2.14 A dominant-impedance plot of a silver wire in different length-scale vs frequency regimes → L_k and L_f boundary determined by collisionless skin depth

- Surface plasmons have a large component of their momentum k_0 in the direction parallel to the metallic surface particularly at high optical frequencies. So now, δ, the penetration of surface plasmonic fields into the metal is different from that of $\delta_{collisionless}$ discussed in the previous case.

  Hence the approach to determine the boundary between L_k and L_f in this context, is by solving for the value of d in Equation2.3 where the metal is silver, the dielectric (or insulator) is air, and $k_{sp} = \sqrt{2}\, k_0$. The $\sqrt{2}$ comes from the expression $k = \omega\sqrt{(L + L')/C}$ when $L = L'$ (or equivalently $L_k = L_f$). This value of d is plotted as the demarcation between L_k and L_f in Figure2.13. Note that this demarcation rises but much steeply than that in Figure2.14 towards the surface plasmon resonance frequencies towards the extreme right of the plot.

2.7 Energy transfer efficiency

Finally, it is interesting to note that focusing energy in a tapered transmission line structure is quite efficient and this can be deduced from the circuit model of transmission line.

The characteristic impedance of a parallel plate MIM structure (Figure2.11) $Z = \sqrt{\frac{L}{C}} = \frac{d}{W}\frac{1}{n}\sqrt{\frac{\mu_0}{\varepsilon_0}}$ depends on the aspect ratio d / W where L is the conventional faraday

inductance L_f. For a given width of the transmission line W, the characteristic impedance Z falls as the dimension of the waveguide d decreases. The resistance R significantly increases owing to the decrease in the cross-sectional area $W\delta$ because the decrease in the dimension d of a parallel plate transmission line structure lowers the penetration depth δ of the surface plasmons into the metal plates. Hence in this case it follows that the energy transfer efficiency as seen from Figure2.15 falls rapidly towards nanoscale.

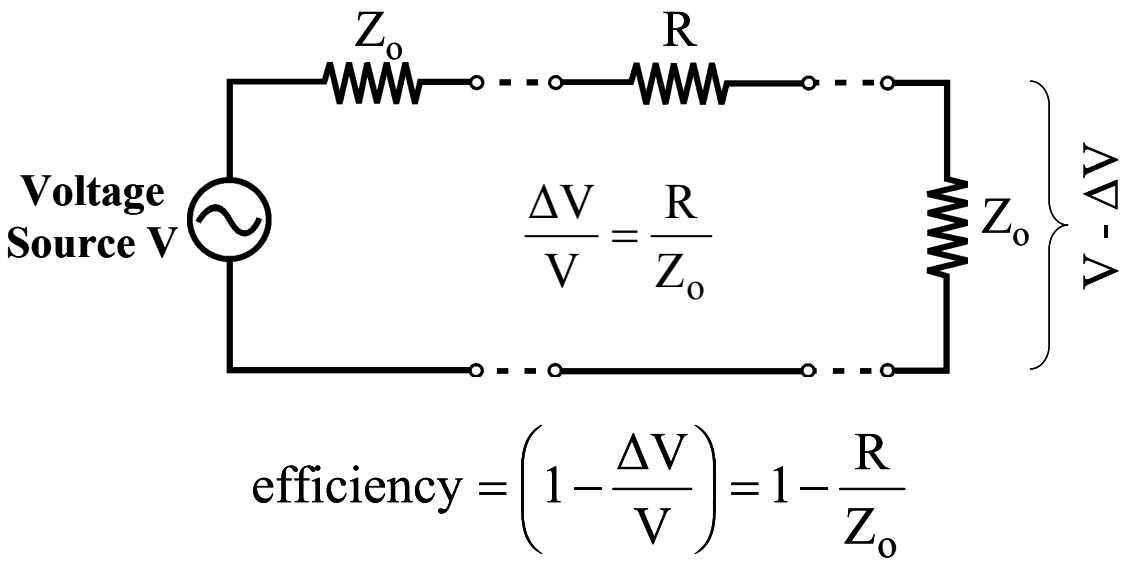

Figure2.15 A transmission line model depicting energy efficiency

Now we study the case when the width W of the parallel plate transmission line scales down to nanometric regime along with d. When operating at near surface-plasmon resonance frequencies at the nanoscale of small dielectric thickness d, we have established from the previous Section 2.6 that $Z \approx \sqrt{\frac{L_k}{C}}$. With $C = \varepsilon_0 \frac{W}{d}$ and using the expression of L_k from the

previous section, we get $Z \approx \frac{1}{W}\sqrt{\frac{2}{\omega^2 {\varepsilon_0}^2 \left(1-\varepsilon_r'\right)} \cdot \frac{d}{\delta}}$. At the scales where L_k becomes significant, δ is very much on the order of d (in the limit of being equal to d).

Thus it is possible to boost the value of Z by scaling down W along with d which boosts the efficiency of power transfer. And this is precisely what occurs in a semi-circular plasmonic dimple lens as we have already established its equivalence to a tapering transmission line in Figure2.12. The efficient energy transfer in a tapered transmission line validates the simulation result obtained by finite element simulation in Figure2.7 [22].

Chapter 3 Preliminary Experiments

This chapter outlines the experimental details of characterizing the optical dielectric constants of thin silver films and the characterization of a grating in-coupler.

3.1 Dielectric constants of silver

In Section2.2, the dispersion of dielectric constants of silver is discussed. The propagation vectors of double-sided surface plasmons in plasmonic lens depend on the values of the dielectric constants. The fabrication of the plasmonic lens would involve evaporation of metallic silver on dielectric layer. The evaporated silver is polycrystalline in nature. The grains are on the order 100-150nm in size. The presence of grain boundaries in the thin films of silver could result in greater scattering of light, hence more loss in addition to the absorption losses of the metal. Therefore it is important to determine the dielectric constants of the evaporated silver to validate it with the ones used for the design of plasmonic lens.

Consider a film of silver on a glass substrate. The air-silver-glass stack forms an IMI surface where single-sided surface plasmons can be launched on both silver-air and silver-glass interface. If the silver film is thin enough, then a double-sided plasmon can be launched into this structure. From Figure 1.2, the dispersion relation for a surface plasmon always lies to the right of the light line. This implies that the wave vector of a surface plasmon is greater than the wave vector of the photon in the insulator. So in order

to couple a photon to a surface plasmon, some kind of momentum (or wave-vector matching) is required.

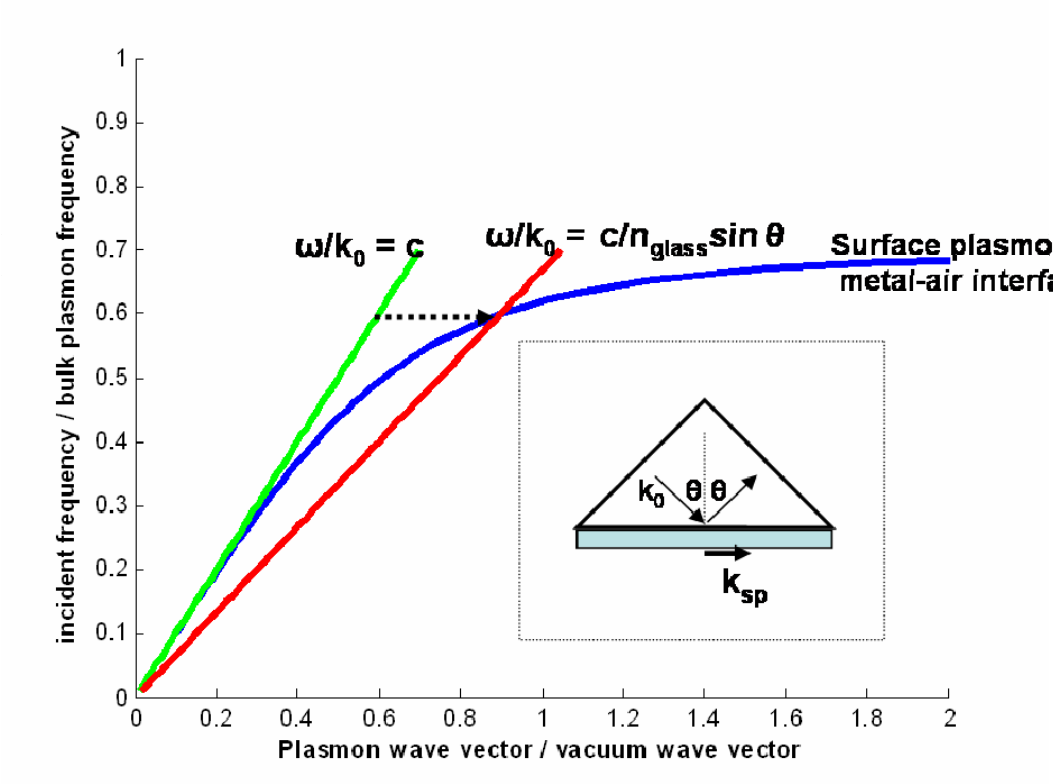

Figure3.1 Principle of Attenuated Total internal Reflection (ATR) method. The dotted line shows the momentum mismatch between photon in air and surface plasmon (SP). (Inset) Kretchmann configuration of lauching SPs

From Figure3.1, it can be seen that the surface plasmon at the silver-air interface intersects with the light line in the glass. This implies that the wave vector of a photon in glass would be equal to the wave vector required to launch a plasmon at the silver-air interface. This would also imply that the photon traveling through the glass needs to

penetrate through the thickness of the silver film to reach the silver-air interface on the other side of the silver.

This method of excitation of surface plasmons is called Kretchmann configuration where the evanescent wave from total internal reflection at the glass-silver interface, penetrates through the thin silver film and couples into the surface plasmon mode at the silver-air interface (Figure3.1 inset) [32]. A triangular, a semi-cylindrical, or a hemispherical prism may be used launch light from air into glass without losing much light to Fresnal reflections at the air-glass interface and to be able to get the reflected beam out of glass without encountering the critical angle at the glass-air interface.

A right angled glass prism is cleaned in a mixture of $HCl+H_2O_2+H_2O$ (1:1:5) at 80°C for 10minutes followed by another 10minutes in a mixture of $NH_4OH+H_2O_2+H_2O$ (1:1:5) at 80°C to clean the sample from inorganic and organic residue. It is then placed in electron beam evaporator where silver is evaporated at a pressure of 10^{-6} torr. The freshly made sample is used for collecting data from the experimental setup shown in Figure3.2

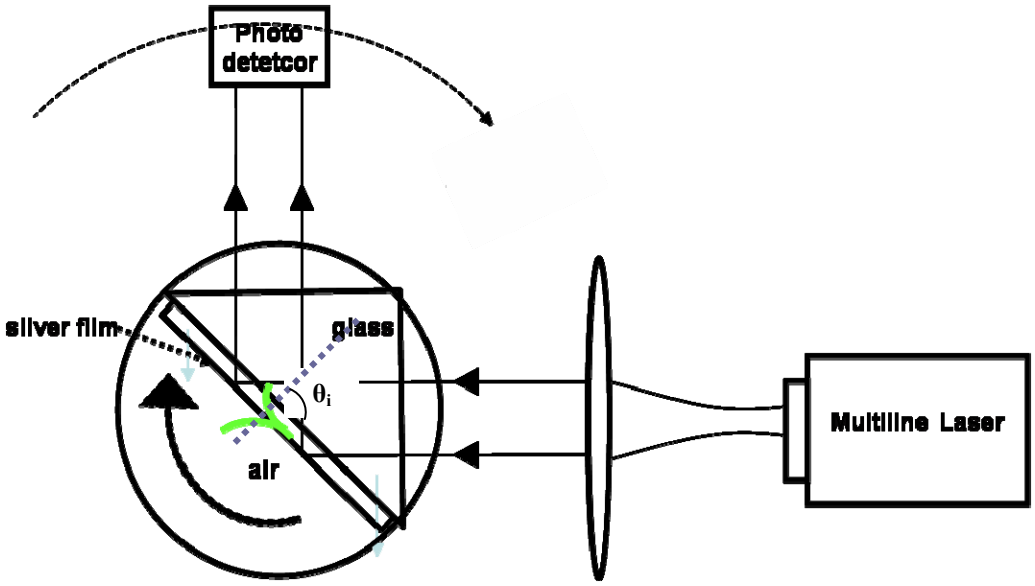

Figure3.2 Experimental setup to launch surface plasmons by ATR method. The green line depicts the surface plasmon at silver-air interface

The multi-line laser used is an Ar-Kr ion laser has laser emission at 476nm, 488nm, 514nm, 568nm and 647nm. The laser light is expanded using a collimating lens. The silver coated prism is mounted on a rotational stage with the laser beam incident on one face of the prism. The reflected beam intensity is recorded by a silicon photodetector. As the prism is rotated, the angle of incidence changes, and the intensity of the reflected beam also changes. Care must be taken to ensure that the reflected beam is normally incident on the central region of the photo detector. At a specific angle of incidence, the tangential component of the photon wave vector from glass is close to the propagation vector of the single sided plasmon that can exist in the air-silver interface. At this angle, the power gets coupled into plasmon and thereby a dip in the reflected power is observed.

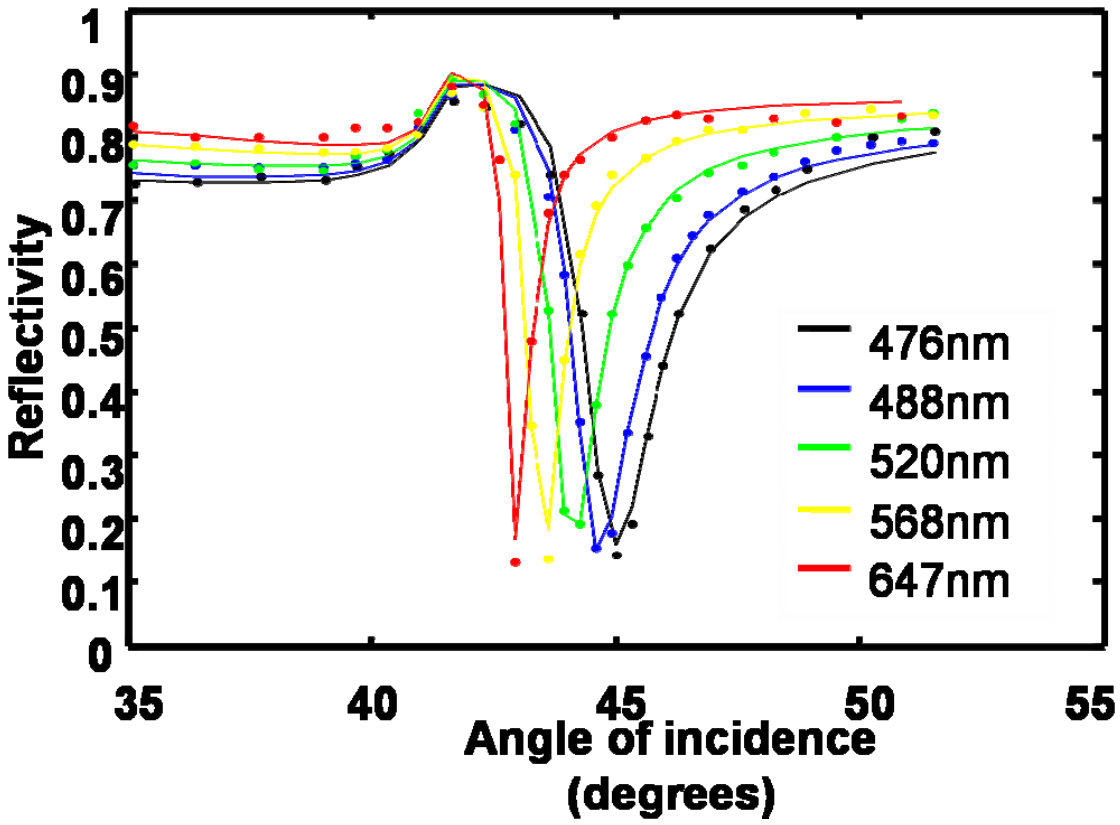

Figure3.3 Experimental data of the ATR reflectivity dips at different wavelengths

- It can be observed that dips in reflectivity at all the wavelengths occur at an angle of incidence greater than 42°, which is the critical angle for the glass-air interface. Hence this method of launching surface plasmons is called ATR (Attenuated Total internal Reflection) method.
- As the frequency of incident light increases, the dip in reflectivity occurs at larger angles. This implies that the tangential component of incident light is larger for higher frequencies. This is precisely what one would expect from the dispersion relations single sided surface plasmons (Figure3.1).

- As the frequency of light increases, the FWHM of the reflectivity dip increases, indicating an increase in the losses. The Q for these plots is ~50.

A MATLAB code was written to fit the data with ε'_{silver} and ε''_{silver} and film thickness.

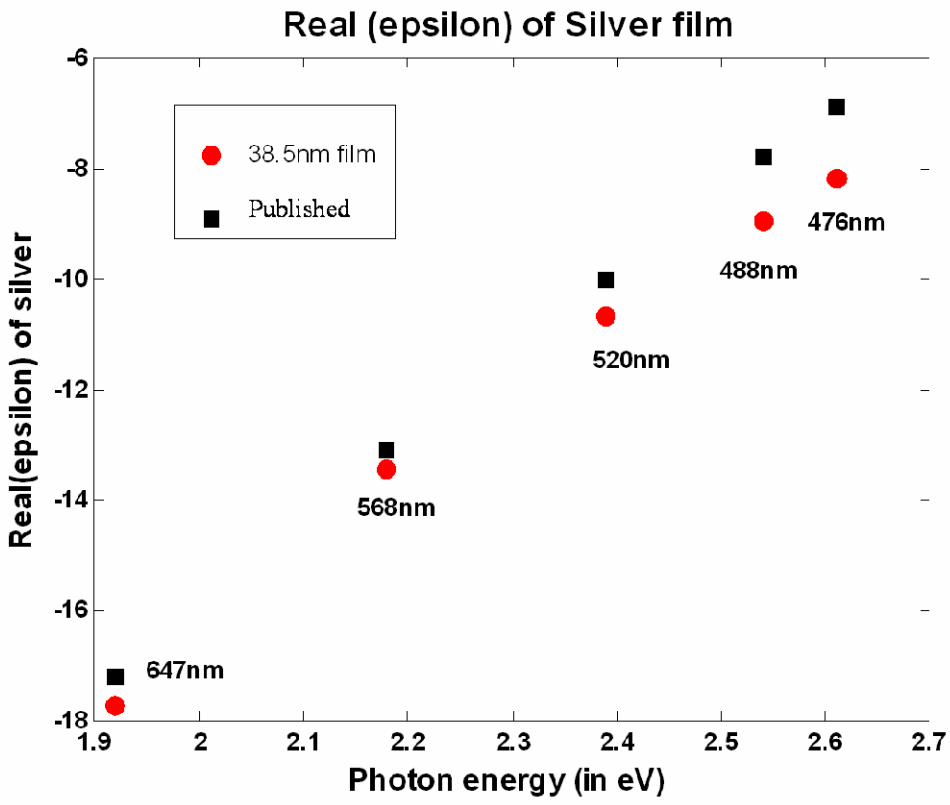

Figure3.4 Real part of dielectric constant of silver (ε'_{silver}) extracted from data in Figure3.2

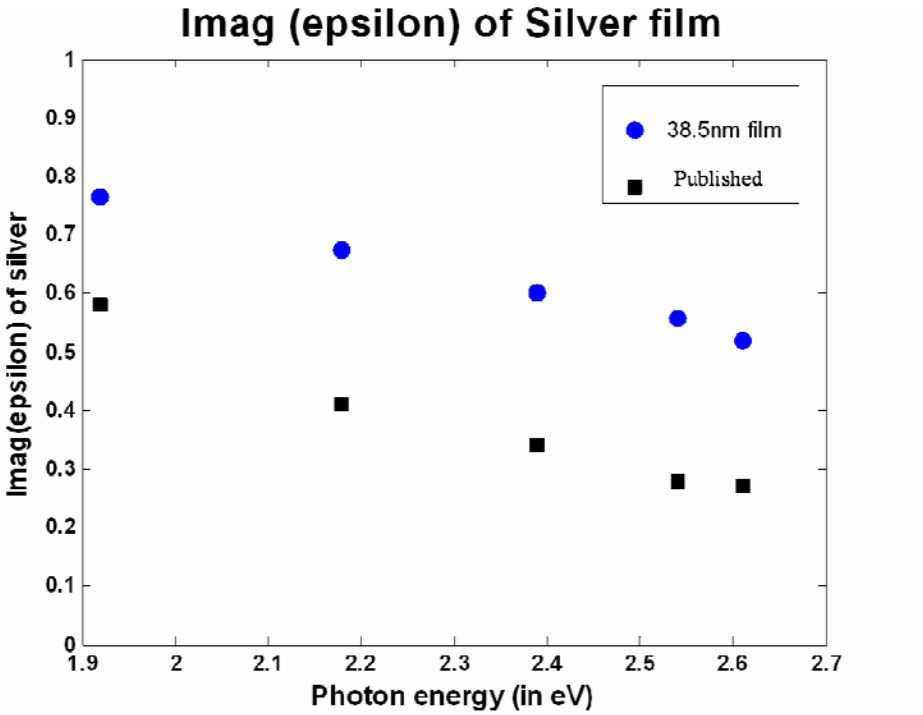

Figure3.5 Imaginary part of dielectric constant of silver (ε''_{silver}) extracted from data in Figure3.2

These plots indicate that the real part of the dielectric constant ε'_{silver} correlates well with the published values in the literature where as the imaginary part ε''_{silver} is more than the published values. The reason for this could be because the film thickness used in this experiment could be thinner than that used in the published literature [33]. Also the method of deposition could be different in both the cases which give rise to different grain structure, thereby different losses. The conclusion is that thin silver films are lossier than the thicker ones.

3.2 Coupling photons to surface plasmons

Section 2.2 discussed about the design of the plasmonic lens. The crux of the design was the tapering thickness of the dielectric in the MIM geometry which would cause the energy to focus down at high vectors. Simulations showed that the design was efficient with a 30° taper angle with the losses being about 2dB across the taper. This was the loss incurred by a double-sided surface plasmon from 50nm thick region to 1nm thick dielectric region.

It is equally important to have good in-coupling efficiency from the free space photons into single sided or double-sided plasmons. From the surface plasmon dispersion relation we have seen that there is a momentum mismatch between a free space photon and a plasmon. So we need to have a structure, which provides the requisite momentum.

In order to couple one mode into another, one mode needs to experience a small perturbation in the dielectric constant ε as function of spatial distance *r* along the direction of propagation of the mode. The spatial frequencies that make up the spatial perturbation of ε(*r*) provide the momentum required by one mode to be coupled in to another mode. The strength of coupling depends upon the modal overlap of the two modes via the perturbation ε(*r*).

A surface grating coupler is a periodic perturbation of ε(*r*) with a period Λ (= $1/K_g$ where K_g is the wave-vector of the grating). Consider a surface with a surface grating coupler of period Λ in silver as depicted in Figure3.5. If light is incident on this grating at an angle θ, and it is required that a surface plasmon of propagation vector k_{sp} be generated, then the phase matching condition is $k_0 sin\theta + K_g = k_{sp}$

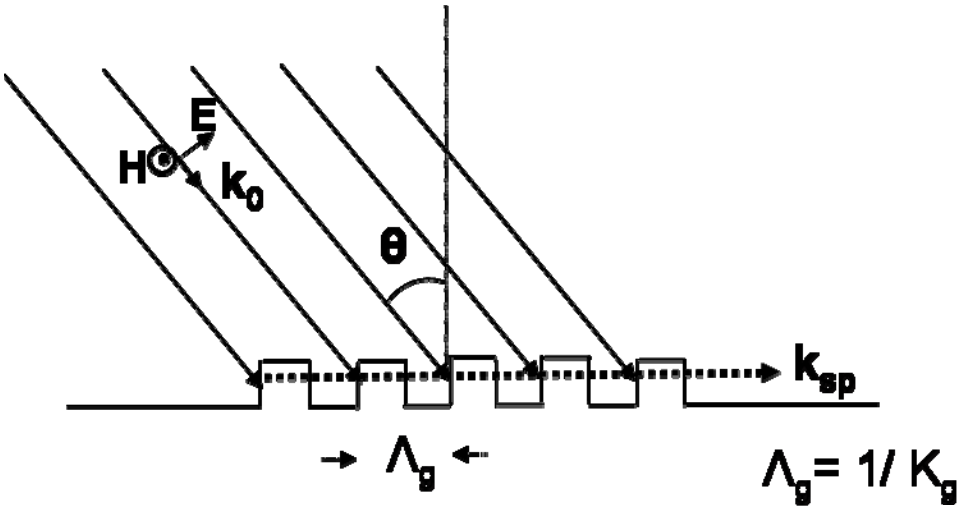

Figure3.6 Phase matching in a surface grating coupler

Another method of in-coupling photons into plasmons in the plasmonic lens geometry can be termed as end fire coupling. Figure3.6 shows the schematic of end fire coupling. Here the perturbation in $\varepsilon(r)$ is a step function with $\varepsilon(r) = \varepsilon_{dielectric}$ about the interface and $\varepsilon(r) = \varepsilon_{metal}$ below the interface.

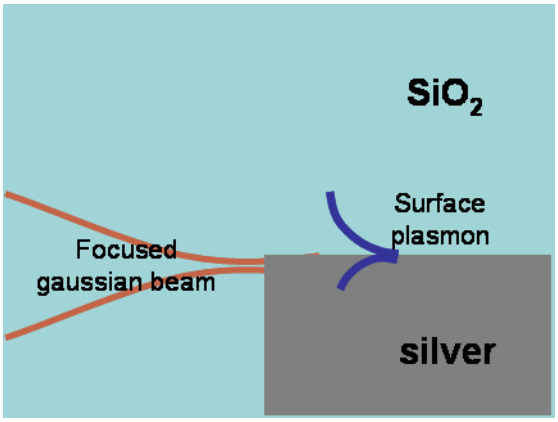

Figure3.7 End fire coupling at a silver-SiO_2 step

The efficiency of the end fire coupling depends on the size and position of the incident beam. Simulations show that an efficiency of ~45% for end fire coupling as for a focused beam width of 260nm at a free space wavelength 488nm [34].

3.3 Surface grating coupler

A one dimensional grating consists of periodic lines on a substrate. This provides a grating vector perpendicular to the lines/grooves of the grating. In order to launch surface plasmons, the polarization of the incident radiation should have a component along the grating vector (i.e. perpendicular to the grating lines) as shown in Figure3.5 because surface plasmons can be generated on by photonic excitation in the TM polarization.

A 400μm x 400μm with a grating period of 440nm is fabricated at silver-glass interface to characterize the coupling of light into surface plasmons. Figure3.7 outlines the fabrication sequence. Figure3.8 shows the SEM image of the grating.

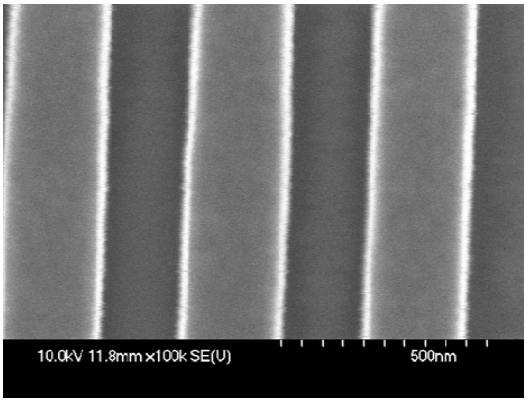

Figure3.8 Scanning electron micrograph of a 1D grating with a period of 440nm and 50% duty cycle.

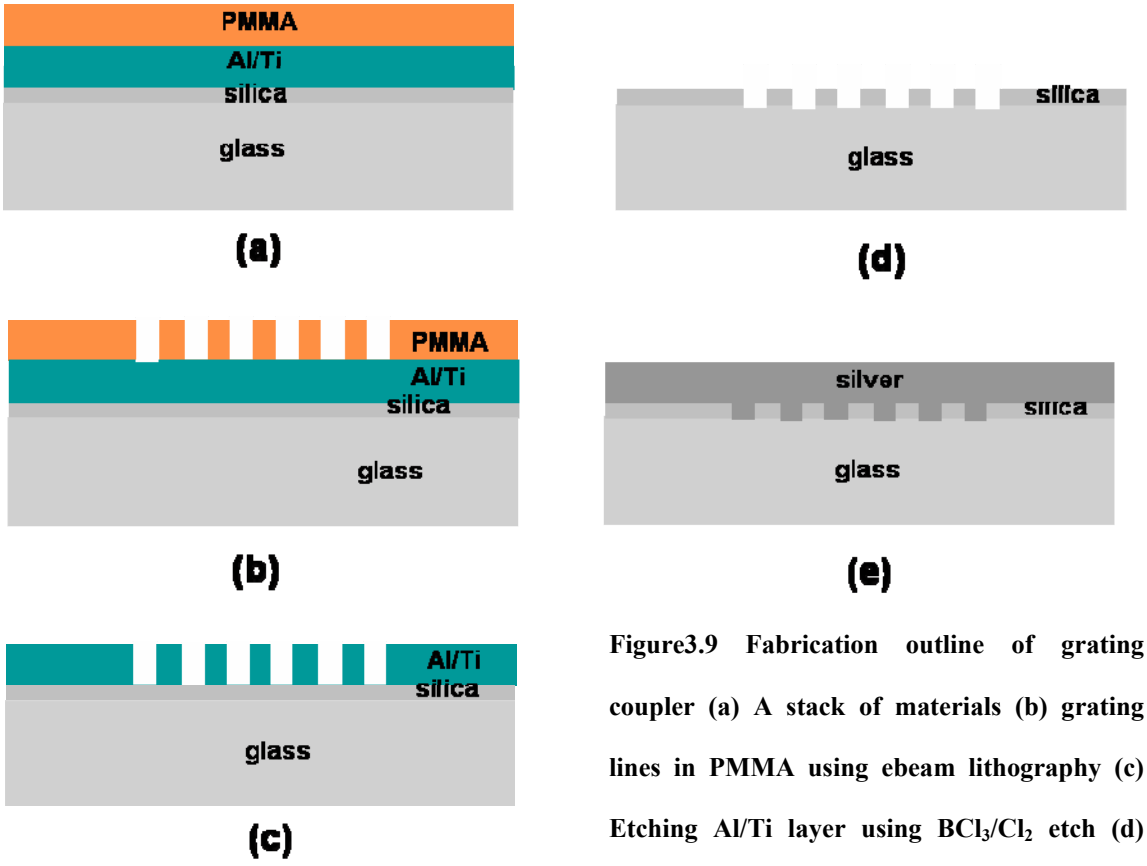

Figure3.9 Fabrication outline of grating coupler (a) A stack of materials (b) grating lines in PMMA using ebeam lithography (c) Etching Al/Ti layer using BCl_3/Cl_2 etch (d) Etching of evaporated silica layer using RIE (e) Evaporation of silver on the sample

Figure3.9 shows the experimental setup used to characterize the grating coupler. Once again the sample is mounted on a rotational stage with the light being incident on glass side of the sample. As the sample is rotated, the intensity of the reflected beam is recorded. A polarizer and a half-wave plate help to rotate the laser polarization to TE (s or σ) and TM (p or π) polarizations.

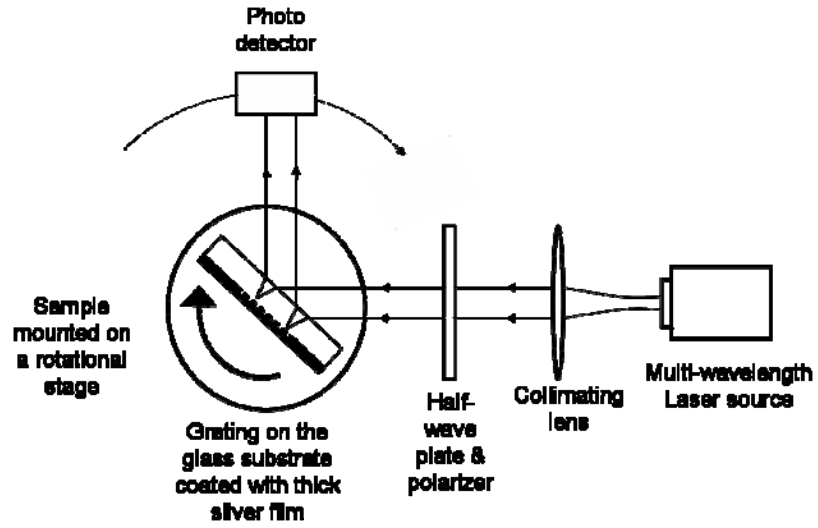

Figure3.10 Experimental setup to launch surface plasmons by characterize the grating coupler

Apart from the light reflected from the zeroth order diffraction/reflection, power emerging out into the first (and higher orders) of diffraction is also recorded. The reflected power is plotted against the angle of incidence in Figure3.10

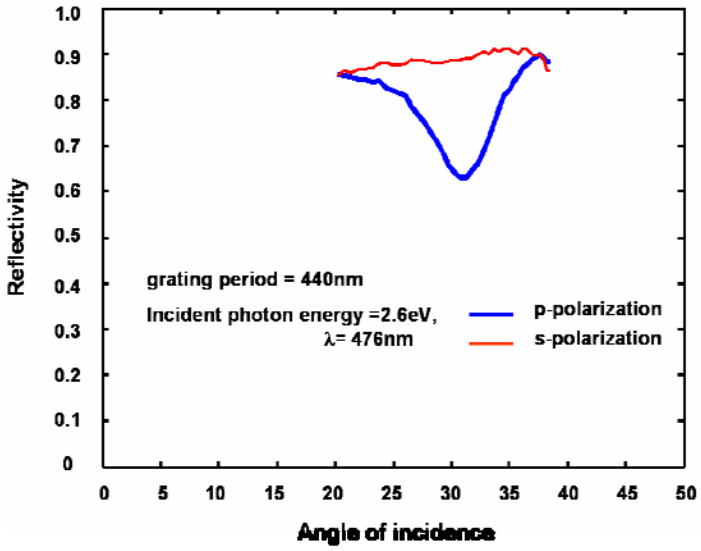

Figure3.11 A plot of zeroth order reflectivity vs angle of incidence

It can be seen that a dip in reflectivity is seen with the incident light being p-polarized instead of s-polarization. This indicates that the power is getting coupled into single sided surface plasmons at the silver-glass interface. Further, the efficiency of coupling is ~30%.

Chapter 4 Fabrication

4.1 Challenges

From a fabrication perspective, the key objectives for realizing the plasmonic dimple lens (Fig 2.2) are –

- To be able to fabricate the optimized angle of the taper for best energy throughput through the lens
- To be able to get a 3-D dimple shape of the tapered dielectric on nanoscale
- To get the a good quality interfaces between silver and dielectric
- To be able to achieve as thin a dielectric layer as possible because this limits the final achievable spot size.

The design specifications of the proposed plasmonic lens structure push the limits of conventional microfabrication methods widely used in the IC/MEMS processing. Further the materials required are not semiconductors like silicon, germanium, or III-V compounds where the process technology is well established. The primary concerns in realizing the above objectives are the following –

- Soft metals like silver, gold should be worked with. And these metals are not being used as for low frequency electrical contacts but are employed as waveguides for guiding optical frequencies at the nanoscale. This imposes

stringent specification on the surface quality of the interfaces of dielectric and metal.

- Amorphous dielectric films measuring <10nm thick, may have to be deposited on a soft metal like silver. The adhesion of metal to dielectric or vice versa is not good.
- A three-dimensional wedge like pattern with a terminal thickness of <10nm should be fabricated. This poses a twin challenge –

  (i) Obtaining a circularly symmetric 3D wedge shape in the dielectric, by means of pattern transfer either through etching or deposition of a gray scale pattern -- alternately deposition could be done into a mold with complementary dimple shape. Again, the adhesion of the deposited dielectric to the mold determines the final shape of the wedge near the focusing end of the taper.

  (ii) Leaving behind the terminal thickness of <10nm – integration of this step with the formation of dimple shape is another major issue whose success forms the crux of the fabrication process.
- After a method to fabricate a circularly symmetric is accomplished, then a technique needs to be developed to cut this circular dimple into half, so as to expose a smooth out-coupling facet at which the focused near field energy can be accessed.

This chapter discusses the efforts to address each of the above challenges and in the next chapter we discuss the fabrication process flow.

4.2 Evaporation of silver on dielectric surface

As mentioned in Section2.2, the metal chosen for the building up the plasmonic lens is silver because is has the higher material Q in the visible region between 420-620nm.

Silver is usually deposited by methods of physical vapor deposition like e-beam evaporation or ion sputtering. During the ebeam evaporation, an electron beam (of energy ~9keV) is used to heat up the silver source in a high vacuum environment of 10^{-6}-10^{-8} torr. At low pressures, the boiling point of silver is lowered. The silver atoms suffer little scattering (or have larger mean free path) in the vacuum chamber due to the low pressure. Hence the deposition of silver is thus directional.

Ion sputter deposition is done, when high energy argon ions bombard the silver source held at a negative potential, knocking off the silver atoms which get deposited on the substrate sample. Sputtering usually occurs at higher pressure owing to the presence of sputtering ions. Also this results in the non-directional deposition of silver on the substrate, which results in good step coverage of the features on the substrate.

We evaporate silver by heating the silver source with the electron beam. Depending on the power used for the process and the deposition time, the temperature of the substrate can rise to about ~80°C. Further the silver adatoms depositing on the

substrate are known to have high surface mobility. As the adatoms reach the surface, they tend to move around, lose energy and coalesce with the more adatoms to form grains. So the morphology of the film depends on the grain size of the polycrystalline silver and other conditions of evaporation like power and rate of deposition.

To determine the surface morphology of silver as a function of deposition rate, the films of 50nm thickness were deposited on cleaned glass substrates. Figure4.1 shows the root mean square (rms) roughness of the silver film reduces by increasing the deposition rate. Qualitatively, this could imply that faster the deposition rate, the adatoms coalesce more and grain sizes are bigger, thereby improving the surface roughness. However for the investigated range of deposition rates, the best rms surface roughness was about 2.8nm.

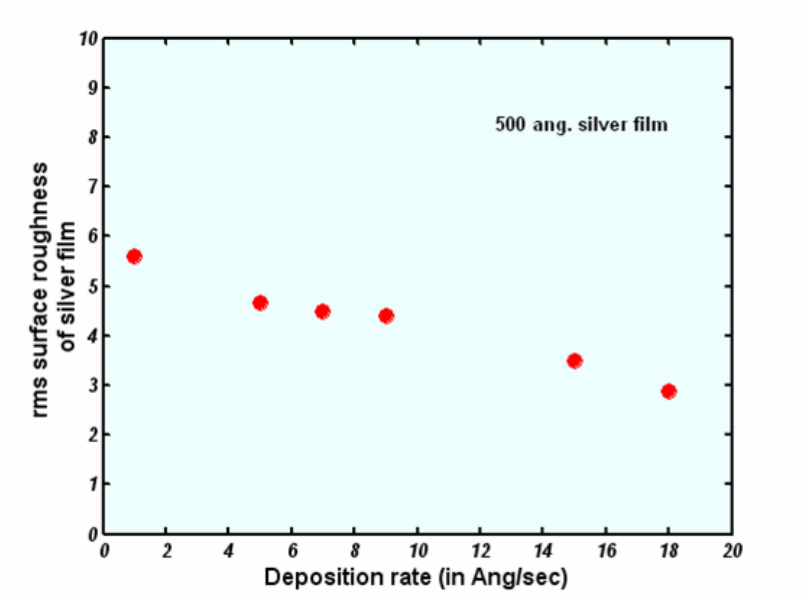

Figure4.1 The rms surface roughness of 50nm ebeam evaporated silver films on glass substrate vs the deposition rate of silver.

Higher deposition rates sometimes have the problem of "spitting" which can be defined as uncontrolled ejection of molten globules of silver onto the film. This gives an undesirable texture to the film when viewed under an optical microscope.

The top surface of a silver film tends to have rms surface roughness of ~3nm [35, 36]. However the bottom surface of the film that is against the substrate has the surface roughness of the substrate. Thus, evaporating silver against an already smooth surface, like that of a thin dielectric, is a possible solution where the active interface for plasmon propagation can have <1nm rms roughness.

Another important aspect of working with silver is that its adhesion to dielectrics is good. Hence care must be taken even while blow drying a sample in a jet of nitrogen. Sonication of samples could also lead to de-adhesion of silver on dielectric substrates.

4.3 Polymer-nitride approach for taper

As outlined in Section 4.1, making a three dimensional semi-circular dimple in dielectric with the thinnest section being <10 nm is a challenge that needs to be addressed. The strategy adopted to accomplish this is to use a two-step approach that involves breaking up the dielectric region of the plasmonic dimple lens into layers of two different dielectric materials.

As depicted in Figure4.2 the taper shape is obtained in a polymer where as the critical thickness of the dielectric, that determines the spatial extent of focusing of energy, is determined by the thickness of amorphous silicon oxide or nitride layer. The merits of this approach are as follows.

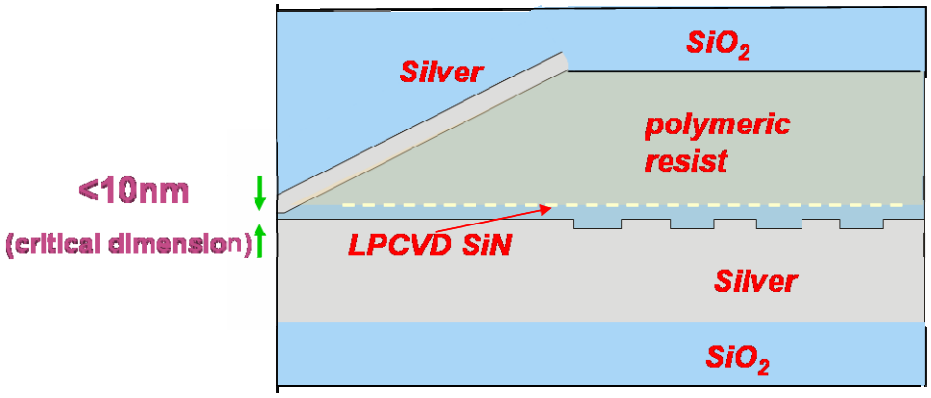

Figure4.2 Our approach to make a 3D structure in dielectric by using a thin amorphous dielectric layer along with a polymer resist.

- Thin and dense amorphous films like silicon oxide or silicon nitride are routinely obtained on a silicon substrate [37, 38]. These films are continuous and free of pinholes making them ideal to withstand high electric fields.
- Very selective etches exist to separate the thin nitride or oxide films from silicon substrates because of the mature and established processing techniques in IC/MEMS industries.
- It is easier to get smooth and continuous analog profiles in polymers than in amorphous dielectric layers. Three-dimensional shapes can be created in polymers

that are sensitive to light or electrons [39-43]. Some of these polymers are also robust enough to form good structural layers in the devices

- Typical refractive index of polymers is between 1.4-1.7. The refractive index of silicon dioxide is about 1.46 and that of silicon nitride is 1.8-2. With nearly equal refractive indices, this two-layer stack will act as a single integral piece of dielectric.

It is important to note that it is almost mandatory to use two different layers of dielectric layers for achieving the objective of this section of making the 3-D taper or dimple shape using a subtractive process, like in an etch process where the material is removed after being deposited or grown. The second layer of thin film dielectric material is going to be different from the tapered dielectric material and the subtractive process involved is chosen such that it shows a good selectivity between the two dielectric layers. In this aforementioned scheme we are using a polymer as the first dielectric layer which gets into a circular dimple shape by a subtractive solvent development process. Clearly this solvent development process does not attack the thin oxide or nitride films that form the thin second dielectric layer. Section 6.3 discusses a process sequence where a subtractive etch process is used to carve a dimple shape in oxide that forms the first dielectric layer. In this case, the second thin film layer is chosen to be nitride that is different from the first oxide layer.

In case of an additive process where the 3D taper or dimple shape is obtained by deposition of a dielectric layer, the thin-film dielectric layer could be of the same material as the dimple/taper layer. Focused ion/electron beam machines are usually equipped with Gas Injection Systems (GIS) where certain precursor gases can be injected in to the chamber only to be reduced by the focused ion/electron beam [44]. A commonly used precursor gas for depositing silica is TEOS (tetraorthoethylsilicate) . Section 6.4 discuses the fabrication of a 3D tapered structure using this approach.

4.4 Three dimensional dimple shape in PMMA

PolyMethylMethaAcrylate (PMMA) is a positive tone electron beam resist which is sensitive to high energy electrons. This resist has a molecular weight of about 495K or 950K dalton which indicates that it is a high molecular weight polymer. This polymer is soluble in solvents like cholorobenzene or anisole. A thin layer of 70nm of this polymer can be spun on flat substrate using the formulation 950K A2 [45]. In the regions of the substrate exposed to high energy electrons, the high molecular weight polymer undergoes scission and breaks into smaller units of polymer. A solution of Methyl IsoButyl Ketone (MIBK) and IsoPropyl Alcohol (IPA), mixed in the ratio of 1:3, acts as a developer dissolving the smaller units of scissioned polymer faster than the unexposed region polymer. Thus after development, the resist in the exposed areas is dissolved away while the unexposed polymer remains behind.

The electron beam used in the exposure, is accelerated through a potential of 70kV and is focused onto the substrate. The spot size of the focused electron beam is on the order of ~5nm. When a pattern needs to be exposed, the ebeam writer digitizes the pattern shape into a number of pixels. The beam dwells on each pixel for a certain period of time delivering a certain amount of charge at each pixel. This charge needs to be greater than the threshold dose of the PMMA (which is about 500μC/cm^2) to obtain a high contrast pattern after development.

When high energetic electrons are incident on PMMA, they not only pass through the resist layer but also penetrate a few microns into the substrate and get backscattered from the various depths of the substrate. A small fraction of these primary electrons are absorbed by the PMMA. In process of back scattering, a significant amount of energetic secondary electrons are emitted which broaden the region of exposure of the beam. This is called proximity effect where the scission of the PMMA not only occurs in the region of beam width of ~5nm but in an area but bigger than the 5nm incident beam spot size. We use the method of doing a single exel exposure. After development we obtain to obtain a crater in the resist. The surface of the developed resist is also rough as seen in Figure4.3 The roughness of the resist after development is most likely because of the solute-solvent phase separation [46, 47].

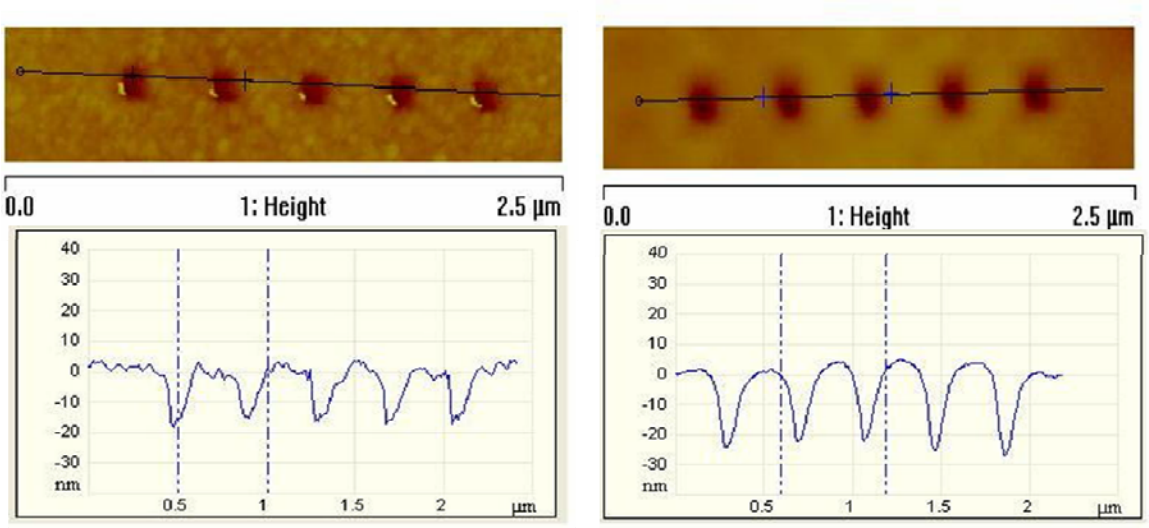

(a) (b)

Figure4.3 AFM scan of the dimples (a) after development (c) after SEM exposure

After development, the samples are exposed to high current of electrons in a Scanning Electron Microscope (SEM) chamber (typically a magnification of 7kX at 10kV, 10µA in a scan speed mode of "Slow2", for 10min on Hitachi S4700). It is observed that surface of the PMMA becomes smooth after SEM exposure as seen in Figure 4.3 It is also observed that the thickness of the PMMA reduces indicating some resist erosion after exposure after SEM exposure.

One possible explanation for the smoothing out profile could be the secondary electron induced decay of the carbon sites in the polymer converting the upper layers into volatile byproducts. This mechanism would require some amount of water vapor to be adsorbed in the polymer [48]. Another possible explanation for the loss of thickness of the PMMA after SEM exposure could be the scission of PMMA under large electron

current on the entire sample. The density of the smaller fragments of polymer chains could be less than the density of the unexposed polymer, leading to a post exposure reduction in resist thickness. Certain data (not presented here) seems to indicate that the reduction of thickness is higher at 5kV than at 10 kV in the SEM for the same time of exposure. This supports the former explanation of the involvement of secondary electrons which are higher at lower accelerating voltage.

Finally, once circular dimple obtained in PMMA by single spot exposure and subsequent SEM exposure is shown in Figure4.4. This dimple has a reasonable surface smoothness with the right dimensions and angle of the taper required for plasmonic lens.

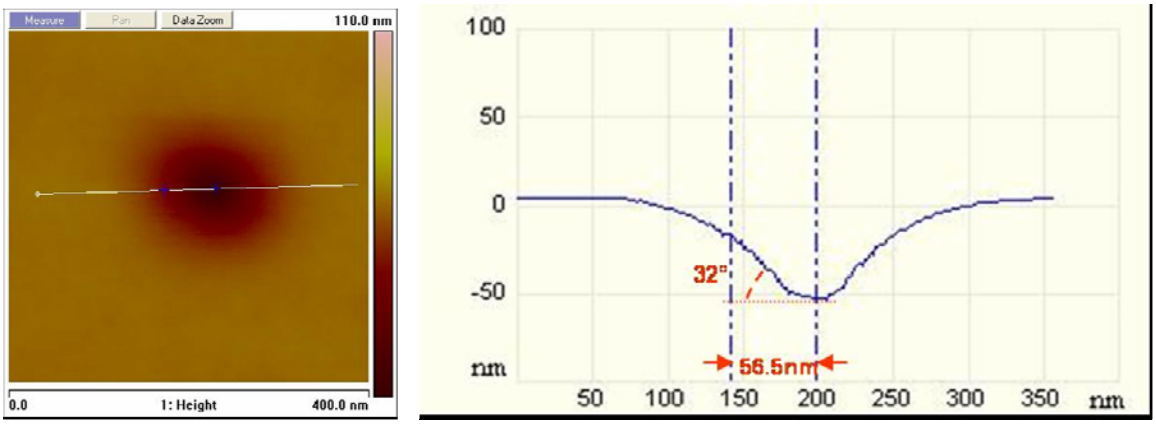

Figure4.4 AFM scan of a dimple made with single spot exposure

It should be noted that the dimple may not always be circular in shape. The stigmation of the electron beam would most likely give more elliptical dimples (see Figure4.5). Also the dose of exposure and time for SEM exposure need to be characterized every time a new source of PMMA resist is used.

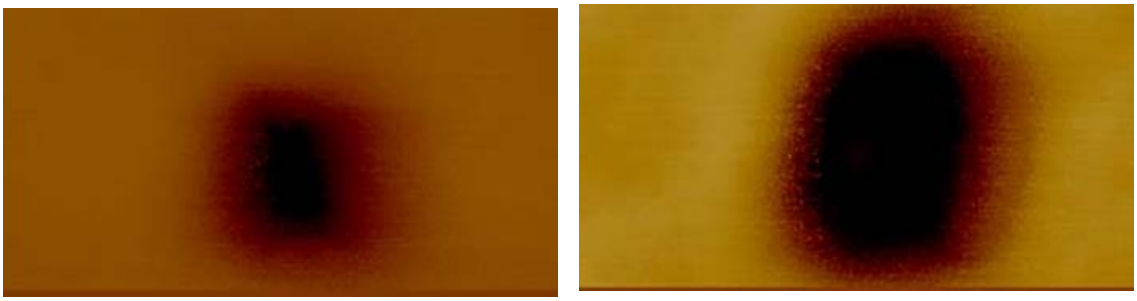

Figure4.5 Topographic scan of non-circular shaped dimples due electron beam astigmation. The size of the scan is 200nm x 400nm

4.5 Thin nitride films

As discussed in Section 4.3, the second part of the approach towards making the plasmonic taper, is the getting a good quality thin amorphous dielectric film. Also was mentioned that the IC industry routinely uses ultra thin high quality oxide [5] and nitride [26] films as gate dielectrics in transistors. However these films are grown on silicon substrates. For our application we need to sandwich this thin dielectric between two silver layers. The discussion in this section addresses the issues involved in removing the silicon substrate while retaining the thin film.

The methods employed in depositing nitride films in our nanofabrication facility are chemical vapor deposition (CVD) techniques namely Low Pressure CVD (LPCVD) and Plasma Enhanced CVD (PECVD). The LPCVD process takes place at higher

temperature (~750°C-850°C) when compared to PECVD process that takes place at ~300°C. In the LPCVD process, the rate of formation of a nitride film on a silicon substrate depends on the temperature of deposition. The LPCVD nitride films are denser than the PECVD ones because they have lesser content of hydrogen in them, there making them more resistant to hydrofluoric acid and other wet chemical etches. This means that LPCVD nitride films are superior in quality over the PECVD ones.

The gases used in the LPCVD process are dichlorosilane ($SiCl_2H_2$) and ammonia (NH_3) with the gas flow rates of 80sccm and 120sccm respectively. The process temperature is 800°C and pressure is ~300mTorr. The typical deposition rate of this stoichiometric nitride is ~5nm/min. However for a time of deposition for 1min, we get ~10nm of nitride. The thickness of this nitride has been characterized by both AFM step scan as well as ellipsometry. Prior to deposition, the silicon wafers are cleaned in piranha solution (H_2SO_4+H_2O_2) for about 10min followed by a quick BOE (buffered oxide etch consisting of HF+NH_4F) dip before they are loaded into the LPCVD furnace tube.

The thickness of the nitride films can be reduced by reducing the process temperature and process time. There is a about ~1min gas stabilization time during which, some deposition occurs. The important point here is the quality of the thin nitride films which should be continuous and free from surface defects or pin holes. Another notable point is that the nitride film tends to be conformal at low pressures of about ~100mTorr where mean free path of the gaseous species is larger than the step size.

Removing the silicon substrate

Nitride films are so strong and robust that they have many applications as free standing membranes. As discussed in the beginning of this section, we need to remove the underlying silicon substrate.

One of the methods to selectively etch silicon with a very high degree of selectivity towards nitride is potassium hydroxide solution. The KOH etch is an established method in silicon bulk micromachining which results in an anisotropic etch of <100> or <110> planes over <111> planes. This anisotropic etch rate of the crystal planes is attributed to different density of silicon atoms on different planes. A square window opened up in <100 > surface when etched in KOH turns into a pyramid exposing the <111> crystal planes. The angle between these planes is 54.7° as depicted in Figure4.6. A 30% aqueous KOH solution at 80°C would have an etch rate of ~1.1μm/sec [49].

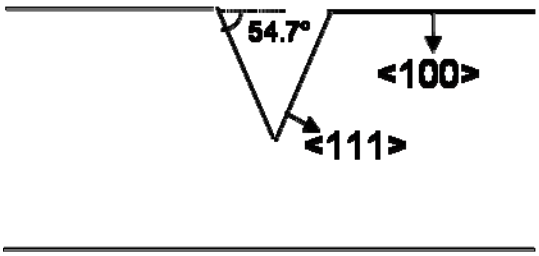

Figure4.6 Crystal planes of silicon during KOH etch

Silicon nitride is a good etch mask for KOH etch. About 100nm of nitride is adequate for about 6-7 hours of etch in KOH solution. Another protective layer is called ProTEK B (made by Brewer Science) also helps to protect silicon surface from KOH. It typically requires a primer for good adhesion to the substrate. In my experiements, the etch rate of silicon in the KOH solution is dependent on the area of exposed silicon for large exposed areas (>1sq.cm). Hence the KOH solution needs to be refreshed often if the entire silicon substrate is to be removed.

Another method of removing silicon is by using a mixture of hydrofluoric acid (HF), nitric acid (HNO_3) and acetic acid (CH_3COOH). This acidic mixture etches away silicon at a very fast rate >300μm/min. The HNO_3 is a strong oxidizer which oxidizes silicon and HF attacks the oxide. For a low HNO_3 and high HF combination, the etch rate is limited by the oxide formation where as for high HNO_3 to low HF combination, the etch rate is limited by oxide removal. The amount of acetic acid present in the mixture determines the rate of dissociation of the HNO_3.

Samples of size of 1cmx1cm coated with <10nm of LPCVD nitride are bonded to a piece of glass with a special kind of epoxy called *Optocast*. This epoxy is filled with silica particles to reduce the volumetric content of epoxy. Curing of epoxy causes shrinkage and thereby stress on the pieces that is bonded to glass. The filler silica particles tend to reduce the stress exerted by the *Optocast* after curing. The *Optocast* is cured for about 2 hrs at 110°C. The stress is an important factor, because when the silicon

substrate is removed with HNA, the thin layer of nitride film is supposed to remain behind on *Optocast* that is glues to the glass. Samples with a thin film of nitride after the removal of silicon substrate in HNA are shown in Figure4.7.

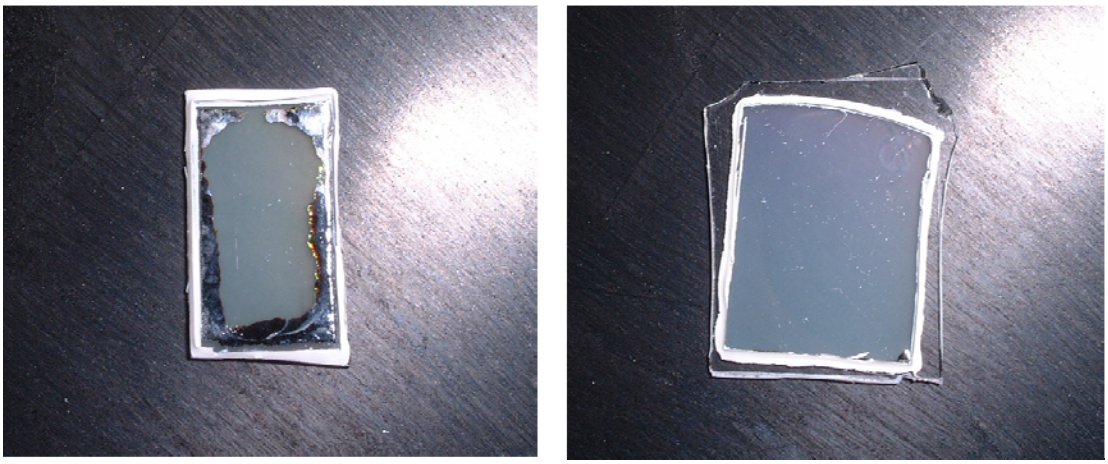

(a) **(b)**

Figure4.7 Removal of silicon substrate with HNA (a) some silicon is still on the rim of the sample (b) all silicon is removed.

4.6 Cutting through the dimple

In Section 4.4, a circular dimple was created in a polymeric resist. As described in Section 2.4, the three dimensional focusing of the energy is achieved at the center of the semicircular dimple (Figure2.8). Hence the circular dimple needs to be cut into half as shown in Figure4.8

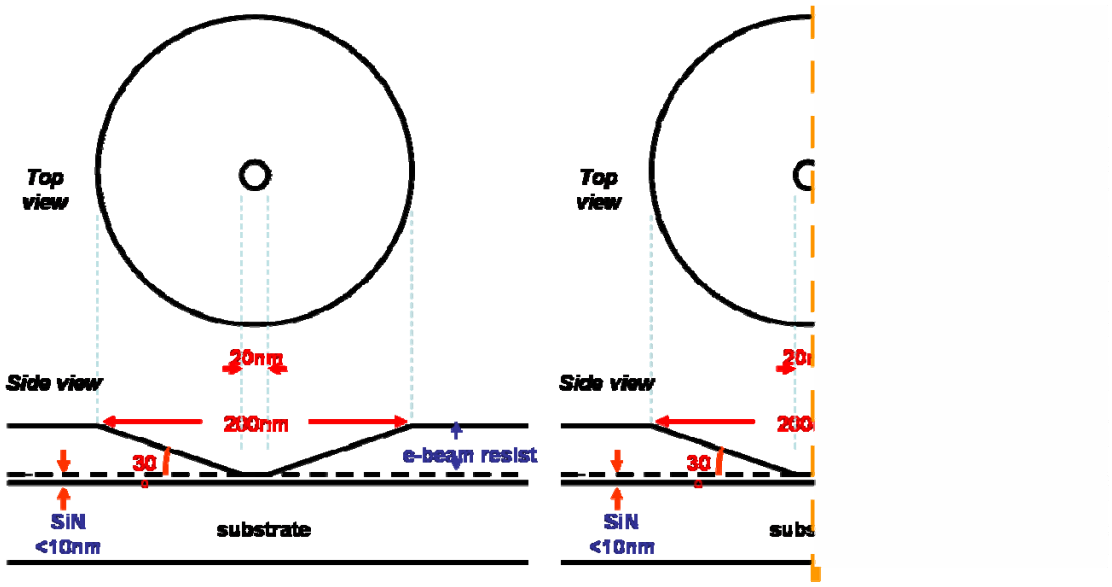

(a) (b)

Figure4.8 Cutting through the dimple (a) before polishing (b) after polishing

One way to achieve this "cutting at nanoscale" is by polishing the structure from one end till the half of the circular dimple is polished away as shown in Figure4.8. Chemical Mechanical Polishing (CMP) is a standard process in the IC industry for planarization of the wafers. It is also used in the copper damascene process to form an embedded layer of interconnects. Though CMP is a standard process for copper, there are also reports of polishing a softer metal like silver [50].

Mechanically polishing away the edge of a sample of different layers can be quite challenging. The idea is to polish a stack of dissimilar materials like glass, silver, PMMA, nitride and epoxy, all at the same time. These materials differ from each other in terms of hardness. Silver is a soft metal where as nitride and glass are the harder ones.

The edge-polishing machine (Figure4.9) has a base platen with a diamond polishing film on it. The sample to be polished is held by a holder that clamps it on its surface. The sample holder is mounted on the polishing arm such that the sample can be polished on this side-face (or edge face) by the diamond pad on the base platen. The base platen rotates at a speed of ~100rpm while the polishing arm moves radially over the base platen. Throughout the polishing process, there should be a constant flow of water to prevent build-up of the polished residue on the pad.

Figure4.9 Ultrapol edge polishing machine

A sample is polished with diamond films of successively finer grit-sizes. To begin with, a lot of material is removed with a pad of coarse grit-size of about 9μm. Then a 3μm grit-size pad is used followed by the 0.1μm pad for the finest polishing. Between changing of the polishing films, the sample is sonicated to get rid of the particles that are stuck to the surface. After polishing, the sample is viewed under the SEM to examine the

-quality of the polished face. AFM scans are also done periodically to determine the smoothness and recess of the layers with respect to each other.

One of the major issues in polishing the stack of materials with varying hardness is the de-lamination of layers with respect to each other. This de-lamination between layers can be because of stress or because of inherently poor adhesion between the layers. Further the clamping force on the sample, the swelling of epoxy, the polishing pressure etc can also cause de-adhesion. Other major issues are the trapping of fine polishing grit in the crevices opened by de-lamination and re-deposition or filling of polished silver debris into the crevices (see Figure4.10). Polishing pressure, speed, sonication – all these parameters seem to be critical in the achieving a good quality surface.

Repeatability in achieving a good polished facet without de-lamination of any layers is one challenge. Another challenge is to use some fiduciary markers to determine the precise endpoint for polishing such that circular dimple could be cut into half. The fiduciary markers used polishing were an array of interdigitated triangles of different sizes made in metal of thickness ~150nm patterned using photolithography (see Figure 4.11). The centers of a pair of triangles of a given size are offset from those of another pair of a different size by about 20nm (which is the desired tolerance in polishing endpoint). As the material is being polished away, the largest set of triangles becomes visible when the sample is dismounted from the polishing machine and viewed under a microscope (of ~20X-50X magnification). As more material is polished away, the

smaller sets of triangles become visible. Thus it could be known how far the polishing front away from the dimple-die. As one approaches closer to the dimple die, it becomes mandatory to inspect the polishing facet using an SEM and AFM machines to know the exact advancement of the polishing front.

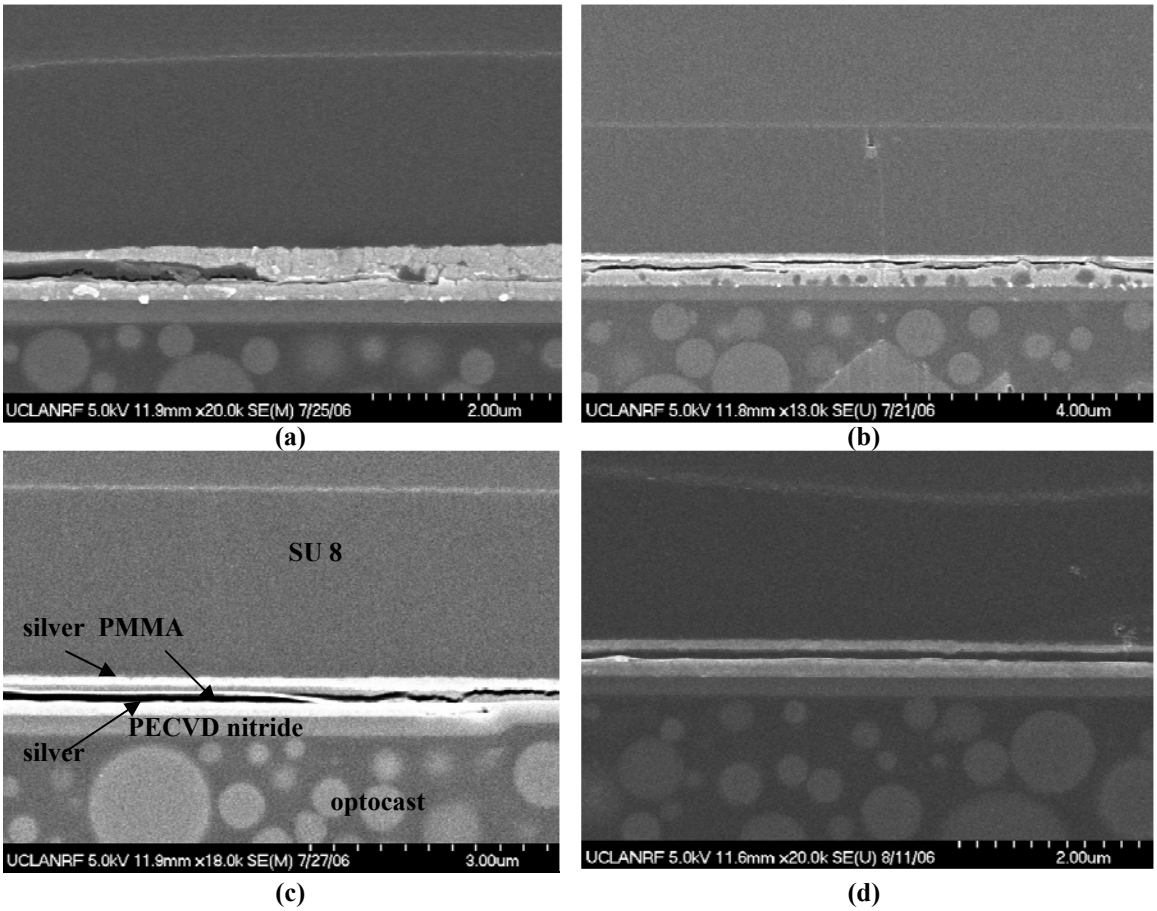

Figure4.10 Edge mechanical polishing (a) Re-deposited silver residue on the silver (b) De-lamination between layers and grit particles on lower silver layer (c) PMMA/thin nitride layer curving up between two of silver exposing de-lamination (d) A good polished facet with no de-lamination

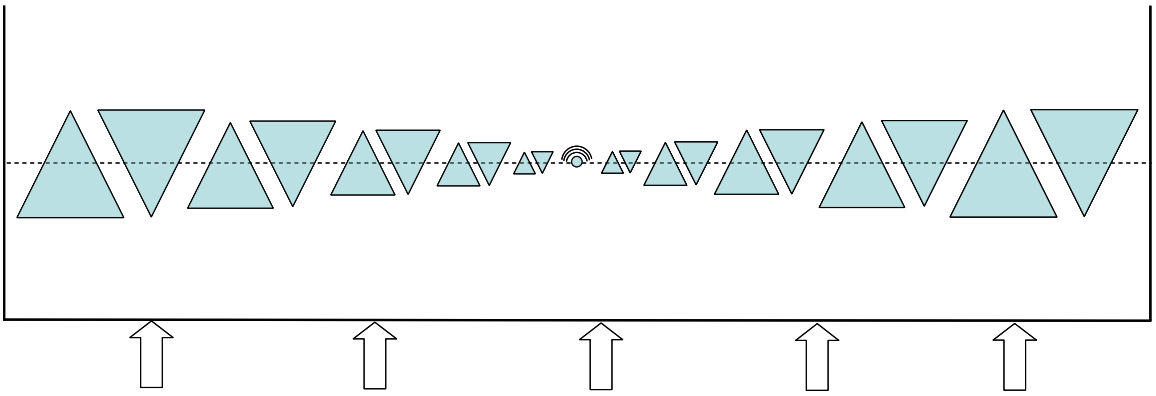

Figure 4.11 Two arrays of interdigitated triangles that serve as fiduciary markers for edge polishing. The circular dimple is at the center of the two arrays. The offset (~ 20nm) between pairs of triangles of different sizes is not depicted. The arrows indicate the polishing front of the sample while mechanical edge-polishing. Also note that the figure is not to scale.

Another approach to "cutting through the dimple" is by the use of focused ion beam milling. An ion beam of gallium ions can be focused to a very small spot size. These ions when accelerated across 30kV can knock out material from the substrate. Milling with an ion beam incident at a grazing angle to the facet of interest, produces a reasonable smooth facet with rms roughness of 1.5nm as seen in Fig. 4.12.

However, there may be certain drawbacks to this approach. Even if the milling is done at a grazing angle of incidence to the facet of interest, there could be lateral penetration of ions into the facet, thus causing gallium contamination in the sample. Though it has not been quantitatively investigated as to how any gallium ion contamination may affect the optical properties of a Ag-dielectric-Ag stack, it would be

likely that any embedded gallium ions would serve as scattering centers for the surface plasmons and would cause additional energy loss.

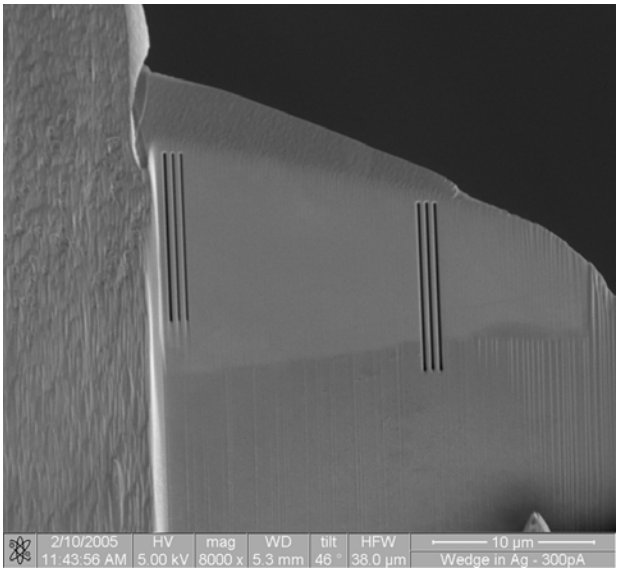

Figure4.12 A sidewall on a single crystal piece of silver, milled with a focused ion beam at grazing incidence to the surface of the sidewall.

Chapter 5 Plasmonic Lens: Fabrication & Measurement

This chapter describes the top-down process-sequence that was used to fabricate the plasmonic dimple lens. This is followed by the near-field characterization of the dimple lens using a pulled-fiber probe in a commercial NSOM set-up.

5.1 Switching from silver to gold

Last chapter outlined the challenges in the fabrication of the proposed three-dimensional plasmonic lens structure. The strategy employed to address each challenge is discussed in a separate section of the chapter. Section 4.6 discussed the issue of removing half the circular dimple (Fig.4.7) to get an access to the focal-spot of the dimple lens. Two methods were suggested here, namely (i) mechanical polishing (ii) focused ion-beam milling.

Between the abovementioned methods, mechanical polishing became the process of choice because it was possible to get several plasmonic lenses in one go as against the FIB milling that requires a long time to remove a lot of time to remove material. Furthermore the IC/MEMS and hard-disk industries routinely polish their wafers at various steps.

The de-lamination problems involved in polishing a stack of dissimilar materials are already depicted in Fig 4.9. Optimal choice of polishing speed, polishing pressure,

and adoption of optimal procedure for curing, sonication etc, helped in overcoming the problem of de-lamination of structural layers of the plasmonic lens. When the polishing endpoint was reached with the help o f fiduciary markers, the topography of the polished facet was characterized with an AFM probe. Fig.5.1 depicts the topography of one such facet.

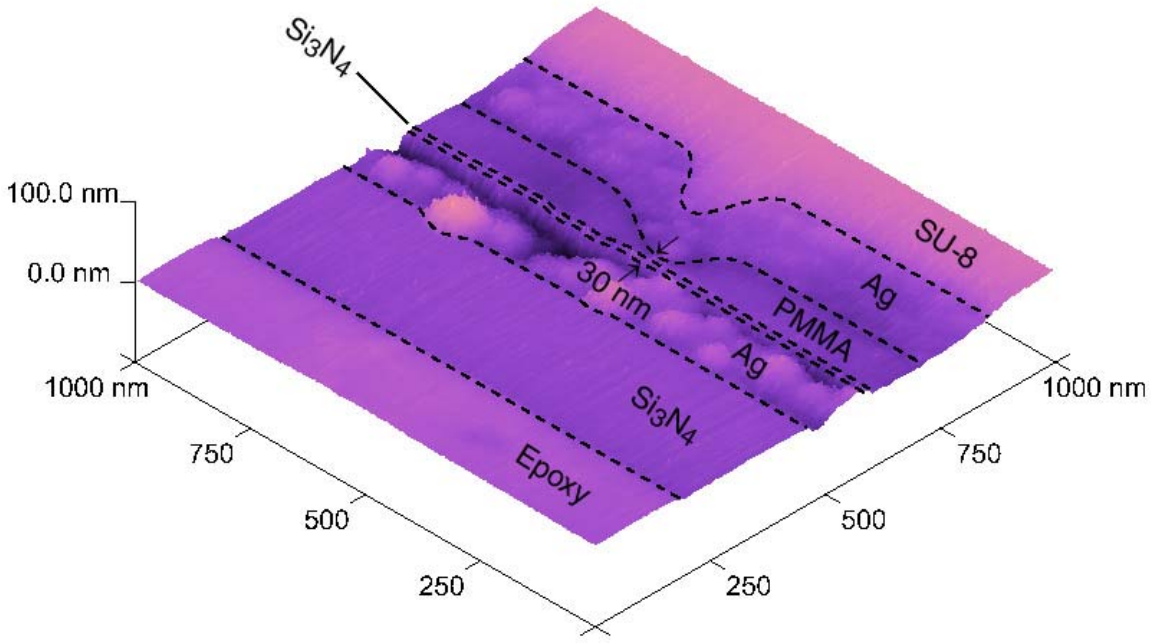

Figure 5.1 A perspective topographic image of the polished facet after mechanical polishing. The layers of the stack are outlined and labeled for a Ag-dielectric-Ag

It is evident from Fig.5.1 that good adhesion between the silver, nitride, polymer, and epoxy layers post-polishing. It is also easy to notice that at least one of the silver layers is very grainy and rough after polishing. This roughness would adversely affect the near-field experimental characterization explained in Section 5.3.

Silver has been our metal of choice since we discussed the principles of plasmonic dimple lens design. It was earlier noted that silver had the best material Q (Fig.2.3) and efforts were directed on characterizing dielectric constants (Sec.3.1) and surface roughness (Sec.4.2) of silver films. However the quality of the post-polished silver surface could not be improved even after tweaking several polishing parameters. A possible conjecture for this roughness is the corrosion of the silver layer. As mentioned in Sec.4.6, the polishing is done in the presence of a continuous stream of water to wash away the polished-residue from the polishing pad. This water could have corroded the silver layer causing the silver grains to stand out in a topographic AFM scan.

To find a solution, it was decided to replace the silver layer of the plasmonic lens with gold. A new sample was prepared and was mechanically polished. After optimizing the polishing parameters of the stack with gold as the metallic layer, a topographic AFM scan of the polished facet was obtained. Fig.5.2 shows a remarkable improvement in the surface quality of the polished-stack. All the layers appear smooth and appear to be uniformly polished. After such encouraging polishing results, it was decided to implement the plasmonic dimple lens in a gold-PMMA-nitride-gold stack. The operating wavelength was moved from 480nm (2.6eV) to 633nm (1.96eV) where gold has the best material Q (Fig.2.3). To find the dispersion relations of double-sided plasmons in Au-silica-Au stack, refer to Appendix B.

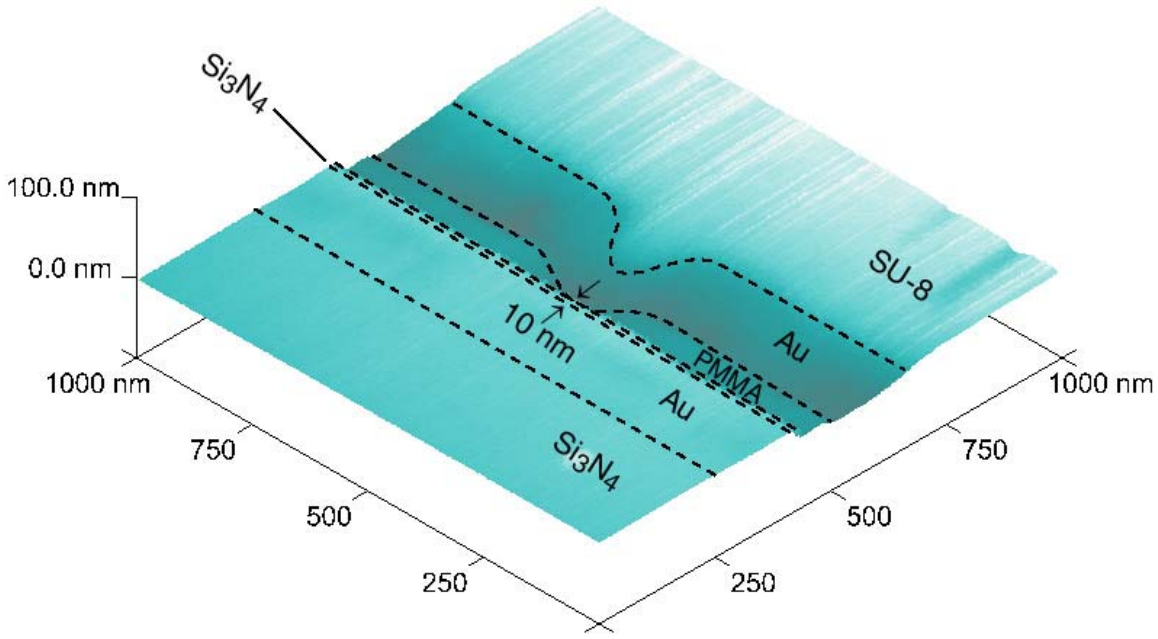

Figure 5.2 A perspective topographic image of the polished facet after mechanical polishing. The layers of the stack are outlined and labeled for a Au-dielectric-Au

5.2 Fabrication Process Flow

The exact process sequence as depicted in Fig.5.3 emerged from numerous trials involving different materials like metals, dielectrics, polymers, and epoxies, and different process steps like etch and polishing. Thin silicon nitride of ~10nm thickness, was deposited on a standard silicon wafer, using low-pressure chemical vapor deposition (LPCVD) process. Gold islands were then patterned on this smooth silicon nitride surface using photolithography, e-beam evaporation and liftoff process (Fig.5.3a). These islands constitute the lower Au layer in the Au-dielectric-Au stack of Fig.2.3. They also include

the fiduciary alignment markers for subsequent e-beam lithography steps, and the endpoint detection markers for the final edge-polishing step.

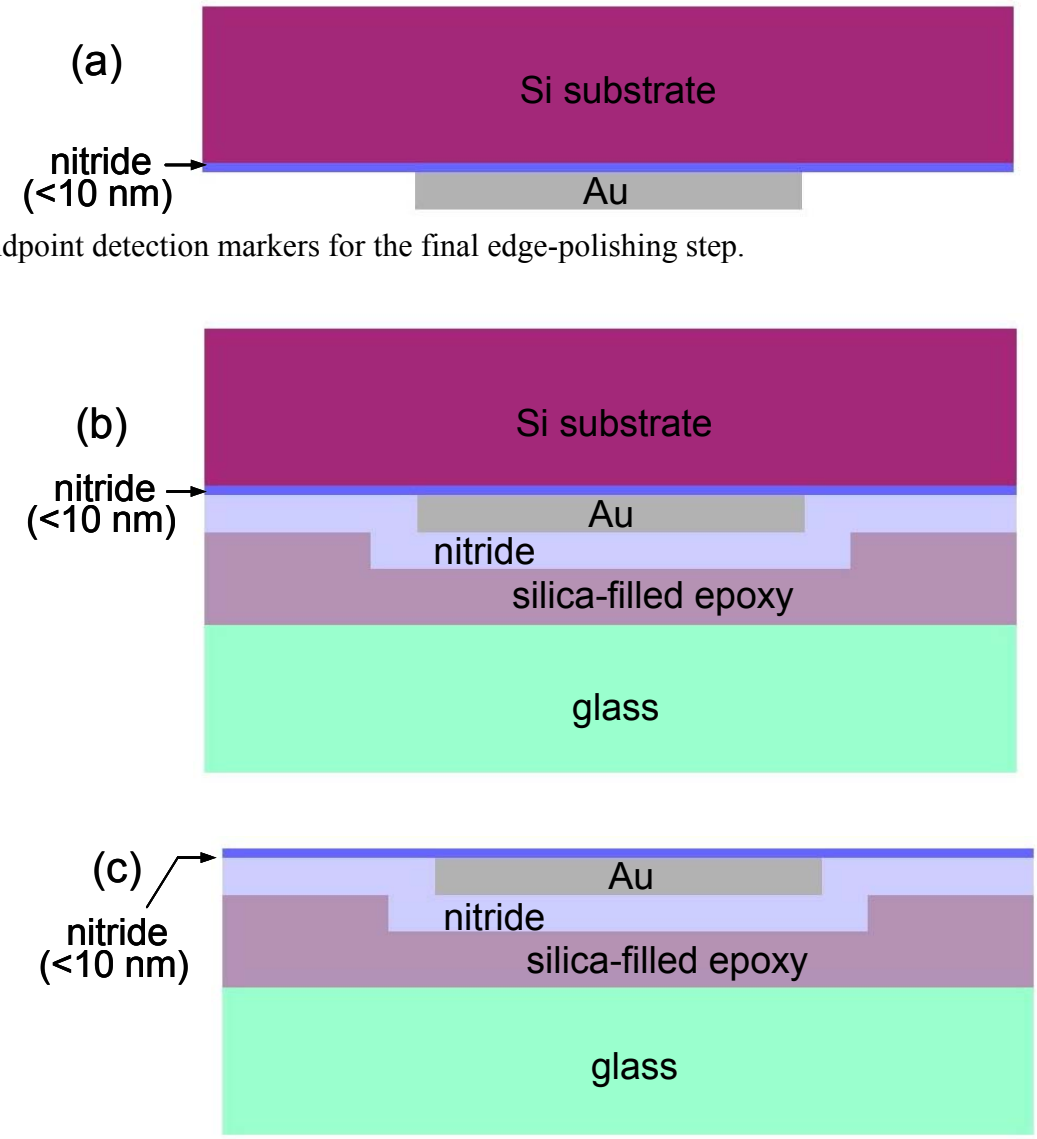

Figure 5.3 (a) Au islands patterned on 10nm LPCVD SiN on a Si-substrate. (b)These islands are coated with 300nm of PECVD SiN and bonded to a glass using silica-filled epoxy. (c) Si-substrate is completely etched away with HNO_3+HF after thinning it down with DRIE process.

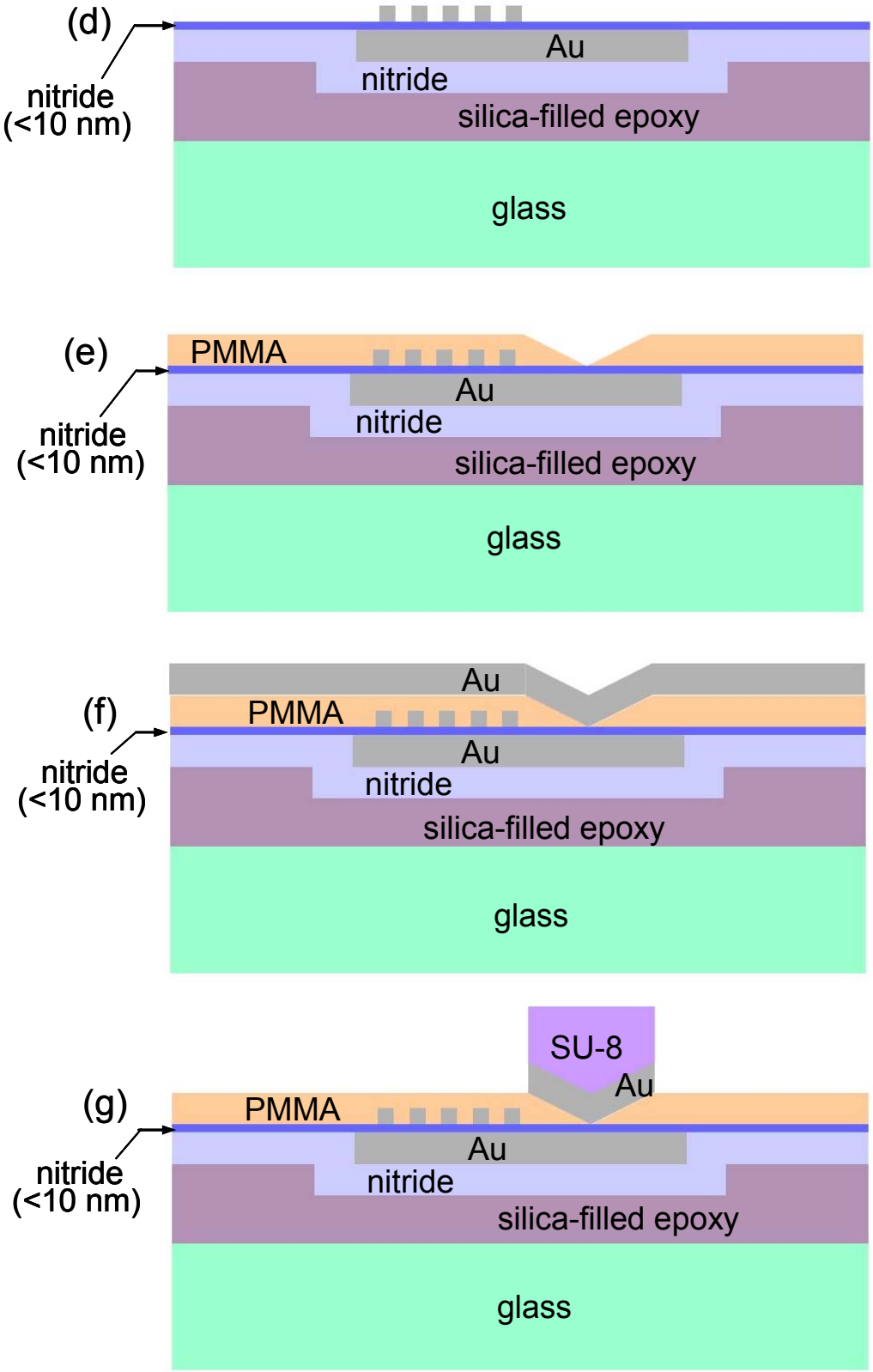
(d)
nitride
(<10 nm)
Au
nitride
silica-filled epoxy
glass
(e)
PMMA
nitride
(<10 nm)
Au
nitride
silica-filled epoxy
glass
(f)
Au
PMMA
nitride
(<10 nm)
Au
nitride
silica-filled epoxy
glass
(g)
SU-8
Au
PMMA
nitride
(<10 nm)
Au
nitride
silica-filled epoxy
glass

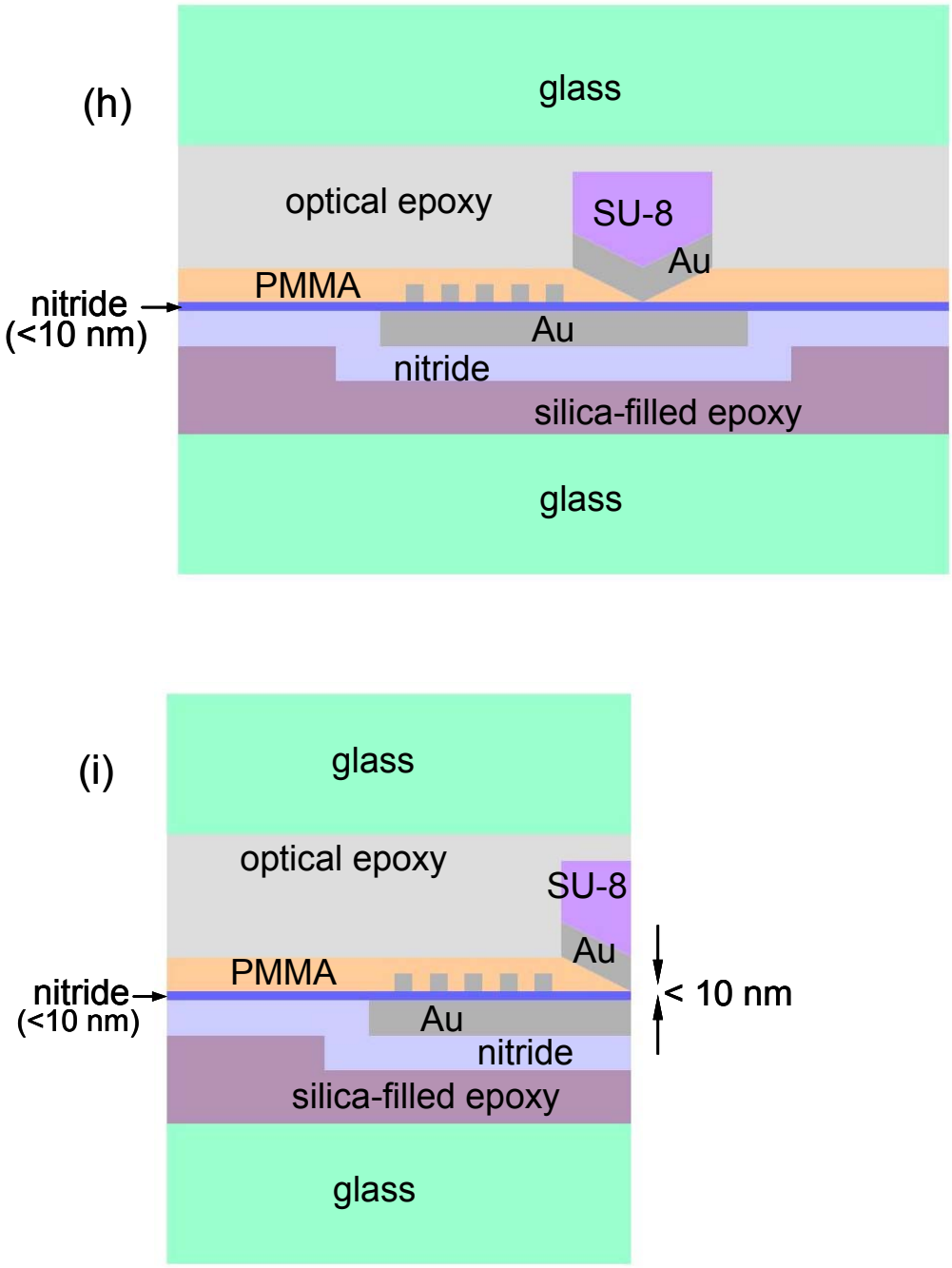

Figure 5.3 (d) Semi-circular grating coupler is fabricated using e-beam lithography, followed by Au metal e-beam evaporation, and resist lift-off. (e) The dimple profile in PMMA is patterned with e-beam lithography (f) Second layer of Au is deposited by e-beam evaporation. (g) With patterned

SU-8 resist as a mask, this Au layer over the grating coupler is etched away with Ar-sputter etch. (h) The sample is bonded to glass using optically transparent epoxy. (i) This stack is mechanically polished from one edge until the point when the circular dimple profile in PMMA is polished halfway through.

About 300nm of silicon nitride was deposited on top of these islands by plasma enhanced chemical vapor deposition (PECVD) process to reduce stress on the thin LPCVD silicon nitride during the subsequent bulk silicon removal step. The patterned side of the sample was bonded to a glass piece using low stress silica-filled epoxy for support during the silicon substrate removal. This stack is shown in Fig.5.3b. The silicon substrate was thinned down to less than 50μm using deep reactive ion etching (DRIE). The remaining silicon was removed by wet etching in a 1:1 mixture of HF and HNO_3 as depicted in Fig.5.3c. This mixture etches silicon but etches LPCVD silicon nitride over 10^3 times more slowly.

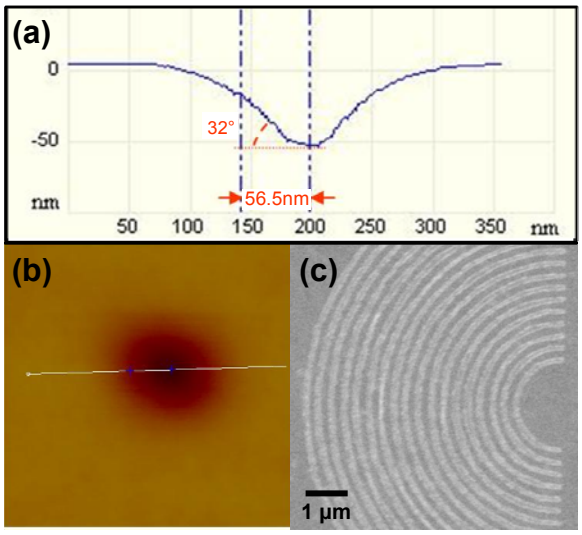

Figure 5.4 (a) Topographic cross sectional scan of dimple and (b) 2D top surface image acquired from the topographic AFM scan of the dimple profile in PMMA. The size of the scan is 400nm×400nm (c) SEM image of the circular grating coupler.

A semi-circular Au grating of 30nm height and 390nm period was patterned using e-beam lithography, e-beam evaporation, and a resist liftoff process (Fig.5.3d). A circular dimple profile was then formed in a 100nm layer of PMMA with a single spot exposure using e-beam lithography (Fig.5.3e). Both the grating and the dimple were inspected using a scanning electron microscope (SEM) and an atomic force microscope (AFM), respectively, as can be seen in Fig. 5.4. To form the top Au layer of Au-dielectric-Au stack as shown in Figure 2.3, 100nm layer of Au was evaporated on top of the PMMA layer using e-beam evaporation (Fig.5.3f). This Au layer was then etched to gain optical access to the grating using Ar-ion sputter etch with e-beam patterned SU-8 (a negative e-beam resist) as a mask. Fig.5.3g depicts the stack at this stage. The structure is then bonded to another piece of glass using optically transparent epoxy for additional support during the mechanical polishing step as seen in Fig. 5.3h. Finally, the sample is polished from the edge until the center of the dimple is exposed at the polished edge facet (Fig.5.3i). The topographic and phase-shift images from the AFM scan of the polished edge facet are shown in Figure 5.5.

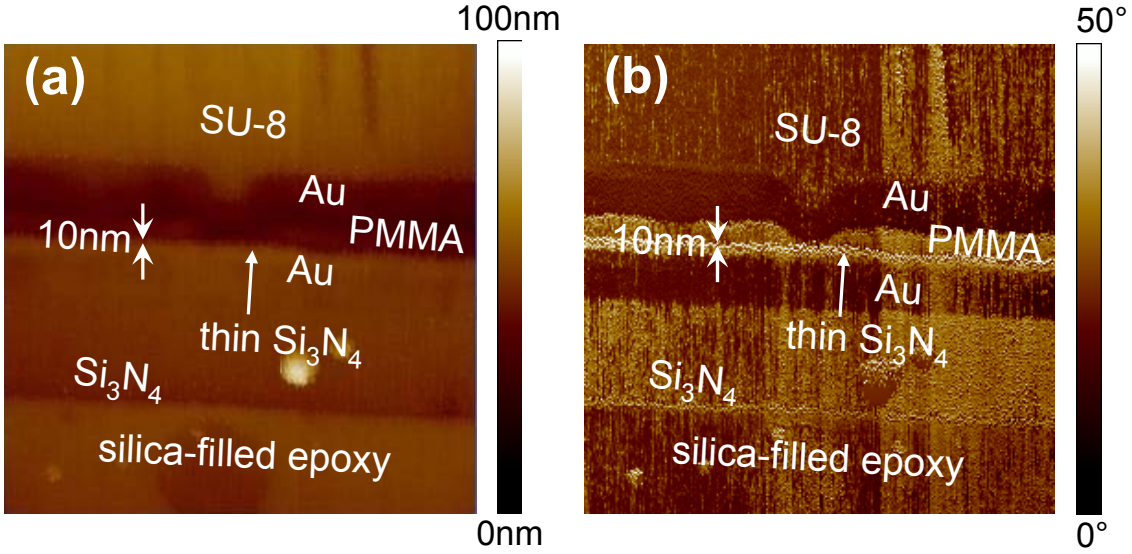

Figure 5.5 (a) Topographic and (b) out-of-phase- tapping mode response of the AFM image of the out-coupling edge after mechanical edge-polishing. The size of the scan is 1.5μm×1.5μm. A good smooth polish, with minimal polishing relief, makes distinguishing the different layers in the topographic image difficult. The out-of-phase-tapping mode response image helps distinguish the different layers in the image.

5.3 Near-field experimental set-up

An NSOM system is a Scanning Probe Microscopy (SPM) system that uses a metal-coated fiber probe to scan the scan the surface of a sample. Typically an optical fiber, say with a nominal diameter on the order of a wavelength of visible light, is pulled such that the core radius reduces to about 50-100nm. After this the fiber is coated with at least 100nm of a metal like aluminum. As discussed in Chapter 2, the typical propagating mode of the optical fiber is cut-off as it evanescently emerges out of the 50-100nm

aperture. Both AFM and NSOM systems are SPM systems; with the difference being that the AFM system uses a sharp pyramidal silicon or silicon nitride tip where as an NSOM system uses an optical fiber as a probe. Every SPM system requires a force-feedback mechanism that helps the probe to track the surface of the sample and thus helps to collect the topographic or any other signal that characterizes the surface. An additional difference between an AFM and a NSOM system is that an AFM tip taps surface of the sample to get the force-feedback where as the NSOM fiber probes uses the shear-force as the feedback. Thus during the scan operation, a NSOM fiber oscillates horizontally parallel to the surface in contrast to an AFM tip that oscillates vertically perpendicular to the surface.

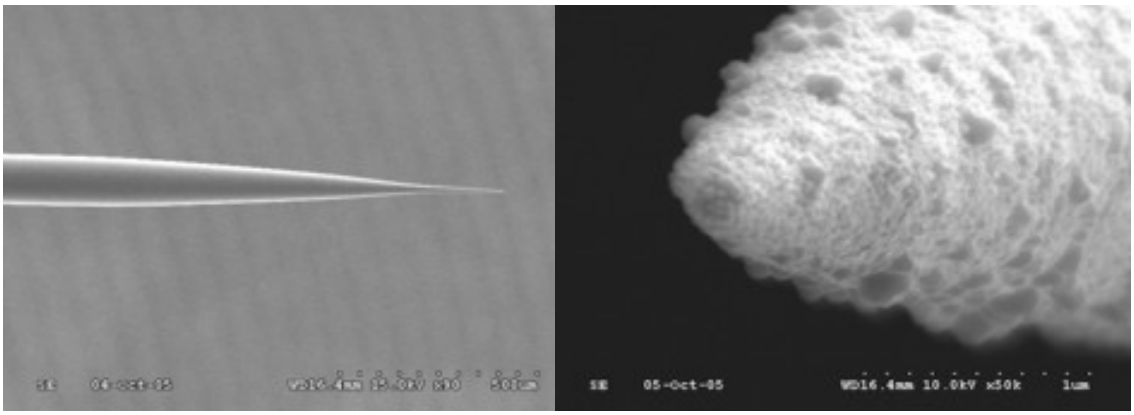

Figure 5.6 Typical SEM images of commercial pulled fiber probes used for NSOM applications

The plasmonic dimple lens is characterized with a commercial NSOM system made by Veeco Inc. called Aurora. The Aurora system consists of a scanning horse-shoe shaped scanner-head onto which the fiber-probe is mounted. This scanner-head consists of a z-stepper motor and a piezo-scanner that moved the mounted fiber in the vertical z

direction. The scanner-head sits on a base that surrounds the stage. The stage is connected to stepper-motors and piezo-scanners that move a sample mounted on the stage in the x and y directions. The Aurora system comes with two microscope objectives where one can be used to illuminate a sample from the top and another can be used for back-illumination of the sample. The output-end of the pulled-fiber probe that captures the optical signal is coupled to another optical fiber which is connected to a photo-multiplier-tube (PMT). The whole system is enclosed in a black polycarbonate box that helps to provide optical shielding. At the base of the base of the enclosure box, there are two holes should which external optical fibers can be brought into the box. In the normal mode of operation, a laser that forms the external light source is sits on a platform that is mechanically isolated from the platform on which the Aurora system is placed. Laser systems, particularly the air-cooled ones, create mechanical noise in operation. Therefore, light from the laser brought into the Aurora enclosure box via an optical fiber.

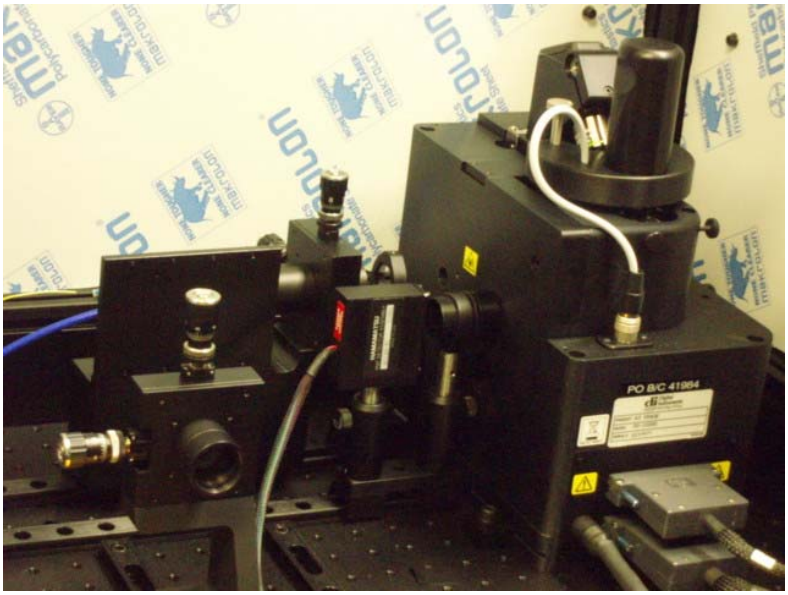

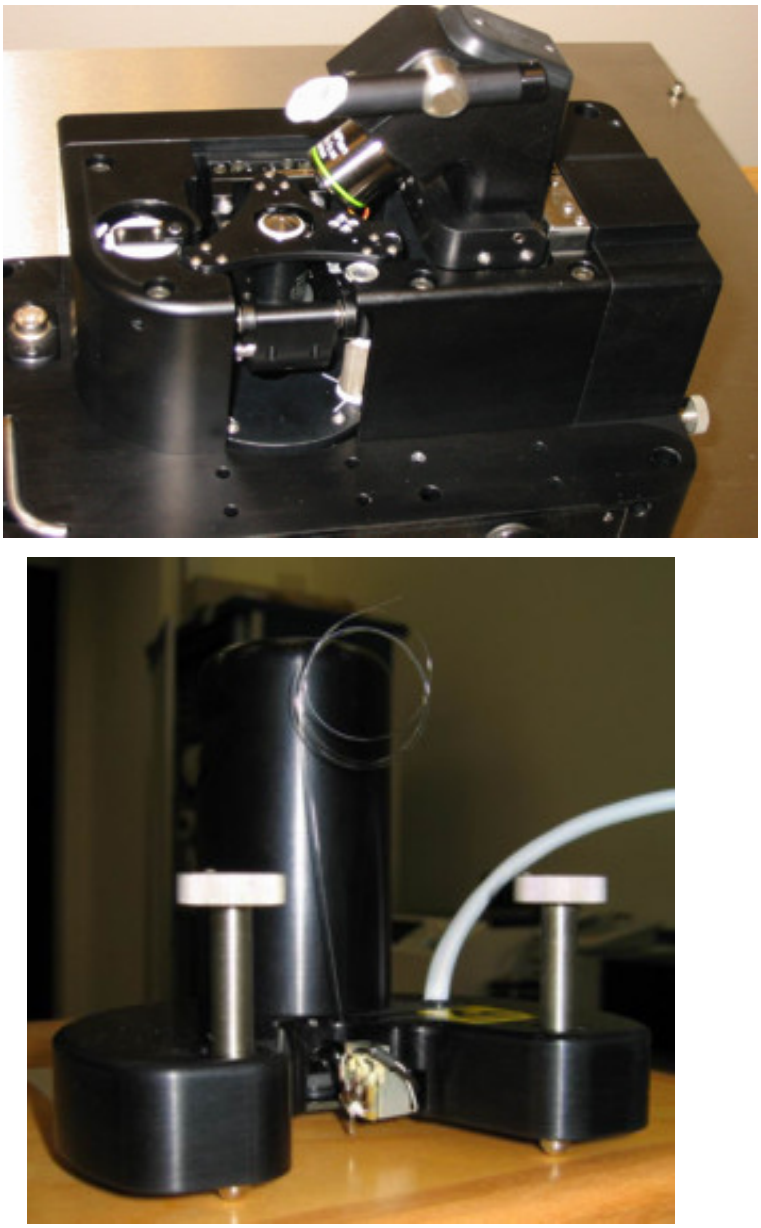

Figure 5.7 Inside an Aurora NSOM system. (Upper) Overview of the Aurora system, (Middle) Stage and reflective objective mounted on the tower, and (Lower) Aurora head with tuning-fork scanner along with a tuning-fork mounted metal-coated pulled-fiber probe.

The Aurora system needed to be modified for characterization of the plasmonic dimple lens. Figure 5.8 shows the schematic of a plasmonic lens characterization. A polished sample has several plasmonic-lens-dies. And these dies are located at the very top-edge of the sample. In order to locate each die and to focus the laser beam onto each grating in-coupler, the focusing microscope objective should be parallel to the stage. As seen from Fig.5.7, the reflection objective of the Aurora system provides illumination at an angle of 45°. Therefore the reflection objective fixture has to be removed from the Aurora system and a long WD Mitutoyo objective (50x, 0.45NA) was used. This microscope objective not only provides input laser illumination of 633nm wavelength but also is used as an imaging objective that forms on image on a CCD screen. The PMT that is used to record the NSOM signal is shielded from the input laser beam inside the Aurora enclosure box.

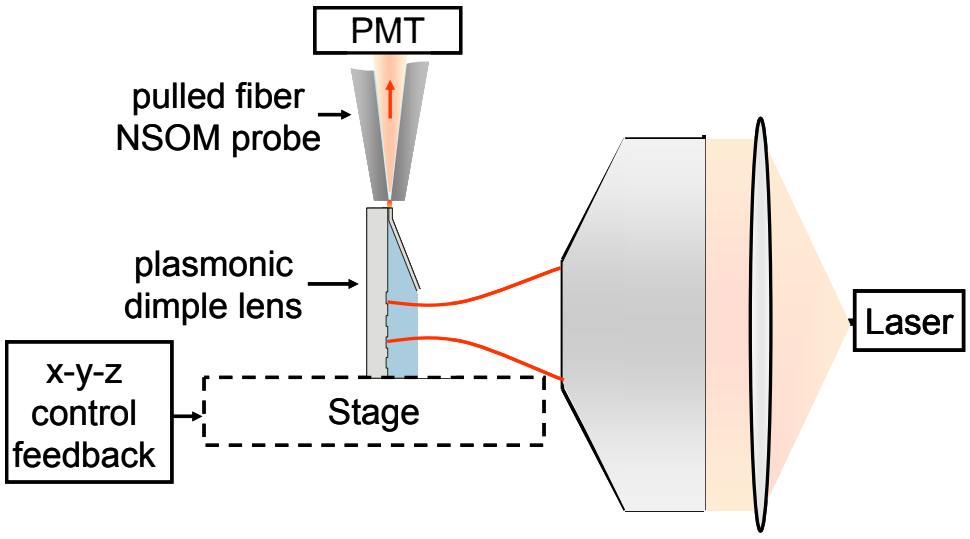

Figure 5.8 Schematic of the experimental setup to characterize the plasmonic dimple lens using Near-field Scanning Optical Microscopy (NSOM).

5.4 Data analysis & discussion

While scanning the surface of interest, an NSOM fiber probe simultaneously collects the topographic signal and the near-field optical signal. Several plasmonic-lens dies are scanned using the pulled fiber probe. A plasmonic-lens die consists of two parts (Fig.2.3) – (a) a dimple lens and (b) a grating in-coupler

In order to compare the performance of the plasmonic-lens, the optical data from the NSOM scans of the plasmonic-lens die (Fig.5.10) is compared to a die that comprises of only a grating in-coupler (Fig.5.9).

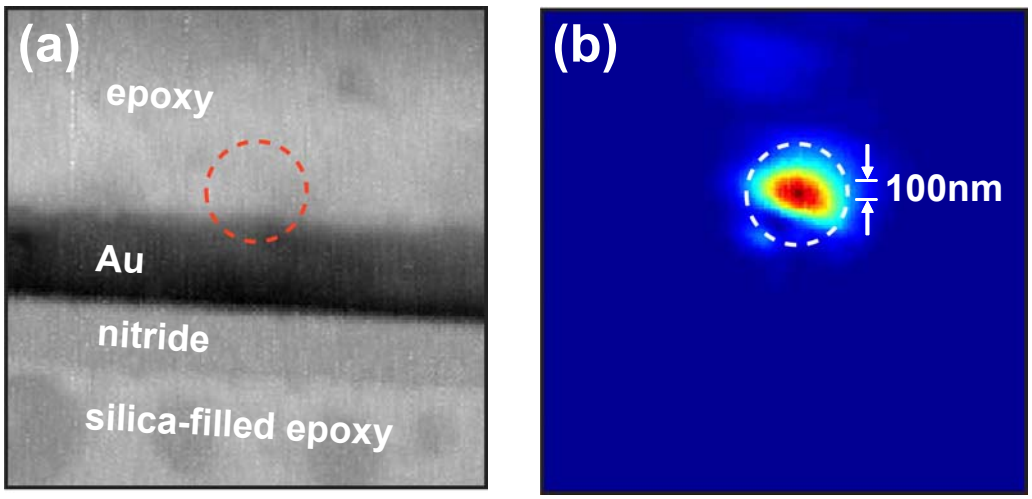

Figure 5.9 (a) Topographic and (b) scanned optical images of a plasmonic-lens die *without* plasmonic dimple lens (*only* grating in-coupler) obtained by Near-field Scanning Optical Microscopy (NSOM) technique. All the scans are 2.5μm×2.5μm.

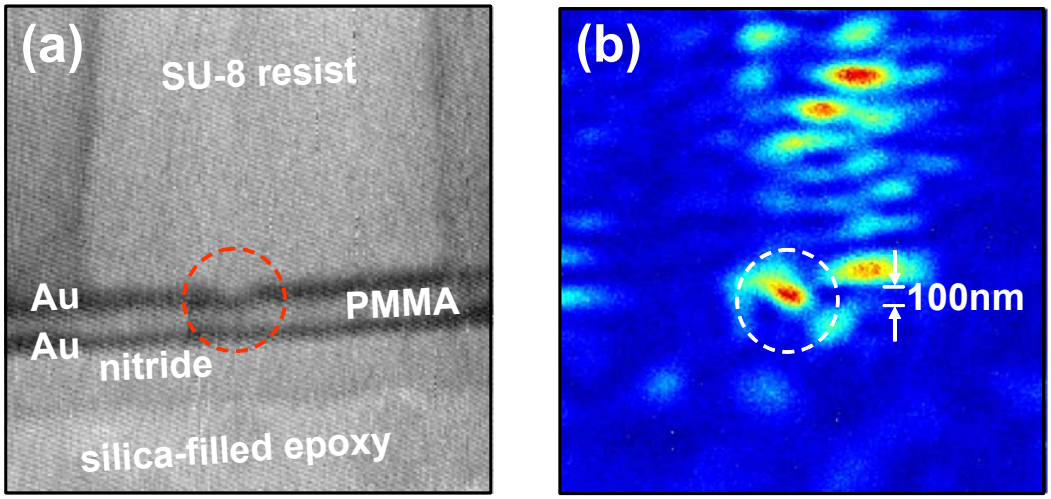

Figure 5.10 (a) Topographic and (b) scanned optical images of a plasmonic-lens die *with* plasmonic dimple lens (*and* grating in-coupler) obtained by Near-field Scanning Optical Microscopy (NSOM) technique. All the scans are 2.5μm×2.5μm.

The comparison between Fig 5.10(b) and Fig. 5.9(b) clearly indicates the focusing effect of the plasmonic dimple lens in terms of the spot-size. (Note that the color-scales of optical images are not equal. Hence comparison should be made only in terms of absolute spot size and not on the basis of output intensity).

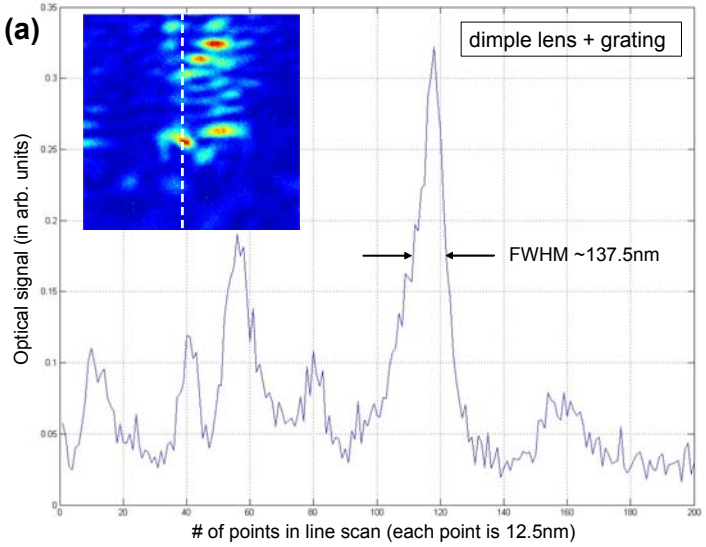

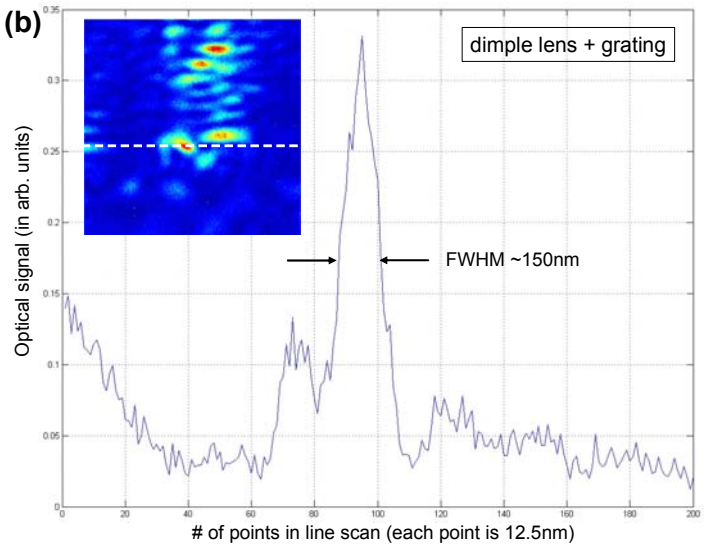

Figure 5.11 Cross-sectional line scans of scanned optical images of a plasmonic-lens die *with* dimple lens (*and* grating in-coupler). (a) Vertical line scan and (b) Horizontal line scan.

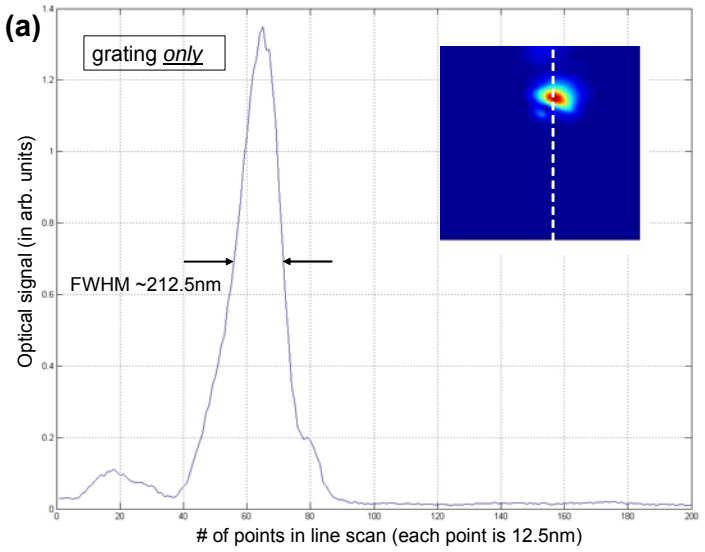

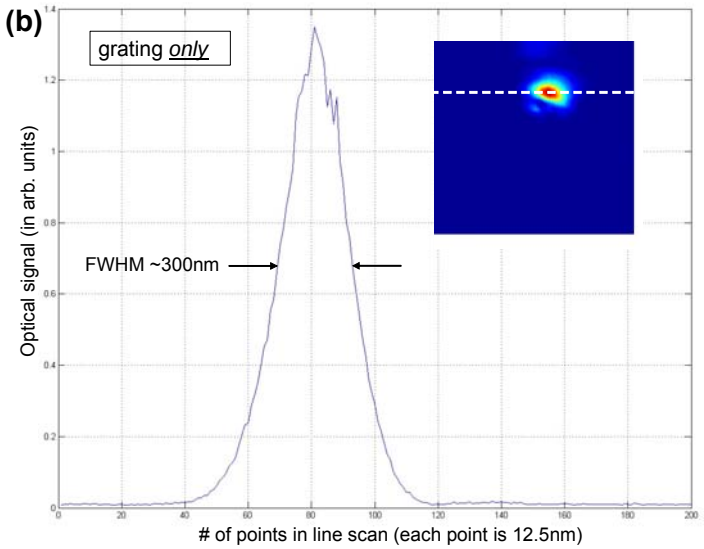

Figure 5.12 Cross-sectional line scans of scanned optical images of a plasmonic-lens die *with* grating in-coupler *only* (*NO* dimple lens). (a) Vertical line scan and (b) Horizontal line scan.

Fig. 5.11 and Fig. 5.12 give the cross-sectional line scans of the optical images of plasmonic-lens dies depicted in Fig. 5.9(b) and Fig. 5.10(b) (with and without the dimple lens), respectively. It is important to note that the nominal aperture of the pulled-fiber probes used for this measurement is between 100-150nm. More discussion on the absolute spot-size measurement is found in the last section of this chapter.

We also observe some additional hotspots that look somewhat like interference fringes of varying intensity over the SU-8 region. Fig. 5.13 shows four different scans of the same plasmonic-lens-die while in the position of incident laser illumination on the grating in-coupler is moved around slightly. It can be seen that that the fringe patterns

slightly move around from one scan to the other but are always over the SU-8 region. Also no such fringes appear in the absence of the SU-8 layer in the die which only has grating in-coupler as in Fig. 5.9(b). Hence this fringe-pattern can be attributed to the interference of the incident light reflected off the upper layer of gold and the back-scattering of this light from the SU-8 − epoxy interface due to refractive-index mismatch between these two materials. (Note epoxy is optically transparent epoxy that cannot be seen in the corresponding topographic images of Fig. 5.13. Instead this layer can be seen in Fig. 5.3(h) & (i)).

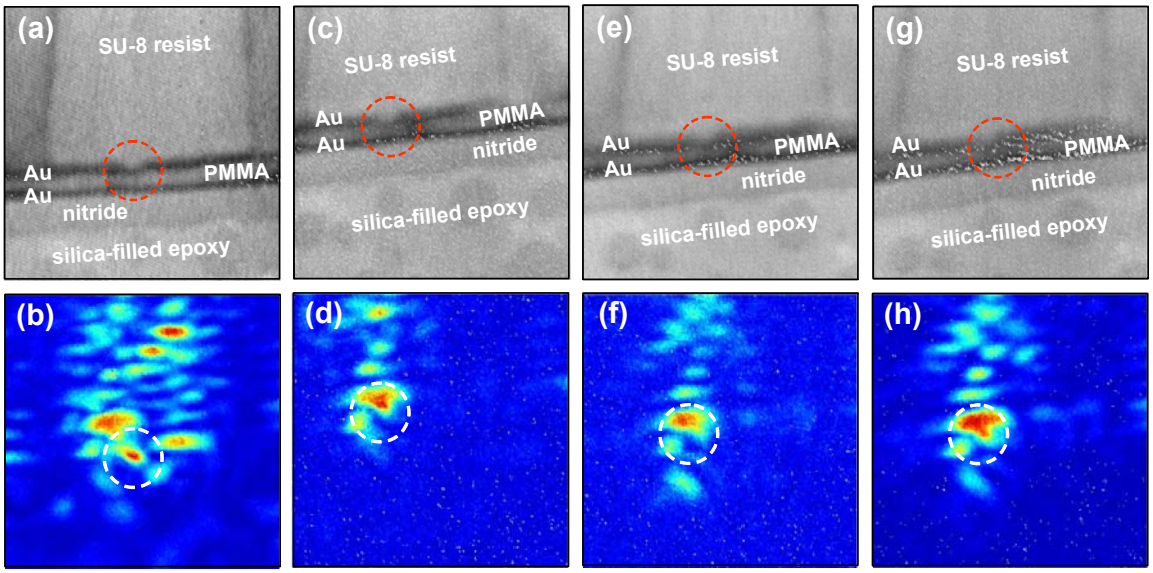

Figure 5.13 (a), (c), (e), and (g) Topographic and (b), (d), (f), and (h) scanned optical images of a single plasmonic-lens die *with* plasmonic dimple lens (*and* grating in-coupler). All the scans are 2.5µm×2.5µm.

In order to ascertain deduction in the above paragraph, each of these scans was overlaid on the top of the others. Care was taken to rotate each topographic and optical

scan so as to align the dimple-lens region before juxtaposing once scan over the other. As seen in Figure5.14, this juxtaposition averages out the hotspots and fringes that appear over the SU-8 region while reinforcing the optical focusing in the dimple region. However we also find that the absolute size of the focused spot increases in this process.

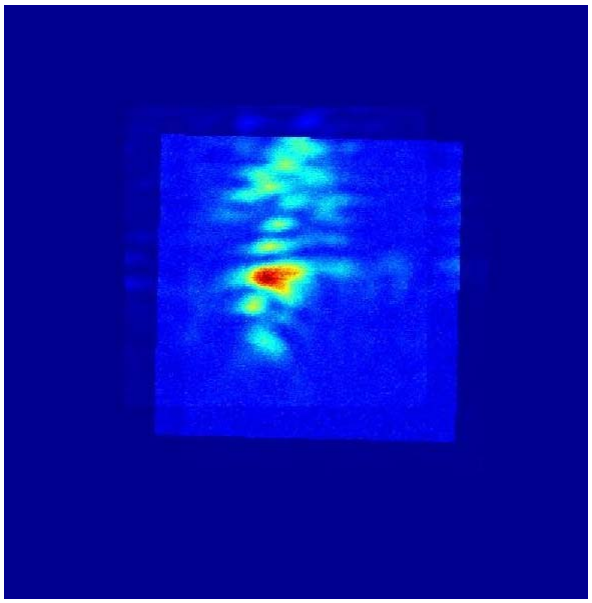

Figure 5.14 Juxtaposition of the four optical scans of Fig.5.13 (b), (d), (f), and (h).

5.5 Limitations to the experimental characterization

Also note that no two scans of the same die identical even when scanned by the same fiber probe. This is evident in both the topographic and optical scans of Fig. 5.13. It has been observed that the fiber-probe wears out in time due to heating or intermittent frictional contact with the surface due to specks of dirt on the surface. Whatever be the

cause, the effects are (i) an increase in the aperture size and (ii) the degradation in the quality of topographic scan. Therefore, even though we start with a fiber-probe with a nominal aperture size of 100-150nm, the data is usually obtained from an aperture that is significantly larger than the aforementioned aperture size.

Another potential limitation in this experimental set-up is movement of the sample (and stage) is x, y, and z direction during the scan while the incident illumination and the fiber-probe is stationary. This means that during the scan of size 2.5μm, the incident beam moves across half the length of the grating in-coupler. Strictly speaking, this will affect the exact measurement of the FWHM of the line scans that determine the spot size of the focused intensity. However this is only a secondary concern because we are limited in our ability to make absolute spot size measurements by the aperture size of the pulled-fiber probe as mentioned in the preceding paragraph.

Thirdly, it has been observed that repeated scanning of a plasmonic lens for long periods of time while the laser beam incident on the grating in-coupler degrades plasmonic lens itself. The topographic AFM scans of the polished out-coupling facet before and after the NSOM measurement show that the PMMA structural layer of the dimple lens gets eroded or sinks in when compared to the surrounding area. This dishing effect also seems to affect the adhesion of the adjacent gold layers to the sandwiched PMMA and nitride layer. One of the reasons for this can be prolonged heating of the layers by the incident laser beam and potentially by the focusing action of the dimple lens

itself. Another suspected reason is the intermittent contact of the fiber-probe with the plasmonic lens facet that gives rise to collisional impact to both the fiber-probe and the surface. The quality of tracking the surface while scanning is worse for a large diameter fiber-probe using shear force feedback when compared to a say, a sharp tip (in an AFM) that uses Van der Waals' force feedback.

Chapter 6 State-of-the-art and future directions

This dissertation describes the design, fabrication, and experimental characterization of a novel plasmonic dimple lens structure in Au-dielectric-Au geometry for focusing visible light to the nanoscale. Comparison of measurements of the circular grating coupler alone and the circular grating coupler together with a dimple lens reveal additional focusing provided by the plasmonic dimple lens. However, the measurement of the final spot size produced by the dimple lens was not possible due to the resolution limit of the pulled-fiber NSOM probe used in the experiment. Our plasmonic lens is capable of focusing light to spot sizes smaller than the aperture size of the commercially available pulled-fiber NSOM probes.

The fabrication strategy is such that the critical dimension of this plasmonic lens is controlled by the layer thickness of the dimple gap, and NOT by the transverse lithographic limitations of electron beam or ion beam processes or equipment. The mechanical edge-polishing step in our fabrication sequence lends itself to be easily adopted by the process flow of the magnetic read-write head of a commercial hard drive. Thus, this structure could potentially be an excellent candidate for the Heat Assisted Magnetic Recording (HAMR) technology, where the plasmonic dimple lens would be used to focus light to provide the strong local heating required for the next generation higher density hard drives [7, 8].

Towards the end of the last chapter, some drawbacks of the NSOM experimental setup were outlined which limited our ability to measure the focused spot size of the optical energy at the out-coupling facet of the plasmonic dimple lens. This chapter suggests some methods to overcome the limitations of our NSOM measurement as mentioned in Section 5.5 and presents a couple of new schemes of characterizing the plasmonic dimple lens.

It also discuses the photochemistry of certain polymers that could be used to detect the light focused by the plasmonic lens. A few different variations to bring light into the plasmonic lens are presented. Then this chapter discusses state-of-the-art progress in the field of plasmonics and metal-optics by covering some new concepts and peer research.

6.1 Photoresist based testing

In order to determine the spot size of the energy emerging out of the plasmonic lens, we need a means to record this in some medium. Photoresists are polymers which absorb light. This causes a chemical change in the photoresist which can be processed to convert it into a physical change.

To characterize the plasmonic lens, the idea is to put a drop of negative photoresist on the polished out-coupling facet of the lens [51, 52]. When the plasmons are excited and the near field energy emerging out of the facet causes negative photoresist to crosslink in the parts where the energy is high enough. When developed in an appropriate developer solution, the cross-linked region remains behind on the out-coupling facet. An AFM scan would show the dimensions of a small blob of resist remaining behind as shown in the Fig. 6.1.

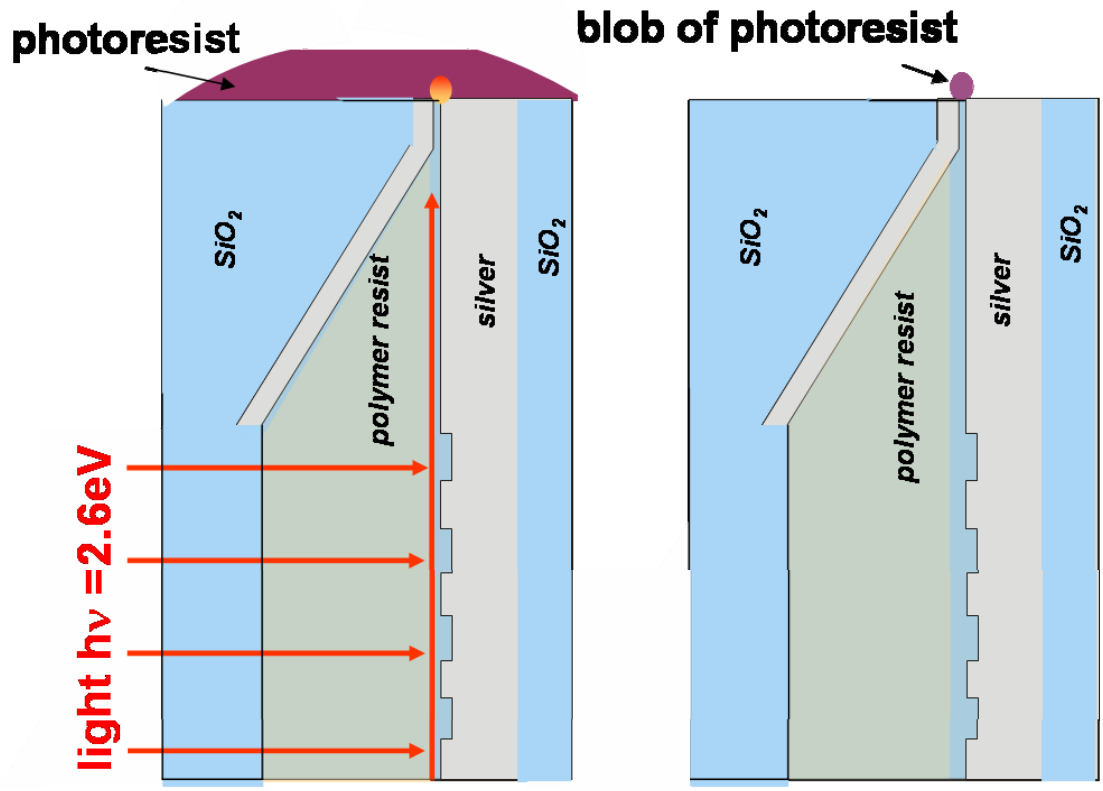

(a) **(b)**

Figure6.1 (a) A plasmonic lens with a drop of photo-resist before development (b) after development a blob of resist is expected to remain behind on the facet. (While this scheme works for any

wavelength of operation, it was initially studied at wavelength of operation of 488nm to be used with silver plasmonic dimple lens)

Commercial photoresists are designed to work at i-line (365nm) or g-line (426nm). A special resist that absorbs at 488nm is made by Prof. Frechet's group at UC Berkeley [53]. This resist consists of camphorquinone which is the photosensitive compound, an initiator and a polymer. After the light is absorbed by the photoactive compound, the initiator gets activated and started cross linking the polymer chains. This resist can be spun down to a thickness of ~50-60nm. The solvent and developer for this resist is anisole.

To detect the sensitivity of this resist to 488nm of light, this wavelength was coupled to a NSOM probe and the resist was exposed to write lines with the NSOM probe. After development, AFM scans show lines of FWHM of ~250nm (Figure6.2).

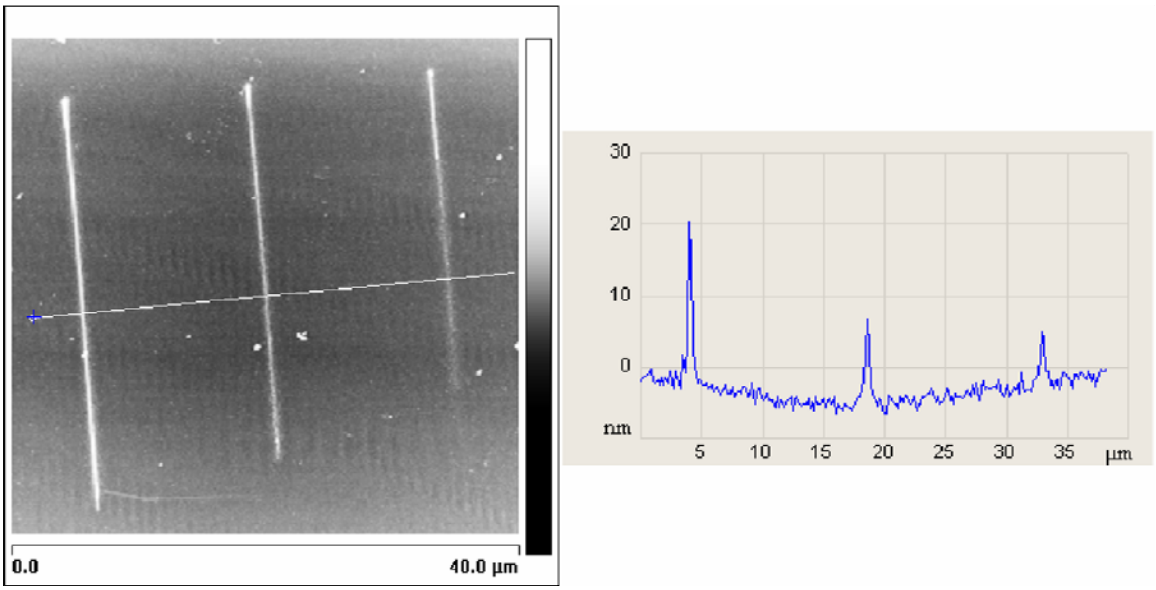

Figure6.2 AFM scan of cross-linked resist that is sensitive at 488nm

The drawback of this resist is that its solvent and developer is anisole. PMMA, in which the dimple is made, is also soluble in anisole. Hence this resist is not suited for the characterization of plasmonic lens as per the scheme depicted in Figure6.1

The features and limitations of this scheme of characterization are as follows –

- The solvent and the developer for this the photoresist must be such that they do not attack PMMA which is the structural layer of the plasmonic lens.
- The smallest resolution one can get out of a photoresist is limited by the diffusion of the photo-activated species. For most resists, this is on the order of ~40nm.
- In the present scheme, light is brought sideways into the device. However the incident light, if its intensity is high enough, could potentially cause the photoresist to get exposed.

To address the first of the above points, a commercial novolak-based resist AZ5214-E was characterized for its sensitivity at 488nm. The novolak based resists are soluble in alkaline developers. Their solvent is PGMEA. Silver and PMMA appear to be very mildly attacked by the developer or the solvent. This resist is a special formulation which can be used as either positive or negative tone resist designed to work at i-line. However it can also weakly absorb at 488nm. Using both NSOM probe as well as using the focused laser light, it was seen that the AZ5214-E crosslinks at 488nm.

In order to beat the diffusion-limited achievable resolution of ~40nm in photoresists, one could use a bottom-up approach where a substrate can be coated with photosensitive monolayer which can be selectively exposed and subsequently, longer and bigger molecules can attach themselves to the photo-activated sites on the monolayer, thereby building up a mask for pattern transfer into the substrate underneath.

There are materials which change phase when exposed to high intensity of light. Also there are materials like PMMA-DR1 [54-56], which undergoes change in isomerization that translates into a topographic change on photo-absorption. Such materials should also be studied as possible alternatives to photoresists.

6.2 Apertureless NSOM characterization

Section 5.5 discusses the aperture size of ~100-150 nm as the major drawback of a fiber-probe based NSOM that has been used to test the plasmonic dimple lens. In order to be able to quantitatively measure the spot size and thereby the performance of our novel lens, building an apertureless NSOM test-bed is suggested [57, 58].

A fiber-probe used its sub-wavelength aperture (~ 100-150 nm) to collect the energy in the near-field of a surface. In contrast, an apertureless NSOM technique is based on the scattering of light in the near-field by a sharp tip and collecting the scattered light in the far-field. Fig. 6.3 depicts a schematic of an apertureless based NSOM.

Typically a sharp silicon based AFM tip with a radius of curvature of 10-15 nm, can be used to scatter light from the out-coupling facet of the plasmonic dimple lens. In principle, an apertureless technique can improve the resolution of measurement over an aperture-based technique by an order of magnitude.

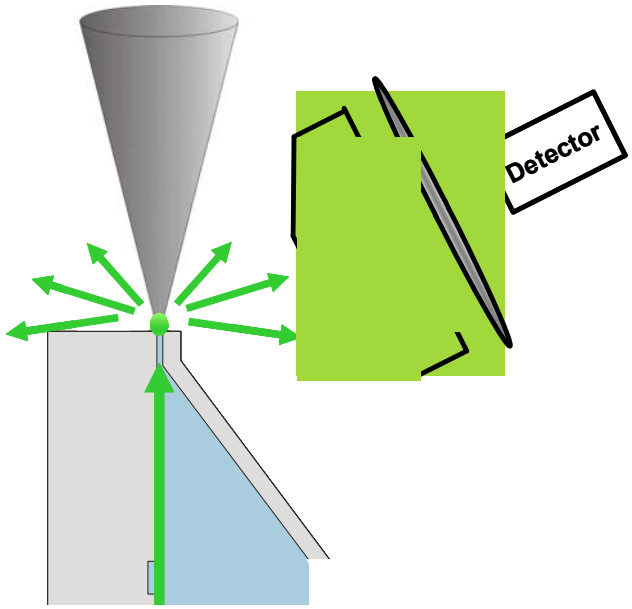

Figure6.3 Apertureless scattering technique to measure near-field intensity at the focus of a plasmonic dimple lens.

The following are a few characteristic features of an apertureless-based NSOM technique particularly when it may be used to characterize out plasmonic dimple lens –

- Since this technique is based on the collection of the scattered light, the scattered signal strength reaching the detector is extremely low. Hence heterodyne measurement is used in this technique.

- The sharp probe is almost always a part of an AFM system. Hence it is always located at the end of a cantilever which is driven at its resonance frequency Ω to obtain the force feedback that is necessary for the AFM operation. A diode laser is always incident on this cantilever and the reflection of this beam off the cantilever I used to record the amplitude and phase of the cantilever oscillation. The wavelength of the diode laser is usually about 670nm. Hence an extremely good filter is required to record the near-field signal at 633nm after completely filtering out the 670 nm wavelength.
- Both the sharp end of the tip as well as the cantilever will scatter the 633nm light (wavelength of operation of the plasmonic dimple lens) at the resonant frequency of Ω. The net far-field signal that reaches the detector is combination of the scattering originating from both the aforementioned sources. In order to extract the signal scattered by the sharp probe, the signal is mixed with a carrier at 3Ω (instead of Ω). The near-field signal decays strongly with distance away from the surface. This makes it better detectable at higher harmonics of the cantilever drive frequency.
- Another salient feature of AFM-based apertureless scattering technique is that the AFM system provides the x,y, and z movements, all to the scanner head onto which the probe-tip is mounted. Thus the sample as well as the incident illumination is stationary throughout the scan.

6.3 Substituting PMMA with an oxide layer

Another issue focused in Section 5.5 is the degradation of PMMA structural layer of the plasmonic dimple lens during the fiber-probe based NSOM characterization. Also Section 6.1 discussed the issues photoresist-based testing of the plasmonic dimple lens because of the incompatibility of the PMMA with the photoresist developer solution. To overcome these problems, it is best to replace the PMMA layer with an oxide layer.

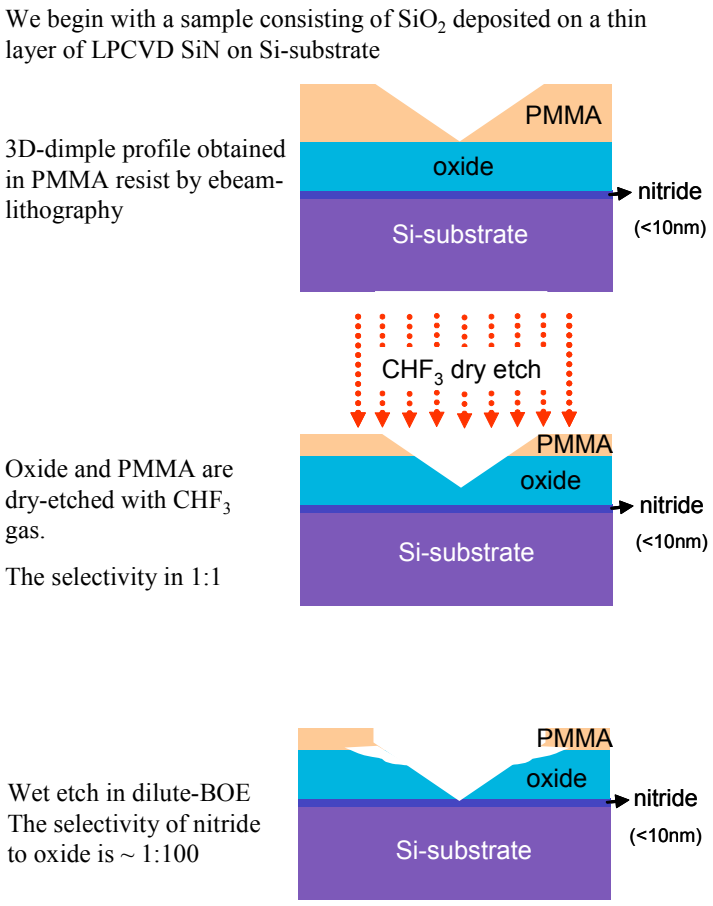

Figure6.4 Scheme to transfer the dimple-pattern from PMMA to oxide layer

It must be noted that the polymer-nitride approach for the taper-structure (Section 4.3) is being replaced by the oxide-nitride approach. The 3D dimple shape will be formed in the oxide layer where as the thin nitride layer will determine the final spot size achieved by the plasmonic dimple lens. Fig. 6.4 describes a sequence of steps that can accomplish this task. This sequence of steps also requires a thorough characterization of dry and wet rates of oxide and nitride layers.

6.4 Improving the in-coupling of light

In–coupling of light into the plasmonic lens or tapered transmission line structure is an area that needs improved from the so far presented scheme of using only a grating in-coupler. In Section 5.4, the laser light was incident on the grating in-coupler that is located at the very edge of the sample. This leads to the spilling of light all over on the out-coupling polished facet of the plasmonic dimple lens.

Apart from using a grating in-coupler, other ways to bring in the light to the "mouth" of the plasmonic lens, is by means of waveguides. Light confined to the waveguide could be used to end-fire couple into the plasmonic dimple. The thickness of the waveguide layers could be adjusted such that the propagation vector of the waveguide mode equals that of the surface plasmon that is to be launched by end firing into the dimple. Since the fabrication of the waveguide must be compatible with the fabrication of the plasmonic lens. While operating at 488nm, one could envision a waveguide

consisting of a silicon nitride core and a silicon oxide clad. A more involved waveguide design would be an adiabatic in plane tapering of the waveguide that matches up with the size of the dimple lens (which is about ~200nm in diameter).

Another schematic of using a grating in-coupler in conjunction with an edge-reflecting parabolic mirror [59] is shown in Figure6.5. A laser beam is directly incident of the grating in-coupler in this figure. This configuration pushes the grating as far away from the focusing nanostructure as possible.

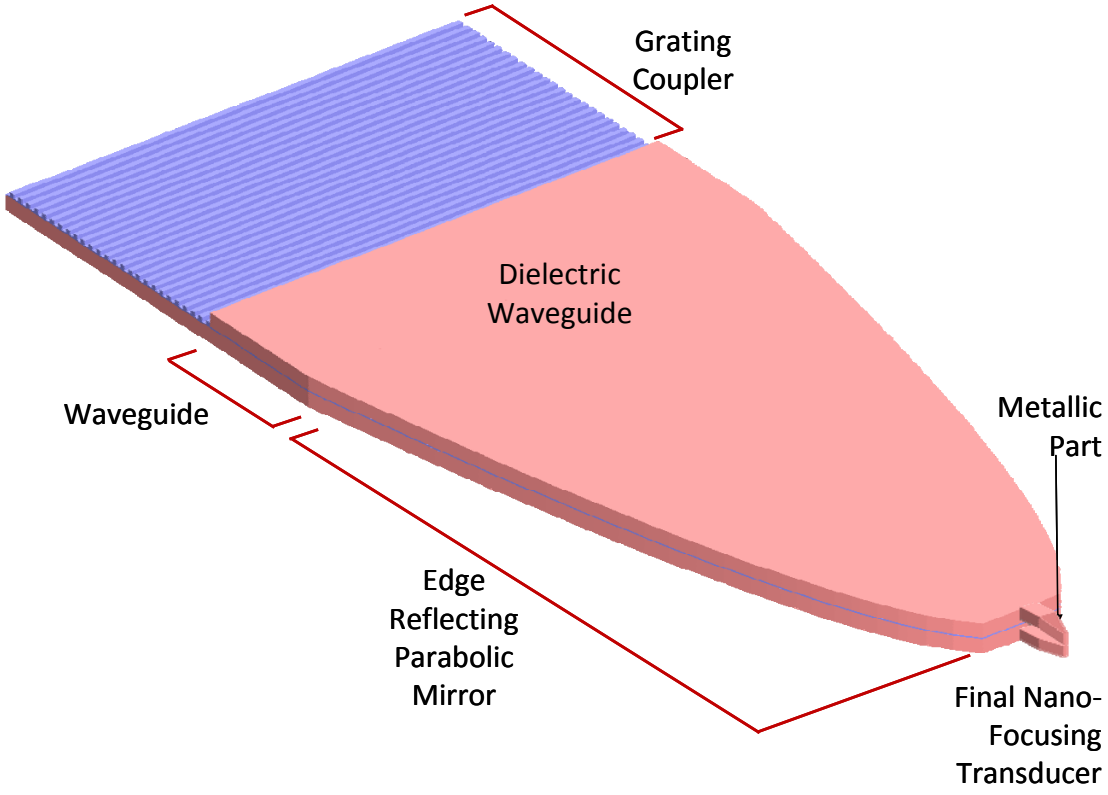

Figure 6.5 An in-coupling scheme that involves a grating coupler and dielectric waveguide shaped into an edge reflecting parabolic mission on its periphery.

6.5 Optical transformer

In Section 2.7 it was observed that as the width W of a transmission line (Figure2.11) scales down, its characteristic impedance Z increases. In Figure2.15, the energy transfer efficiency was expressed in terms of voltages and impedances that were used to model a transmission line. If d_{in} and d_{out} are respectively the spacing between the metal plates at the entrance and the exit of the transmission line as shown in inset of Figure6.6, we can assign expressions for fields $E_{in}=V_{in}/d_{in}$ and $E_{out}=V_{out}/d_{out}$.

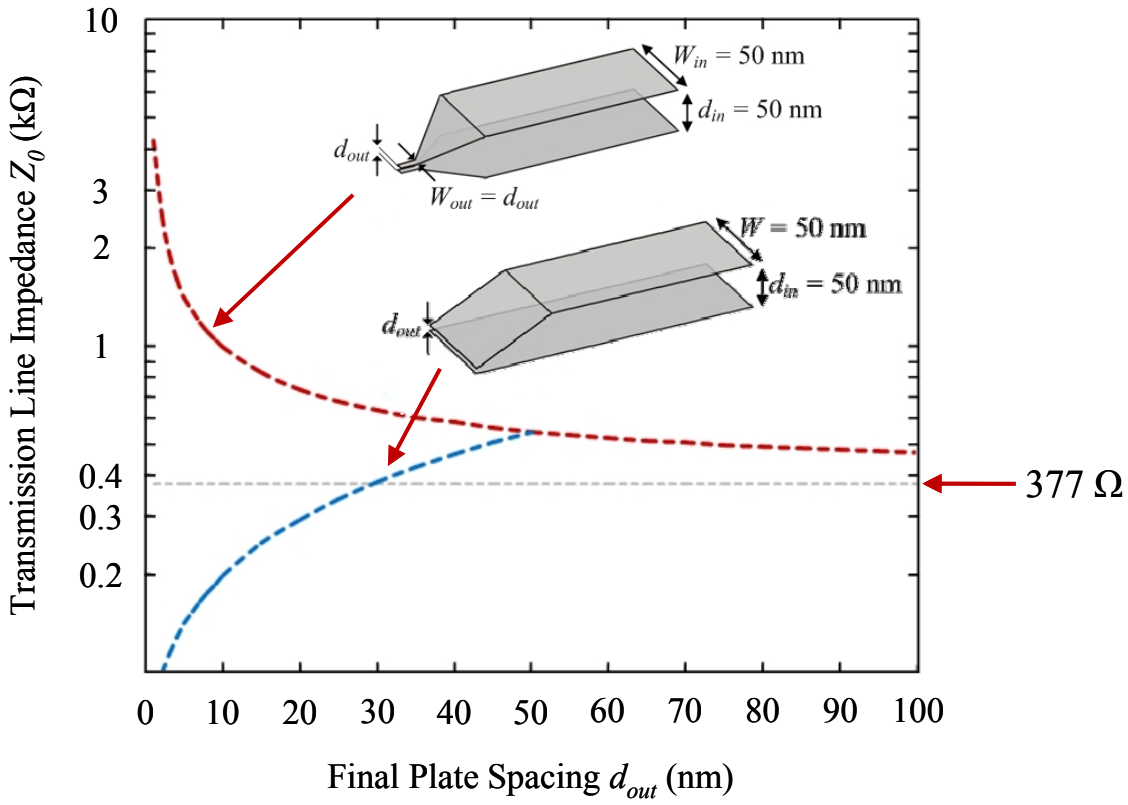

Figure 6.6 A plot of transmission line output impedance Z_{out}, of Au-air-Au transmission line at photons of 1.5eV [60]

Similarly power at the input and output ends of the transmission line are given by $P_{in} = V_{in}/Z_{in}$ and $P_{out} = V_{out}/Z_{out}$. Therefore, $\frac{E_{out}}{E_{in}} = \frac{d_{in}}{d_{out}}\sqrt{\gamma\frac{Z_{out}}{Z_{in}}}$ where $P_{out} = \gamma P_{in}$.

Hence as long as $Z_{out}/Z_{in} > 1/\gamma$, there is a localized electric field enhancement at the output end of the transmission line when compared to the input end. Some estimates on the electric field enhancement are found in reference [60]. This means that a 2D tapered transmission line behaves like an impedance transformer at the nanoscale and since the impedance Z_{out} can be made large enough by decreasing W, we can achieve high electric fields in nanoscopic volumes that can usher in a lot of new applications one of which is discussed in the following paragraph.

Consider a molecule of diameter $a \sim$ 1nm. Its capacitance in the order of $\varepsilon_0 a \approx 10^{-20} F$. Its capacitive reactance $X_C = \frac{1}{j\omega C} \approx -j45k\Omega$ at λ= 826nm (i.e. for a photon energy of 1.5eV). Now Figure6.6 shows the transmission line output impedance Z_{out} as a function of free space plate spacing d for a gold-air-gold MIM structure at 1.5ev. This plot is based on the expressions that were discussed in Section 2.7.

We observe that the as the ratio W and d of the parallel plate transmission line are scaled down together, the impedance Z_{out} increases assuming a value of ~ 4.5kΩ for W=d

~1nm for photon energy of 1.5eV. This impedance is about an order of magnitude lower than that of impedance of a molecule discussed the in the preceding paragraph. However when we refer to the impedance plot of Au-air-Au structure in FigureA-2 (of Appendix A) we note that for photon energies on the order of 2.25ev ($\lambda \sim 550$nm), Z_{out} can be made much larger because kinetic inductance diverges. Thus operating at this wavelength, we would be able to better match the impedance of a molecule to deliver more power to the molecule.

We examine another aspect called the radiation resistance. In order to effectively radiate into free space, any structure would need to have a $Z_{out} = Z_{free\text{-}space} = 377\Omega$. An antenna is an intermediate structure that is able to match the impedance of a radiative system to that of the free space. The radiative resistance R_{rad} of a typical molecule of size $a \sim 1$nm is estimated from the expression $\frac{2\pi}{3}\sqrt{\frac{\mu_0}{\varepsilon_0}}\left(\frac{a}{\lambda}\right)^2$ to be less than 0.5mΩ at a $\lambda=$ 826nm (photon energyof 1.5eV) []. This is much smaller than the impedance of free space, $Z_{free\text{-}space} = 377\Omega$. The impedance transformer action of the tapered parallel plate transmission line could, thus, help couple the molecule radiation to free space better. This concept could be used to better design substrates can be used sensitive detection of trace molecules.

6.6 Fabricating a tapered transmission line structure

It was established in Section 2.5 that the plasmonic dimple lens is equivalent to a tapered transmission line as depicted in Figure2.12. As discussed towards the end of Section 4.3, electron-beam induced deposition of metals and dielectrics can be used to obtain a wedge shaped deposit of silica. Such an approach has been used to fabricate to the structure shown in Figure6.7. This structure shows an electric field enhancement of ~14 over flat gold surface [61] using a two-photo-photo-luminescence measurement (TPPL) as described in these references [52, 62].

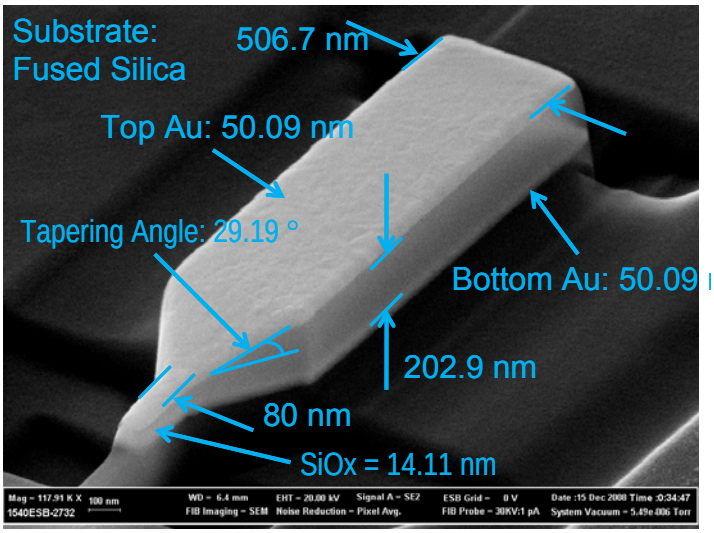

Figure 6.7 A tapered Au-silica-Au transmission line fabricated using electron-beam induced deposition

This approach of fabrication has certain merits over the fabrication-process described in this dissertation to fabricate the semicircular dimple lens in that it does not involve the mechanical polishing step described in Section 4.6. However this structure it

is not viable for near-field surface or optical characterization. Fabricating such a structure at the end of a cantilever may make it more tenable to make near-field energy spot-size and electric field enhancement measurements.

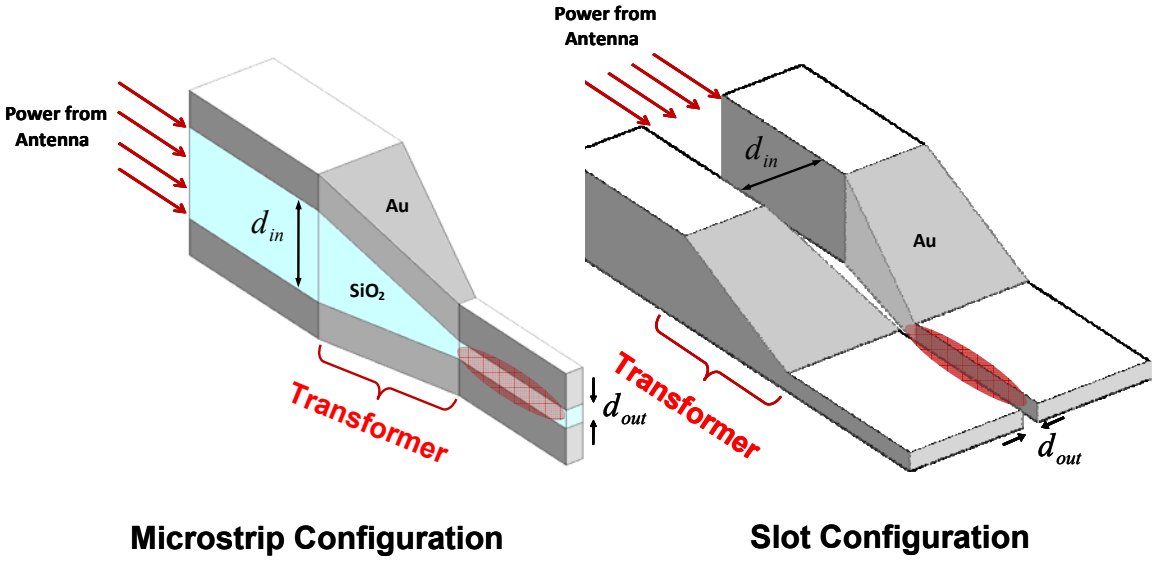

Figure 6.8 A tapered Au-silica-Au transmission line structure in a microstrip and slot configurations.

This work demonstrates the fabrication of 2D tapered transmission line in what would be called a microstrip configuration. Another alternative design is a slot transmission line configuration as seen in Figure6.8. It is interesting to note in the former configuration mandates the wedge-like deposition of dielectric where as the latter requires that of a metal. Also it may be easier to carve out a slot using a focused ion beam in the latter than be able to shape the wedge in the former. Another observation is that a only a slot configuration is amenable when a free-space core or air gap is required. The

microstrip configuration would require the presence of some dielectric material other than air.

An overall comment on gas-induced wedge deposition of dielectric/metal is that the smallest thickness of dielectric/metal would be determined by the minimum thickness of a good quality pin-hole free continuous film of the dielectric that can be deposited on a metal substrate or vice-versa. On the other hand, the fabrication process flow developed for the plasmonic dimple lens ensures good quality dielectric films <5nm needed for the fabrication of 2D tapered microstrip transmission lines. Here the fabrication strategy is such that the critical dimension of this plasmonic lens strcuture is controlled by the layer thickness of the dielectric gap, and NOT by the transverse lithographic limitations of electron beam or ion beam processes or equipment.

6.7 A dark-field plasmonic lens structure

It can be seen from the NSOM data and analysis (Section 5.4) that the plasmonic dimple lens that has been designed (Chapter 2) and fabricated (Chapter 5) is not a dark-field structure. Laser light is incident on the grating that is located at the very edge of the sample. This issue can be minimized by the designing a dielectric waveguide that has been discussed in Section 6.4.

Another dark-field structure has been proposed which can effectively shield off the incident light from the out-coupling side. Figure6.9 shows a tapered pin-hole located at the center of the circular grating coupler fabricated in an optically opaque thickness of metal that can achieve dark-field.

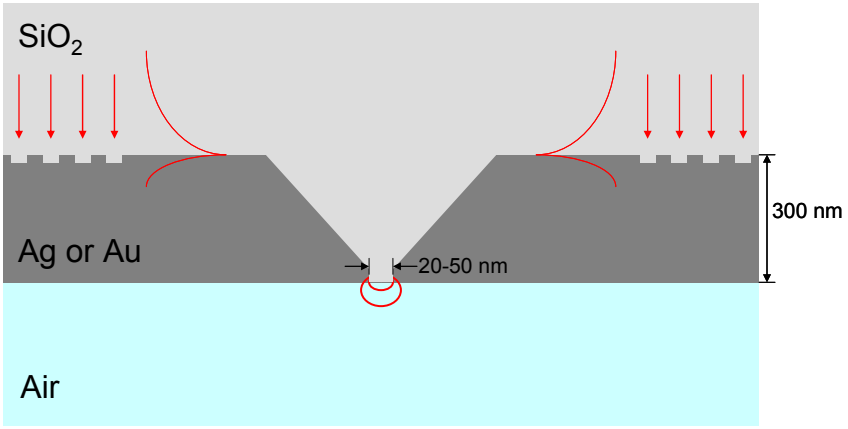

Figure 6.9 A dark-field structure comprising of a tapered pin-hole located at the center of a cicular grating coupler.

The incident light get coupled into surface plasmons that funnels into the pinhole which acts as an antenna radiator to effective concentrate electric field in the near-field of the hole. Figure6.10 shows the fabricated structure and reference [63] discusses the experimental results and analysis of this device.

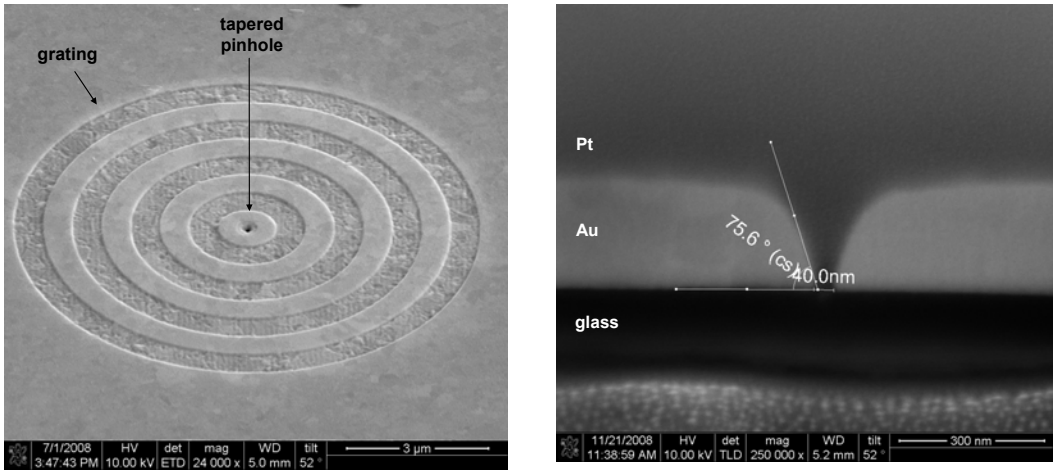

Figure 6.10 (Left) A circular grating coupler with a tapered pin-hold at its center, (right) SEM image of the tapered pin-hole fabricated with a focused ion beam (FIB) machine.

6.8 Conclusions

This dissertation has outlined the design, fabrication and experimental characterization of a novel plasmonic dimple lens, which can focus down the energy of the surface plasmons to the nanoscale. The experimental results show the focusing action of the dimple lens qualitatively. The fabrication strategy is such that the critical dimension of this plasmonic lens is controlled by the layer thickness of the dimple gap, and NOT by the transverse lithographic limitations of electron beam or ion beam processes or equipment. Several methods are suggested to quantitatively characterize the nanofocusing of this dimple lens. It is hoped that this novel design and new insights will usher in new discoveries at nanoscale.

Appendix A

Impedance plot for Gold wire and gold slab

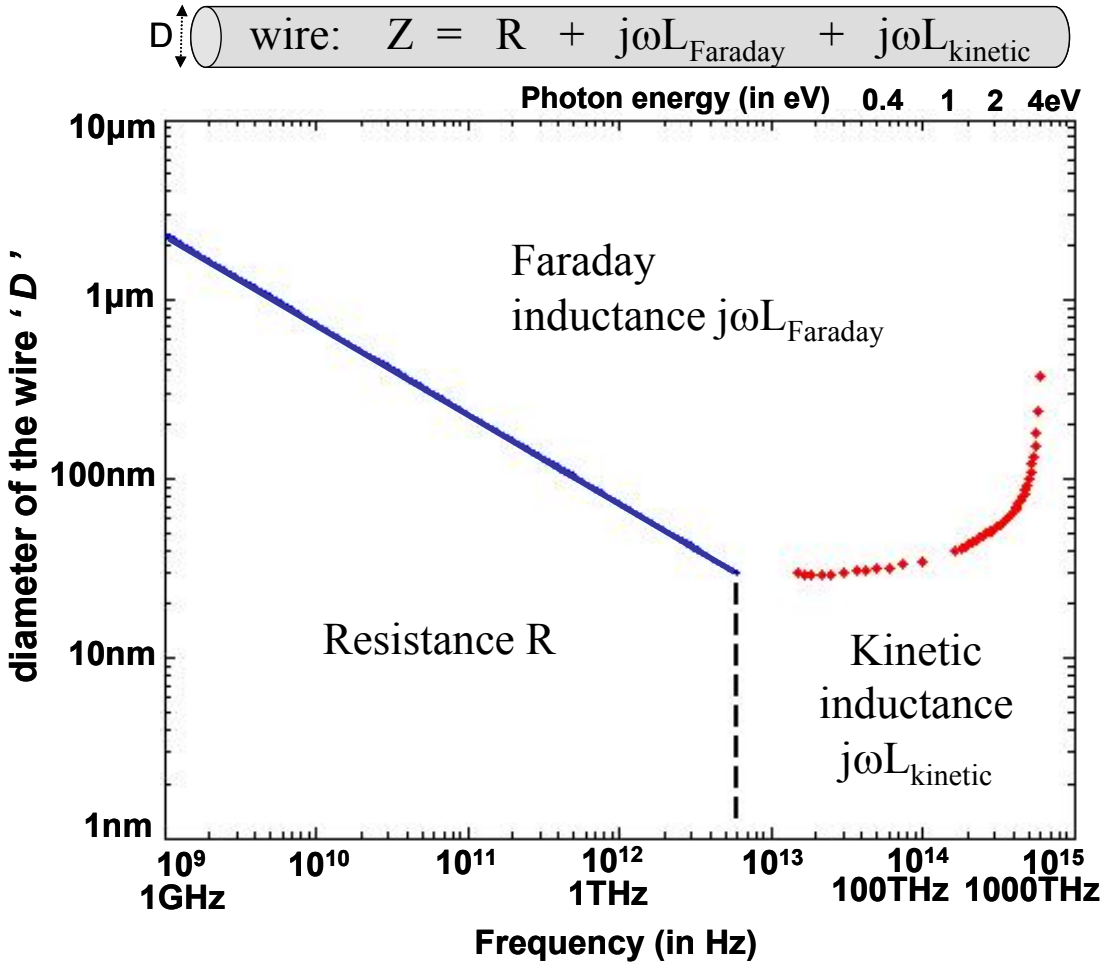

Figure.A-1 A dominant-impedance plot of a gold wire in different length-scale vs frequency regimes

The expression for each of the impedances is given by the following.

$$R = \frac{\varepsilon_r''(\omega)}{\omega\ \varepsilon_0 \left|1-\varepsilon_r'(\omega)\right|^2}\frac{(length)}{(area)} \qquad L_k = \frac{1}{\omega^2 \varepsilon_0 (1-\varepsilon_r'(\omega))}\frac{(length)}{(area)}$$

where $area = 2\pi r_1 \delta$

$$L_f = \frac{\mu_0}{2\pi} \ln\left(\frac{r_2}{r_1}\right)(length)$$

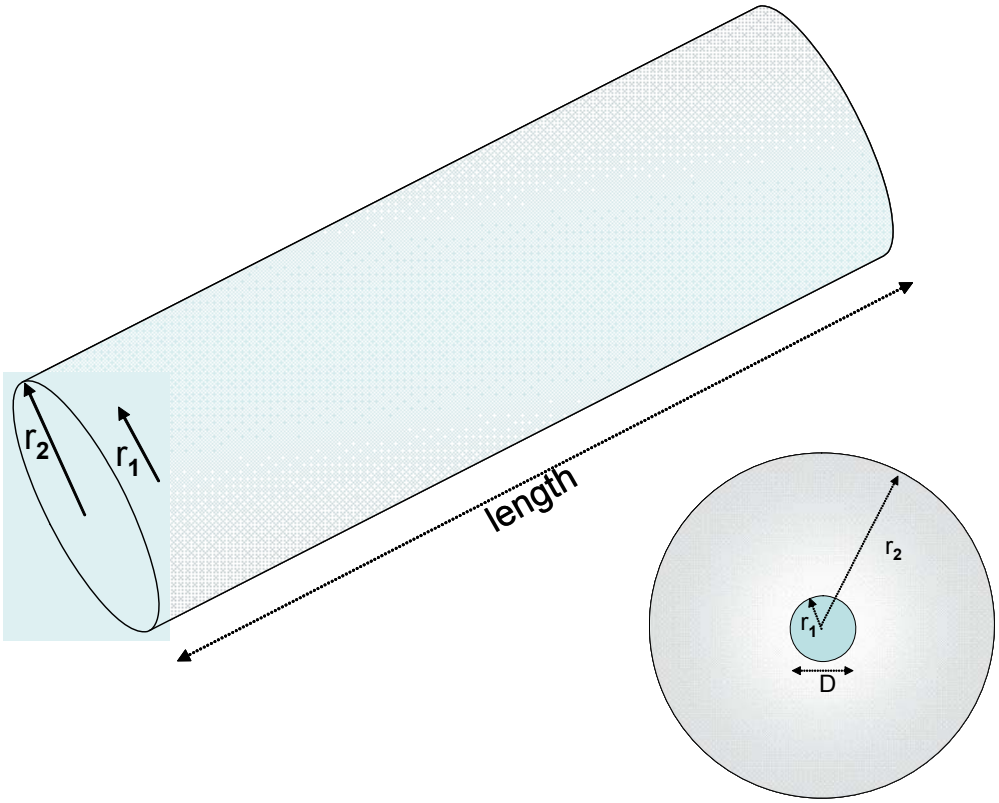

Note that the faraday inductance $L_f = \frac{\mu_0}{2\pi} \ln\left(\frac{r_2}{r_1}\right)(length)$ is applicable for coaxial transmission line.

When $r_2 >> r_1$, $\ln\left(\frac{r_2}{r_1}\right) \to 2\pi$ $\therefore$ for a wire of radius r_1, $L_f \approx \mu_0(length)$

The determination of the boundaries in Figure A-1 is on the same lines as described in Section 2.6

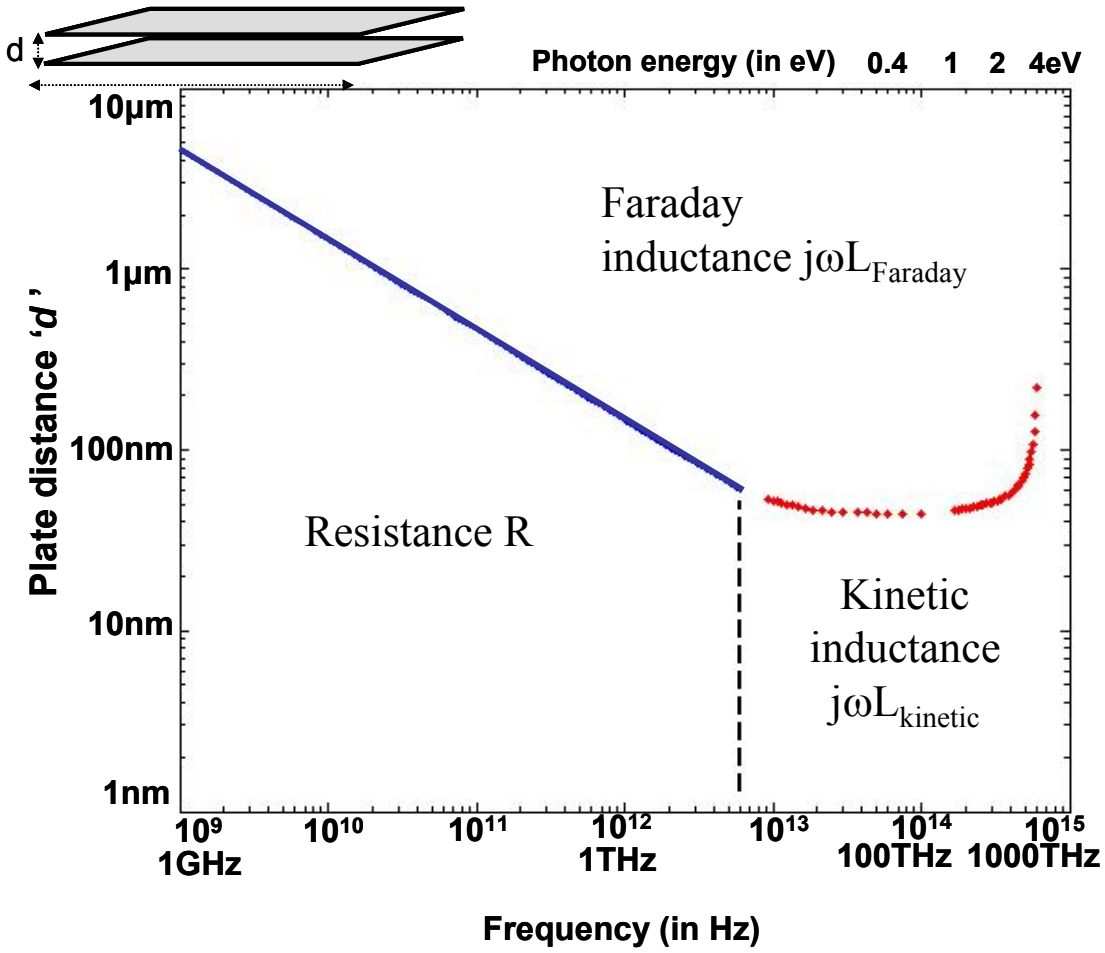

Figure A-2 A dominant-impedance plot of a gold wire in different length-scale vs frequency regimes

The expressions for different impedances used to evaluate the boundaries for Au-air-Au plot are same as the ones described in Section 2.6.

The frequency at which $R = L_k$ is ~ 6 THz. Note that for a silver, this frequency is 4.12 Thz (from Section 2.6). This follows from the fact that conductivity of Au ($\sigma = 4.87\times10^7$ S/m) is slightly smaller than that of silver. Hence Au remains resistive up until 6THz, where as at this frequency, the kinetic inductance starts dominating over resistance in the case of Ag.

Appendix B

Optical constants of gold

Photon energy (in eV)	**Wavelength (in μm)**	ε_r' **(real part of** ε_r**)**	ε_r'' **(imaginary part of** ε_r**)**
0.64	1.9375	-189.042	25.3552
0.77	1.6104	-125.3505	12.5552
0.89	1.3933	-90.4265	8.1863
1.02	1.2157	-66.2185	5.7015
1.14	1.0877	-51.0496	3.861
1.26	0.9841	-40.2741	2.794
1.39	0.8921	-32.0407	1.9254
1.51	0.8212	-25.8113	1.6266
1.64	0.7561	-20.6102	1.2718
1.76	0.7045	-16.8177	1.0668
1.88	0.6596	-13.6482	1.0352
2.01	0.6169	-10.6619	1.3742
2.13	0.5822	-8.1127	1.6605
2.26	0.5487	-5.8421	2.1113
2.38	0.521	-3.9462	2.5804
2.5	0.496	-2.2783	3.8126
2.63	0.4715	-1.7027	4.8444
2.75	0.4509	-1.759	5.2826
2.88	0.4306	-1.6922	5.6492
3	0.4133	-1.7022	5.7174
3.12	0.3974	-1.6494	5.7389
3.25	0.3815	-1.6049	5.6444

3.37	0.368	-1.4006	5.6092
3.5	0.3543	-1.232	5.598
3.62	0.3425	-1.3102	5.5382
3.74	0.3316	-1.3553	5.5737
3.87	0.3204	-1.2308	5.8458
3.99	0.3108	-1.2425	5.7926
4.12	0.301	-1.2274	5.7803
4.24	0.2925	-1.3068	5.5964
4.36	0.2844	-1.3323	5.4949
4.49	0.2762	-1.3665	5.2824
4.61	0.269	-1.3464	4.9763
4.74	0.2616	-1.2365	4.7223
4.86	0.2551	-1.0804	4.4901
4.98	0.249	-0.8913	4.3385
5.11	0.2427	-0.7445	4.1633
5.23	0.2371	-0.6169	4.055
5.36	0.2313	-0.551	3.8922
5.48	0.2263	-0.4155	3.8252
5.6	0.2214	-0.3463	3.7102
5.73	0.2164	-0.2338	3.6062
5.85	0.212	-0.1325	3.51
5.98	0.2074	-0.0104	3.3904
6.1	0.2033	0.1382	3.3968
6.22	0.1994	0.2039	3.3277
6.35	0.1953	0.2925	3.2857
6.47	0.1917	0.2952	3.1759
6.6	0.1879	0.2271	3.0413

Table B-1 Optical constants of gold [64]

Photon energy (in eV)	**Wavelength (in μm)**	ε_r' **(real part of ε_r)**	ε_r'' **(imaginary part of ε_r)**
0.0388	32	-36900	25400
0.0413	30	-33700	21700
0.0443	28	-30600	18400
0.0477	26	-27300	15300
0.0517	24	-24100	12400
0.0564	22	-20800	9890
0.062	20	-17700	7670
0.0689	18	-14800	5780
0.0775	16	-12200	4190
0.0886	14	-9510	2860
0.1033	12	-7140	1840
0.124	10	-5050	1090
0.155	8	-3290	568
0.1771	7	-2540	383
0.2067	6	-1880	242
0.248	5	-1310	141
0.31	4	-839	73
0.4133	3	-475	31

Table B-2 Optical constants of gold [65]

Photon energy (in eV)	**Wavelength (in μm)**	ε_r' **(real part of** ε_r**)**	ε_r'' **(imaginary part of** ε_r**)**
0.0039	318	-86200	623000
0.0046	269	-87400	537000
0.0053	236	-94700	481000
0.0062	200	-91800	400000
0.0075	165	-98700	337000
0.0087	143	-96000	282000
0.0099	125	-99700	247000
0.0113	110	-100000	215000
0.0124	100	-106000	193000
0.0136	90.9	-103000	168000
0.0149	83.3	-104000	149000
0.0161	76.9	-97200	130000
0.0174	71.4	-96600	114000
0.0186	66.7	-85100	100000

Table B-3 Optical constants of gold [66]

Appendix C

Dispersion relation of double-sided plasmons for Au-SiO_2-Au MIM slab structure

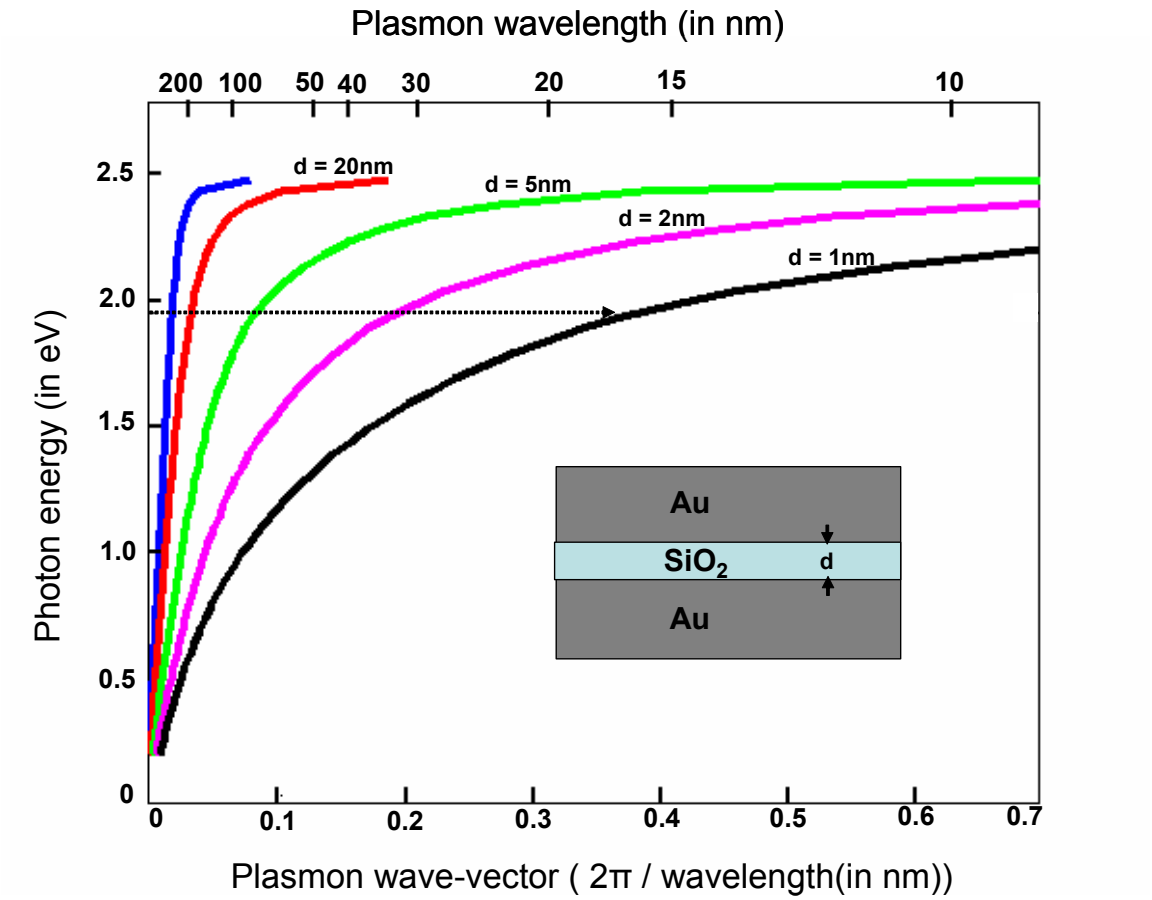

Figure C-1 Dispersion relation for Au-silica-Au MIM slab structure

This plot is generated using the optical constants in Table B-1 in MATLAB. The complex dielectric constant of gold is used in the calculations.

The Matlab code follows:

```
% ---------------------------------------------------
ev=[0.64     0.77     0.89     1.02     1.14     1.26     1.39     1.51
1.64     1.76     1.88     2.01     2.13     2.26     2.38      2.5     2.63
2.75     2.88     3.00     3.12     3.25     3.37      3.5     3.62     3.74
3.87     3.99     4.12     4.24     4.36     4.49     4.61     4.74     4.86
4.98     5.11     5.23     5.36     5.48      5.6     5.73     5.85     5.98
6.10    6.22    6.35    6.47    6.60];
% lambda=0.450:0.050:1.000;

n=[0.92    0.56    0.43    0.35    0.27    0.22    0.17    0.16    0.14
0.13     0.14     0.21     0.29     0.43     0.62     1.04     1.31     1.38
1.45     1.46     1.47     1.46     1.48      1.5     1.48     1.48     1.54
1.53     1.53     1.49     1.47     1.43     1.38     1.35     1.33     1.33
1.32     1.32     1.30     1.31     1.30     1.30     1.30     1.30     1.33
1.33    1.34    1.32    1.28];

k=[13.78    11.21    9.519    8.145    7.150    6.350    5.663    5.083
4.542     4.103     3.697     3.272     2.863     2.455     2.081     1.833
1.849     1.914     1.948     1.958     1.952     1.933     1.895     1.866
1.871     1.883     1.898     1.893     1.889     1.878     1.869     1.847
1.803     1.749     1.688     1.631     1.577     1.536     1.497     1.460
1.427     1.387     1.350     1.304     1.277     1.251     1.226     1.203
1.188];

epsreal=n.^2-k.^2;
epsimag=2.*n.*k;

lambda=1.24./ev;

ereal=spline(lambda,transpose(epsreal));
eimag=spline(lambda,transpose(epsimag));


myopt=optimset('MaxFunEvals',500000,'MaxIter',500000);
%%%%%%%% solving dispersion relation %%%%%%%%%
 %%%%%  0.2eV to 3.2eV in steps of 0.05  == 60 steps %%%%%%
 epsd=2.25;

% ---------------------------------------------------

 d=100e-9;
 clear i;
 for j=1:1:37 %---> for generating main disp plot
     energy(j)=0.64+0.05*j; %---> for generating main disp plot
     k0(j)=(2*pi*1e+6)/wavelength(j);
     realepsm(j)=ppval(ereal,wavelength(j));
     imagepsm(j)=ppval(eimag,wavelength(j));

     [kxzero(j),fvalzero(j),exitflagzero(j),outputzero(j)]              =
fzero(@(ksp) expfun(ksp,d,epsd,realepsm(j),k0(j)),2*k0(j));
```

```
     [kxim(j),fvalim(j),exitflagim(j),outputim(j)]                    =
fminsearch(@(kspim)
expmin5fun(kxzero(j),kspim,d,epsd,realepsm(j)+i*imagepsm(j),k0(j)),[1e4
],myopt);
     [kxre(j),fvalre(j),exitflagre(j),outputre(j)]                    =
fminsearch(@(kspre)
expmin5fun(kspre,kxim(j),d,epsd,realepsm(j)+i*imagepsm(j),k0(j)),[2*k0(
j)],myopt);
     [kxim1(j),fvalim1(j),exitflagim1(j),outputim1(j)]                =
fminsearch(@(kspim)
expmin5fun(kxre(j),kspim,d,epsd,realepsm(j)+i*imagepsm(j),k0(j)),[1e4],
myopt);
     [kxre1(j),fvalre1(j),exitflagre1(j),outputre1(j)]                =
fminsearch(@(kspre)
expmin5fun(kspre,kxim1(j),d,epsd,realepsm(j)+i*imagepsm(j),k0(j)),[2*k0
(j)],myopt);

     [kxcomp1(j,:),fvalcomp1(j),exitflagcomp1(j),outputcomp1(j)]      =
fminsearch(@(ksp)
expmin5fun(ksp(1),ksp(2),d,epsd,realepsm(j)+i*imagepsm(j),k0(j)),[kxre1
(j),1e4],myopt); % 1.4 works

 end

  clear j;
 for j=1:1:32
     kxd_100(j)=kxcomp1(j,1);
     energy_100(j)=energy(j);
     end
 clear j;
 clearvars kx* -except -regexp 100$
 clearvars fval* exitflag* output*

% ------------------------------------------------


d=20e-9;
 clear i;
 for j=1:1:37 %---> for generating main disp plot

     energy(j)=0.64+0.05*j; %---> for generating main disp plot
     wavelength(j)=1.24/energy(j);
     k0(j)=(2*pi*1e+6)/wavelength(j);
     realepsm(j)=ppval(ereal,wavelength(j));
     imagepsm(j)=ppval(eimag,wavelength(j));

     [kxzero(j),fvalzero(j),exitflagzero(j),outputzero(j)]            =
fzero(@(ksp) expfun(ksp,d,epsd,realepsm(j),k0(j)),3*k0(j));
     [kxim(j),fvalim(j),exitflagim(j),outputim(j)]                    =
fminsearch(@(kspim)
expmin5fun(kxzero(j),kspim,d,epsd,realepsm(j)+i*imagepsm(j),k0(j)),[1e6
],myopt);
     [kxre(j),fvalre(j),exitflagre(j),outputre(j)]                    =
fminsearch(@(kspre)
```

```
expmin5fun(kspre,kxim(j),d,epsd,realepsm(j)+i*imagepsm(j),k0(j)),[3*k0(
j)],myopt);
     [kxim1(j),fvalim1(j),exitflagim1(j),outputim1(j)]                =
fminsearch(@(kspim)
expmin5fun(kxre(j),kspim,d,epsd,realepsm(j)+i*imagepsm(j),k0(j)),[1e6],
myopt);
     [kxre1(j),fvalre1(j),exitflagre1(j),outputre1(j)]                =
fminsearch(@(kspre)
expmin5fun(kspre,kxim1(j),d,epsd,realepsm(j)+i*imagepsm(j),k0(j)),[3*k0
(j)],myopt);

     [kxcomp1(j,:),fvalcomp1(j),exitflagcomp1(j),outputcomp1(j)]      =
fminsearch(@(ksp)
expmin5fun(ksp(1),ksp(2),d,epsd,realepsm(j)+i*imagepsm(j),k0(j)),[kxre1
(j),1e6],myopt); % 1.4 works

 end

  clear j;
 for j=1:1:32
     kxd_20(j)=kxcomp1(j,1);
     energy_20(j)=energy(j);
 end
 clear j;
 clearvars kx* -except -regexp 20$ 100$
 clearvars fval* exitflag* output*

% ------------------------------------------------


d=5e-9;
 clear i;
 for j=1:1:37 %---> for generating main disp plot

     energy(j)=0.64+0.05*j; %---> for generating main disp plot
     wavelength(j)=1.24/energy(j);
     k0(j)=(2*pi*1e+6)/wavelength(j);
     realepsm(j)=ppval(ereal,wavelength(j));
     imagepsm(j)=ppval(eimag,wavelength(j));

     [kxzero(j),fvalzero(j),exitflagzero(j),outputzero(j)]            =
fzero(@(ksp) expfun(ksp,d,epsd,realepsm(j),k0(j)),3*k0(j));
     [kxim(j),fvalim(j),exitflagim(j),outputim(j)]                    =
fminsearch(@(kspim)
expmin5fun(kxzero(j),kspim,d,epsd,realepsm(j)+i*imagepsm(j),k0(j)),[1e5
],myopt);
     [kxre(j),fvalre(j),exitflagre(j),outputre(j)]                    =
fminsearch(@(kspre)
expmin5fun(kspre,kxim(j),d,epsd,realepsm(j)+i*imagepsm(j),k0(j)),[5*k0(
j)],myopt);
     [kxim1(j),fvalim1(j),exitflagim1(j),outputim1(j)]                =
fminsearch(@(kspim)
expmin5fun(kxre(j),kspim,d,epsd,realepsm(j)+i*imagepsm(j),k0(j)),[1e5],
myopt);
```

```
     [kxre1(j),fvalre1(j),exitflagre1(j),outputre1(j)]                =
fminsearch(@(kspre)
expmin5fun(kspre,kxim1(j),d,epsd,realepsm(j)+i*imagepsm(j),k0(j)),[5*k0
(j)],myopt);

     [kxcomp1(j,:),fvalcomp1(j),exitflagcomp1(j),outputcomp1(j)]       =
fminsearch(@(ksp)
expmin5fun(ksp(1),ksp(2),d,epsd,realepsm(j)+i*imagepsm(j),k0(j)),[kxre1
(j),1e5],myopt); % 1.4 works

 end

 clear j;
 for j=1:1:32
     kxd_5(j)=kxcomp1(j,1);
     energy_5(j)=energy(j);
 end
 clear j;
 clearvars kx* -except -regexp 5$ 20$ 100$
 clearvars fval* exitflag* output*

% ------------------------------------------------


d=2e-9;
 clear i;
 for j=1:1:37 %---> for generating main disp plot
     energy(j)=0.64+0.05*j; %---> for generating main disp plot
     wavelength(j)=1.24/energy(j);
     k0(j)=(2*pi*1e+6)/wavelength(j);
     realepsm(j)=ppval(ereal,wavelength(j));
     imagepsm(j)=ppval(eimag,wavelength(j));

     [kxzero(j),fvalzero(j),exitflagzero(j),outputzero(j)]            =
fzero(@(ksp) expfun(ksp,d,epsd,realepsm(j),k0(j)),10*k0(j));
     [kxim(j),fvalim(j),exitflagim(j),outputim(j)]                    =
fminsearch(@(kspim)
expmin5fun(kxzero(j),kspim,d,epsd,realepsm(j)+i*imagepsm(j),k0(j)),[1e5
],myopt);
     [kxre(j),fvalre(j),exitflagre(j),outputre(j)]                    =
fminsearch(@(kspre)
expmin5fun(kspre,kxim(j),d,epsd,realepsm(j)+i*imagepsm(j),k0(j)),[10*k0
(j)],myopt);
     [kxim1(j),fvalim1(j),exitflagim1(j),outputim1(j)]                =
fminsearch(@(kspim)
expmin5fun(kxre(j),kspim,d,epsd,realepsm(j)+i*imagepsm(j),k0(j)),[1e5],
myopt);
     [kxre1(j),fvalre1(j),exitflagre1(j),outputre1(j)]                =
fminsearch(@(kspre)
expmin5fun(kspre,kxim1(j),d,epsd,realepsm(j)+i*imagepsm(j),k0(j)),[10*k
0(j)],myopt);

     [kxcomp1(j,:),fvalcomp1(j),exitflagcomp1(j),outputcomp1(j)]       =
fminsearch(@(ksp)
```

```
expmin5fun(ksp(1),ksp(2),d,epsd,realepsm(j)+i*imagepsm(j),k0(j)),[kxre1
(j),1e5],myopt); % 1.4 works

 end

  clear j;
 for j=1:1:32
     kxd_2(j)=kxcomp1(j,1);
     energy_2(j)=energy(j);
 end
 clear j;
 clearvars kx* -except -regexp 2$ 5$ 20$ 100$
 clearvars fval* exitflag* output*

% ------------------------------------------------


d=1e-9;
 clear i;
 for j=1:1:37 %---> for generating main disp plot
     energy(j)=0.64+0.05*j; %---> for generating main disp plot
     wavelength(j)=1.24/energy(j);
     k0(j)=(2*pi*1e+6)/wavelength(j);
     realepsm(j)=ppval(ereal,wavelength(j));
     imagepsm(j)=ppval(eimag,wavelength(j));

     [kxzero(j),fvalzero(j),exitflagzero(j),outputzero(j)]            =
fzero(@(ksp) expfun(ksp,d,epsd,realepsm(j),k0(j)),20*k0(j));
     [kxim(j),fvalim(j),exitflagim(j),outputim(j)]                    =
fminsearch(@(kspim)
expmin5fun(kxzero(j),kspim,d,epsd,realepsm(j)+i*imagepsm(j),k0(j)),[1e5
],myopt);
     [kxre(j),fvalre(j),exitflagre(j),outputre(j)]                    =
fminsearch(@(kspre)
expmin5fun(kspre,kxim(j),d,epsd,realepsm(j)+i*imagepsm(j),k0(j)),[20*k0
(j)],myopt);
     [kxim1(j),fvalim1(j),exitflagim1(j),outputim1(j)]                =
fminsearch(@(kspim)
expmin5fun(kxre(j),kspim,d,epsd,realepsm(j)+i*imagepsm(j),k0(j)),[1e5],
myopt);
     [kxre1(j),fvalre1(j),exitflagre1(j),outputre1(j)]                =
fminsearch(@(kspre)
expmin5fun(kspre,kxim1(j),d,epsd,realepsm(j)+i*imagepsm(j),k0(j)),[20*k
0(j)],myopt);

     [kxcomp1(j,:),fvalcomp1(j),exitflagcomp1(j),outputcomp1(j)]      =
fminsearch(@(ksp)
expmin5fun(ksp(1),ksp(2),d,epsd,realepsm(j)+i*imagepsm(j),k0(j)),[kxre1
(j),1e5],myopt); % 1.4 works

 end


  clear j;
```

```
 for j=1:1:32
     kxd_1(j)=kxcomp1(j,1);
     energy_1(j)=energy(j);
 end
 clear j;
 clearvars kx* -except -regexp 1$ 2$ 5$ 20$ 100$
 clearvars fval* exitflag* output*

% ------------------------------------------------
```

```
% ------------------------------------------------
```

exp5fun.m

```
% ------------------------------------------------

function f=expmin5fun(kspre,kspim,d,ei,em,wbyc)

f=[abs(  exp(2*i*(sqrt(((wbyc)^2)*ei-(kspre+i*kspim)^2)) * d) - (   ((
em*(sqrt(((wbyc)^2)*ei-(kspre+i*kspim)^2))   +   ei*(sqrt(((wbyc)^2)*em-
(kspre+i*kspim)^2))      )^2)      /      (      (em*(sqrt(((wbyc)^2)*ei-
(kspre+i*kspim)^2)) - ei*(sqrt(((wbyc)^2)*em-(kspre+i*kspim)^2)) )^2) )
)];
```

```
% ------------------------------------------------
```

expfun.m

```
% ------------------------------------------------

function f=expfun(ksp,d,ei,em,wbyc)

f=    exp(-(sqrt(abs(((wbyc)^2)*ei-ksp^2)))    *    d)    -    (        (
em*(sqrt(abs(((wbyc)^2)*ei-ksp^2)))    +    ei*(sqrt(abs(((wbyc)^2)*em-
ksp^2)))     )     /     (     em*(sqrt(abs(((wbyc)^2)*ei-ksp^2)))     -
ei*(sqrt(abs(((wbyc)^2)*em-ksp^2))) ) ) ;


% ------------------------------------------------------------------
```

Bibliography

1. ITRS Roadmap 2007 http://www.itrs.net/Links/2007Winter/2007_Winter_Presentations/09_Litho_2007_JP.pdf
2. Online information about imaging modes from http://www.veeco.com/
3. B. Hecht et al., *Journal of Chemical Physics* **112 (18),** p7761 (2000)
4. A.Chimmalgi, T.Y. Choi, C.P. Grigoropoulos and K. Komvopoulos, *Applied Physics Letters*, vol. 82, no. 8, p. 1146 (2003).
5. Christopher Loo, Amanda Lowery, Naomi Halas, Jennifer West, and Rebekah Drezek, "Immunotargeted Nanoshells for Integrated Cancer Imaging and Therapy," Nano Letters **5**, 709-711 (2005).
6. S. Nie and S.R. Emory, *Science* **275**, p1102 (1997)
7. Challener, W.A.; Mcdaniel, T.W.; Mihalcea, C.D.; Mountfield, K.R.; Pelhos, K.; Sendur, I.K. Light Delivery Techniques for Heat-Assisted Magnetic Recording. *Jpn. J. Appl. Phys.* **2003**, 42, 981-988.
8. Mcdaniel, T.W.; Challener, W.A.; Sendur, K. Issues in Heat-Assisted Perpendicular Recording. *IEEE Trans. on Magnetics* **2003**, 39, 1972-1979.
9. S. Ramo, J.R. Whinnery and T. Van Duzer, *Fields and Waves in Communication Electronics* (John Wiley and Sons, Singapore, 1994), Chapter 4.
10. R.P. Feynman, R.B. Leighton, M. Sands, The Feynman Lectures on Physics (Addison-Wesley, Boston, 1963), vol.2, chapter 23.

11. C. Kittel, *Introduction to Solid State Physics (7th edition),* John Wiley & Sons, 1996
12. J. Conway, *Efficient Optical Coupling to the Nanoscale*, PhD dissertation, University of California Los Angeles, 2006.
13. H. Bethe, *Phys.Rev***. 66**, p163 (1944)
14. C.J. Bouwkamp, *Philips Res. Rep.* **5**, p321 (1950)
15. Novotny, D. Pohl and B. Hecht, *Opt. Lett.* **20**, p970 (1995)
16. T. Tatsui et al., Applied Physics Letters 73 (15),p 2090 (1998)
17. T.W. Ebbesen et al., *Nature* **391**, p667 (1998).
18. J. Conway, *Efficient Optical Coupling to the Nanoscale*, Section 2.1, PhD dissertation, University of California Los Angeles, 2006
19. R.E. Collin, *Field Theory of Guided Waves (2nd edition)*, IEEE Press,1991
20. J. Conway, *Efficient Optical Coupling to the Nanoscale*, Section 2.3, PhD dissertation, University of California Los Angeles, 2006
21. J. Conway, *Efficient Optical Coupling to the Nanoscale*, Section 2.6, PhD dissertation, University of California Los Angeles, 2006
22. J. Conway, *Efficient Optical Coupling to the Nanoscale*, Section 3.2, PhD dissertation, University of California Los Angeles, 2006
23. J. Conway, *Efficient Optical Coupling to the Nanoscale*, Section 2.4, PhD dissertation, University of California Los Angeles, 2006
24. J. Conway, *Efficient Optical Coupling to the Nanoscale*, Section 3.5, PhD dissertation, University of California Los Angeles, 2006

25. G. Timp, et al., *IEDM Technical Digest,* pp. 615-618 (IEDM, San Francisco, 1998)

26. D. Teasdale et al., *Electrochemical and Solid State Letters* 4 (5), F11-F12 (2001)

27. Sendur, K; Challener, W. Near-field radiation of bow-tie antennas and apertures at optical frequencies. *J. Microsc*. **2003**, 210, 279-283

28. Yu, N; Cubukcu, E; Diehl, L; Bour, D; Corzine, S; Zhu, J; Höfler, G; Crozier, K.B.; Capasso, F. Bowtie plasmonic quantum cascade laser antenna. *Opt. Exp.* **2007**, 15, 13272-13281

29. Matteo, J.A.; Fromm, D.P.; Yuen, Y.; Schuck, P.J.; Moerner, W.E.; Hesselink, L. Spectral analysis of strongly enhanced visible light transmission through single C-shaped nanoapertures. *App. Phys. Lett.* **2004**, 85, 648-650.

30. L.G. Schulz and F. R. Tangherlini, Journal of the Opical Society of America, vol. 44, p. 362 (1954).

31. S. Ramo, J.R. Whinnery and T. Van Duzer, *Fields and Waves in Communication Electronics* (John Wiley and Sons, Singapore, 1994), Chapter 3.

32. Raether, *Surface Plasmons*, vol 111 of Springer-Verlag Tracts in Modern Physics (Springer-Verlag, New York, 1988).

33. E. Palik, *Handbook of Optical Constants of Solids* (Academic Press, New York, 1985)

34. Jesse Lu, FEMlab simulations on end fire coupling (unpublished)

35. Petrovic, R.; Strbac, S.; Bundaleski, N.; Rakocevic, Z. Surface roughness minimum: Ag thin layer deposited on glass. *J. Serb. Chem. Soc.* **2001**, 66, 483-490.

36. Bendavid, A.; Martin, P.J.; Wieczorek, L. Morphology and optical properties of gold thin films prepared by filtered arc deposition. *Thin Solid Films* **1999**, 354**,** 169-175.

37. Muller, D.A.; Sorsch, T.; Moccio, S.; Baumann, F.H.; Evans-Lutterodt, K.; Timp, G. The electronic structure at the atomic scale of ultrathin gate oxides. *Nature* **1999**, 399, 758-761.

38. Shi, X.; Shriver, M.; Zhang, Z.; Higman, T.; Campbell, S.A. Properties of high-k/ultrahigh purity silicon nitride stacks. *J. Vac. Sci. Technol. A* **2004**, 22, 1146-1151.

39. Stauffer, J.M.; Oppliger, Y.; Regnault, P.; Baraldi, L.; Gale, M.T. Electron beam writing of continuous resist profiles for optical applications. *J. Vac. Sci. Technol. B* **1992**, 10, 2526-2529.

40. Hu, F.; Lee, S-Y. Dose control for fabrication of grayscale structures using a single step electron-beam lithographic process. *J. Vac. Sci. Technol. B* **2003**, 21, 2672-2679.

41. Sung, J.W.; Hockel, H.; Brown, J.D.; Johnson, E.G. Development of a two-dimensional phase-grating mask for fabrication of an analog-resist profile. *App. Opt.* **2006**, 45, 33-43.

42. Sure, A.; Dillon, T.; Murakowski, J.; Lin, C.; Pustai, D.; Prather, D.W. Fabrication and characterization of three-dimensional silicon tapers. *Opt. Exp.* **2003**, 11, 3555-3561.

43. Vivien, L.; Le Roux, X.; Laval, S.; Cassan, E.; Morini, D.M. Design, Realization, and Characterization of 3-D Taper for Fiber/Micro Waveguide Coupling. *IEEE Journal of Selected Topics in Quantum Electronics* **2006**, 12, 1354-1358.

44. J. Orloff, Handbook of Charged Particle Optics (CRC Press, New York, 1997).

45. http://www.microchem.com/products/pdf/PMMA_Data_Sheet.pdf

46. S. Yasin, M.N. Khalid, D.G. Hasko, S.Sarfraz, *Microelectronic Engineering* 78-79, p484 Sp. Iss. SI (2005)

47. S. Yasin, M.N. Khalid, D.G. Hasko, *Japanese Journal of Applied Physics* vol.43 no.10, p6984 (2004)

48. K.T. Kohlmann-von Platen, W.H. Bruenger, *Journal of Vacuum Science & Technology B* 14(6), p4262 (1996)

49. K. Williams, K. Gupta, M. Wasilik, *Journal of Microelectromechanical Systems* vol.12 no.6, p761 (2003)

50. M. Hauder, J. Gstottner, L.Gao, D. Schmitt-Landsiedel, Microelectronic Engineering 64(1-4), p73 (2002)

51 Srituravanich, W.; Fang, N.; Sun, C.; Zhang, X. Plasmonic Nanolithography. *Nano. Lett.* **2004**, 4, 1085-1088.

52. Sundaramurthy, A.; Schuck, P.J.; Conley, N.R.; Fromm, D.P.; Kino, G.S.; Moerner W.E. Toward Nanometer-Scale Optical Photolithography: Utilizing the Near-Field of Bowtie Optical Nanoantennas. *Nano. Lett.* **2006**, 6, 355-360.

53. S. Backer, I. Suez, Z. Fresco, J. Frechet **,** J. Conway, **S. Vedantam**, H. Lee and E. Yablonovitch, , "Evaluation of new materials for plasmonic imaging lithography at 476nm using near field scanning optical microscopy," *Journal of Vacuum Technology B*, vol. 25, pp. 1336-1339 (2007).

54. C. Hubert et al., Nano Letters vol.5 no.4, p615 (2005)

55. Yann Gilbert, Renaud Bachelot, Alexandre Vial, Gilles Lerondel, Pascal Royer, Alexandre Bouhelier, and Gary Wiederrecht, "Photoresponsive polymers for topographic simulation of the optical near-field of a nanometer sized gold tip in a highly focused laser beam," Opt. Express **13**, 3619-3624 (2005)

56. Yann Gilbert, Renaud Bachelot, Pascal Royer, Alexandre Bouhelier, Gary P. Wiederrecht, and Lukas Novotny, "Longitudinal anisotropy of the photoinduced molecular migration in azobenzene polymer films," Opt. Lett. **31**, 613-615 (2006)

57. Yang, T.J.; Lessard, G.A.; Quake, S.R. An apertureless near-field microscope for fluorescence imaging. *Appl. Phys. Lett.* **2000**, 76, 378-380.

58. M. Brehm et al., Consolidating Apertureless NSOM. *Journal of Korean Physical Society* vol.47, ppS-80-85 (2005).

59. US Patent Pub. No. 2005/0135008, "Diffraction Grating" , William Challener, et al.

60. M. Staffaroni et al., Proposal for a Voltage Transformer at Optical Frequencies, unpublished (2009).

61. H. Choo, S. Cabrini, M. Staffaroni, P. J. Schuck. and E. Yablonovitch, "Nanofabrication and Optical Characterization of Optical Transformer with 3D-Tapered Tip," 2009 EIPBN Conference, May 26-29, 2009.

62. P. Ghenuche, S. Cherukulappurath, T. H. Taminiau, N. F. van Hulst, and R. Quidant, "Spectroscopic mode mapping of resonant plasmon nanoantennas," Phys. Rev. Lett. 101, 116805 (2008).

63. J. Tang, *Darkfield Imaging with a Plasmonic Focusing Lens: Antenna Theory for Near-field Scanning Optical Microscopes* , PhD dissertation, University of California Los Angeles, 2009.

64. P.B. Johnson & R.W. Christy, Optical Constants of the Noble Metals, Phys. Rev. B, vol.6, no. 12, pp. 4370-4379 (1972).

65. H. E. Bennett and J. M. Bennett, Optical Properties and Electronic Structure of Metals and Alloys edited by F. Abeles (North-Holland, Amsterdam, 1966), p. 175.

66. G. Brandli and A. J. Sievers, Phys. Rev. B 5, 3550 (1972).